

Electronic Thesis and Dissertation Repository

4-17-2015 12:00 AM

Novel Techniques For Investigating The Regulation Of Skeletal Muscle Hemodynamics

Baraa K. Al-Khazraji
The University of Western Ontario

Supervisor

Dr. Dwayne Jackson
The University of Western Ontario Joint Supervisor

Dr. Daniel Goldman
The University of Western Ontario

Graduate Program in Medical Biophysics

A thesis submitted in partial fulfillment of the requirements for the degree in Doctor of Philosophy

© Baraa K. Al-Khazraji 2015

Follow this and additional works at: <https://ir.lib.uwo.ca/etd>



Part of the [Biophysics Commons](#), [Circulatory and Respiratory Physiology Commons](#), [Medical Biophysics Commons](#), and the [Musculoskeletal, Neural, and Ocular Physiology Commons](#)

Recommended Citation

Al-Khazraji, Baraa K., "Novel Techniques For Investigating The Regulation Of Skeletal Muscle Hemodynamics" (2015). *Electronic Thesis and Dissertation Repository*. 2800.
<https://ir.lib.uwo.ca/etd/2800>

This Dissertation/Thesis is brought to you for free and open access by Scholarship@Western. It has been accepted for inclusion in Electronic Thesis and Dissertation Repository by an authorized administrator of Scholarship@Western. For more information, please contact wlsadmin@uwo.ca.

NOVEL TECHNIQUES FOR INVESTIGATING THE REGULATION OF
SKELETAL MUSCLE HEMODYNAMICS

(Thesis format: Integrated Article)

by

Baraa Karim Al-Khazraji

Graduate Program in The Department of Medical Biophysics

A thesis submitted in partial fulfillment
of the requirements for the degree of
Doctor of Philosophy

The School of Graduate and Postdoctoral Studies
The University of Western Ontario
London, Ontario, Canada

© Baraa Karim Al-Khazraji 2015

Abstract

The effect of the sympathetic nervous system (SNS) on blood flow distribution within skeletal muscle microvasculature is conditional upon regional activation of SNS receptors. Due to a lack of appropriate experimental models and techniques, no study has systematically evaluated the effect of SNS receptor activation in continuously branching skeletal muscle arteriolar trees. In line with previous work, we hypothesize that there will be a spatially-dependent distribution of sympathetic receptor activation along the arteriolar tree. Specifically, we anticipate a progressive decrease of adrenergic activation and a progressive increase of peptidergic and purinergic activation with increasing arteriolar order. We developed a novel rat gluteus maximus (GM) muscle preparation which provided access to a large vascular network, from which we developed an experimental method for collecting cell velocity profiles in fast-flowing arterioles. Using these data, we derived an empirical relationship between velocity ratio (V_{Max}/V_{Mean}) and arteriolar diameter, collected novel data on cell free layer width and estimated wall shear rates, and derived a wall shear rate equation from experimental data that can be used for calculating wall shear rates in skeletal muscle microvasculature. We evaluated SNS receptor activation ($\alpha 1R$, $\alpha 2R$, NPY1R, and P2X1R) in continuously branching arteriolar trees in the rat GM, as a function of network topology. A computational flow model estimated the total flow, resistance, and red blood cell flow heterogeneity. For the first time, we highlight effects of SNS receptor activation on network hemodynamics, where proximal arterioles responded most to adrenergic activation, while distal arterioles responded most to Y1R and P2X1R activation. Our data highlight the functional consequences of topologically-dependent SNS receptor activation. The tools developed in this thesis are beneficial for computing hemodynamic parameters from *in vivo* data, as well as providing input variables to and validation of computational flow models.

Keywords

Sympathetic nervous system, skeletal muscle, arterioles, blood flow, hemodynamics, microcirculation, norepinephrine, neuropeptide Y, ATP, computational modelling, fluorescent red cells, velocity profiles, wall shear rate.

List of Abbreviations and Symbols

$\bar{V}_{RBC\ Edge}$: mean of edge velocities of the velocity profile

A_{Vessel} : vessel cross-sectional area

V_{Center} : centerline velocity

$V_{Edge\ Factor}$: conversion factor for calculating experimental edge velocities

V_{Edge} : velocity value at the edge of the velocity profile

$V_{Expt\ RBC\ Edge}$: experimentally-acquired velocity value at the edge of the velocity profile

V_{Max} : maximum velocity

V_{Mean} : mean velocity

V_{RBC} : red blood cell velocity

V_{Ratio} : velocity ratio, index of velocity profile bluntness

$Width_{CFL}$: red blood cell free layer width

$\frac{dP}{dx}$: partial pressure gradient along a vessel segment

ΔP : change in pressure in a vessel segment

μ : blood viscosity in a vessel segment

μ_{pl} : plasma viscosity in a vessel segment

μ_{rel} : relative blood viscosity in a vessel segment

ANOVA: analysis of variance

ATP: adenosine triphosphate

cAMP: cyclic adenosine monophosphate

CCD: charged-couple device

COX: cyclooxygenase

D: arteriolar diameter

EDHF: endothelial derived hyperpolarizing factor

EDL: extensor digitorum longus

E_{Max} : absolute maximum constriction response

FITC: fluorescein isothiocyanate

GM: gluteus maximus muscle

GPC: G-protein coupled receptor

Hct: hematocrit

H_D : discharge hematocrit

Hz: hertz

IVVM: intravital video microscopy

L: vessel length

$LogEC_{50}$: concentration of agonist which elicits half of the maximum constriction response

NA: numerical aperture

NE: norepinephrine

NO: nitric oxide

NPY: neuropeptide Y

P2X1R: purinergic receptor subunit type 1 receptor

PE: phenylephrine

PRU: peripheral resistance units

PSS: physiological salt solution

r: vessel radius

r^2 : coefficient of determination

RBC: red blood cell

R_C : radius of the red blood column

R_S : radius of vessel at the centroid of the edge streak

R_{Wall} , R_L : radius of vessel lumen

S.E.M.: standard error of the mean

SD: standard deviation

sec: second (unit of time)

SNP: sodium nitroprusside

SNS: sympathetic nervous system

TH: tyrosine hydroxylase

TPR: total peripheral resistance

Y1R: neuropeptide Y Y1 receptor

α 1R: α 1 adrenergic receptor

α 2R: α 2 adrenergic receptor

D : oxygen diffusion constant

Q, \dot{Q} : blood flow

R : resistance in a vessel segment

k : oxygen's solubility in a given medium

Co-Authorship Statement

The work (conception, design, experimentation, data analyses, and preparation of manuscript) contained in this dissertation was performed by the author (BKA), under the supervision of Dr. Dwayne N. Jackson and Dr. Daniel Goldman, with the advice of Dr. Christopher G. Ellis.

In Chapter 2, Dr. Nicole M. Novielli assisted with surgical training, and Dr. Philip J. Medeiros collected flow cytometry data. In Appendix C, Dr. Philip J. Medeiros conducted cell migration assays and assisted with writing the methods section of the manuscript, and Dr. Nicole M. Novielli provided manual measurements to serve as a gold standard in analysis.

Dedication

It is with great honor that I dedicate this thesis, my greatest academic achievement thus far, to my family, my husband, and my 9 month old daughter Emilene.

To my father with the captivating smile, Karim Al-Khazraji, although you left this world too early, you have provided eternal enrichment to my life from my childhood memories alone. I not only dedicate this thesis to you, but I dedicate all of my academic work to you. We will continue to publish together, side by side, as Baraa *Karim Al-Khazraji*.

To my sweet, and most generous mother, Hanan, you independently raised 4 children while holding down a job to provide for us. You never let me see myself as anything short from spectacular. It is when I think of you, and how you see me, that I keep myself in check and always seem to do what is best.

To my siblings, Hajar, Sayf and Adam, if I can do this, you three can do anything. Always remember that no one has the connection that we have. Our roots are intertwined, no matter how far apart we are from each other. I see you as my older sister and brothers. I am in awe watching you grow to become your own individual selves. You continually inspire me.

To the man I am blessed to call my husband, Asoomy, we have squeezed in an enormous amount of “living” in the time that we have known each other. Thank you for *always* being here, right here beside me, right where I wanted you. You are the ideal teammate for me, and were integral to this entire process. You provided me with the mental clarity that was required for me to see this to its end. Thank you as a wife, and as a mother.

To the most precious creature I have ever come to know, my baby Emilene. Mama is so proud and excited that she can even be in a position to write about you in her dissertation! You were a complete gem throughout the entire process, and I have learned a lot about myself from you. Throughout this entire rollercoaster of a PhD, everything turned out better than you or I could have imagined. You make Mama and Baba’s life feel very full and rich.

Acknowledgements

Throughout the course of my PhD, I learned more about myself, the scientist and person, than I did about sympathetic receptors and hemodynamics. I have several people to thank and acknowledge for taking part in this journey with me.

My supervisors Dr. Dwayne Jackson and Dr. Daniel Goldman, I owe you many thanks for your patience, guidance, and continuous support. Thank you for always providing me with opportunities to grow as a young scientist, and as an individual thinker. Thank you for guiding me in such a way where I was able to harness my strengths, and work on my weaknesses. To Dr. Christopher G. Ellis, you have been more than a member of my PhD advisory committee. Your words of advice transcend the confines of my PhD. I am forever grateful to you for imparting your wisdom to me.

Thank you to my thesis examiners (Drs. Steve Segal, Peter Canham, Ian MacDonald, and Jamie Melling) for extensively going through my thesis, providing many beneficial comments and making several edits. You made the defense a very enjoyable experience (surprisingly!). Thank you Dr. Roland Pittman (VCU) for all of your effort and involvement in promoting the success of my career.

My labmates that turned into the dearest of friends, Nicole, Phil, and Nate, thank you for being genuine, for always caring, for belly aching laughs and most importantly, thank you for letting us pick up where we left off.

The many good people (students, professors – special thanks to Dr. Peter Canham, Dr. Jerry Battista, Dr. Grace Parraga – and administration – special thanks to Wendy Hough for looking out for me for nearly a decade!) of MBP that I run into at seminars or in the hallway, and have more of a positive impact on me than they know. You have provided the perfect atmosphere for learning by making the department feel more like a community. I have likely thanked you in person far too many times, so you very well know who you are!

My decade (and then some) life-long friends, my Windsor girls, my undergraduate Perth girls, and my graduate-school-turned-into-long-term friends. What haven't we seen each other go through? Thanks for the soul food.

My family who were my foundation, and my focus of a horizon when I felt as though I lost sight of things. Mama, Hajar, Sayf, and Adam, your words of encouragement kept me going. Thank you Baba, your spirit accompanied me the entire way, and you helped me persevere.

Most of all thank you to my teammate of a husband, you pulled more than your weight, especially near the end, so I could finish my degree. My daughter, Emilene, you gave new meaning to this PhD. Thank you both for using your smiles to remind me that at the end of the day, I have a home in your hearts.

Table of Contents

Abstract.....	ii
List of Abbreviations and Symbols.....	iv
Co-Authorship Statement.....	vii
Dedication.....	viii
Acknowledgements.....	ix
Table of Contents.....	x
List of Tables.....	xv
List of Figures.....	xvi
List of Appendices.....	xviii
Chapter 1 : General introduction.....	1
1.1 What is the microcirculation?.....	2
1.2 What is unique to skeletal muscle microcirculation?.....	4
1.3 How is skeletal muscle microcirculation regulated?.....	5
1.4 Sympathetic nervous system-mediated arteriolar vasoconstriction.....	7
1.5 Importance of the SNS in microvascular control.....	9
1.6 The overlooked non-adrenergic control of skeletal muscle microcirculation.....	10
1.7 Importance of network topology in microvascular regulation.....	16
1.8 Where has skeletal muscle microvasculature classically been studied?.....	18
1.9 How has skeletal muscle microcirculation classically been imaged?.....	24
1.10 Purpose of thesis dissertation.....	30
1.11 References.....	31
Chapter 2 : A simple “streak length method” for quantifying and characterizing red blood cell velocity profiles and blood flow in rat skeletal muscle arterioles.....	39
2.1 Introduction.....	40
2.2 Materials and methods.....	42

2.2.1	Preparations and protocols	42
2.2.2	Intravital video microscopy	44
2.2.3	RBC streaks, velocity profiles and flow calculations	45
2.2.4	Statistical analyses and data presentation	51
2.3	Results.....	53
2.3.1	Systemic measures and arteriolar responses to O ₂	53
2.3.2	Streak length method validation	53
2.3.3	<i>In vivo</i> velocity profiles, experimental blood flow calculations, and velocity ratios.....	53
2.4	Discussion.....	56
2.4.1	Measuring V _{RBC} in skeletal muscle arterioles.....	56
2.4.2	Arteriolar RBC velocity profiles.....	58
2.4.3	Relationship between blood flow and arteriolar diameter	59
2.5	Conclusion	60
2.6	References.....	61
Chapter 3 : Taking the “stress” out of shear rate calculations: An experimentally-derived shear rate equation for use in skeletal muscle microvasculature		
3.1	Introduction.....	65
3.2	Materials and methods	67
3.2.1	Data source.....	67
3.2.2	Data analysis: Wall shear rate estimation	67
3.2.3	Data analysis: Development of an experimentally derived and straightforward wall shear rate equation.....	68
3.2.4	Data analysis: Comparison to other wall shear rate calculation methods.	70
3.2.5	Statistical analysis.....	71
3.3	Results.....	71
3.3.1	Wall shear rate estimation from <i>in vivo</i> velocity profiles.....	71

3.3.2	Development of an experimentally-derived and straightforward wall shear rate equation.....	78
3.3.3	Comparison of wall shear rate calculation methodologies	83
3.4	Discussion.....	85
3.4.1	Wall shear rate estimation.....	85
3.4.2	Development of an experimentally derived and straightforward wall shear rate equation.....	86
3.4.3	Comparison of wall shear rate calculation methodologies	88
3.5	Conclusion	89
3.6	References.....	90
Chapter 4 : From one generation to the next: A comprehensive account of sympathetic receptor control in branching arteriolar trees		
4.1	Introduction.....	94
4.2	Materials and methods	96
4.2.1	Animal care and use.....	96
4.2.2	Anesthesia and skeletal muscle preparation	96
4.2.3	Intravital video microscopy (IVVM)	97
4.2.4	Experimental protocols	98
4.2.5	Selection of agonist concentrations	99
4.2.6	Experimental data collection.....	100
4.2.7	Tissue viability and inclusion criteria	101
4.2.8	Arteriolar order classification	101
4.2.9	Computational modelling.....	102
4.2.10	Data presentation and statistical analyses	105
4.3	Results.....	108
4.3.1	Phenylephrine data.....	108
4.3.2	UK 14,304 data	110

4.3.3	Neuropeptide Y data	110
4.3.4	ATP data	113
4.3.5	α,β -methylene ATP data	113
4.3.6	Computational analysis: Calculating hemodynamic consequences from spatially-dependent SNS receptor activation	117
4.4	Discussion	125
4.4.1	Experimental findings: Topologically-dependent sympathetic control along arteriolar trees	125
4.4.2	Computational findings: Total network resistance and flow changes as a result of a differential distribution of receptors for sympathetic neurotransmitters.....	133
4.5	Conclusion	135
4.6	References	136
Chapter 5 : General discussion		142
5.1	Development of the gluteus maximus skeletal muscle preparation.....	143
5.2	Development of a method for calculating blood flow in fast-flowing arterioles	144
5.3	Use of <i>in vivo</i> red blood cell velocity profiles for estimating wall shear stress..	148
5.4	Recent use of “streak length” method in skeletal muscle microvascular studies	151
5.5	Use of “streak length” method for the validation of an in-house computational flow model	153
5.6	Use of the rat GM for investigating SNS receptor functionality in branching arteriolar trees	155
5.7	Topologically-dependent SNS receptor activation and ligand contribution.....	157
5.8	Importance of collecting data from microvascular networks	158
5.9	Future Studies	159
5.9.1	Experimental values of hematocrit	159
5.9.2	Sympathetic nervous system co-transmission of neurotransmitters	161
5.9.3	Other topics of interest.....	162
5.10	References.....	163

Appendices.....	166
Appendix A: Copyright license agreement for Chapter 2	166
Appendix B: Animal use protocol approval	167
Appendix C: An automated cell-counting algorithm for fluorescently-stained cells in migration assays	168
Appendix D: Cell counting algorithm.....	182
Curriculum Vitae	184

List of Tables

Table 4.1: Summary values for 5 arteriolar orders.	107
---	-----

List of Figures

Figure 1.1: Topologically-dependent SNS receptor functionality.....	15
Figure 2.1: Schematic of streak length method technique.....	46
Figure 2.2: Velocity profiles from binned diameters of arteriolar segments.....	47
Figure 2.3: Relationship between experimental blood flow and arteriolar diameter.....	52
Figure 2.4: Relationship between velocity ratio and arteriolar diameter.....	55
Figure 3.1: Relationship between experimentally acquired wall shear rate and arteriolar diameter.....	73
Figure 3.2: Relationship between cell free layer width and arteriolar diameter.....	74
Figure 3.3: Normalized cell free layer as a function of arteriolar diameter.....	75
Figure 3.4: Relationship between profile edge velocity and arteriolar diameter.....	76
Figure 3.5: Relationship between centerline velocity and arteriolar diameter.....	77
Figure 3.6: Relationship between change in cell free layer width and centerline velocity. ...	79
Figure 3.7: Comparison of experimental and calculated wall shear rates.....	82
Figure 3.8: Comparison of wall shear rates (WSR) using different velocity ratios.....	84
Figure 4.1: Arteriolar responses to $\alpha 1R$ activation at 5 arteriolar orders.....	109
Figure 4.2: Arteriolar responses to $\alpha 2R$ activation at 5 arteriolar orders.....	111
Figure 4.3: Arteriolar responses to Y1R activation at 5 arteriolar orders.....	112
Figure 4.4: Arteriolar responses to ATP application at 5 arteriolar orders.....	114
Figure 4.5: Arteriolar responses to ATP application with P2X1R blockade at 5 arteriolar orders.....	115

Figure 4.6: Arteriolar responses to $\alpha\beta$ -meATP application at 5 arteriolar orders.	116
Figure 4.7: Computational network reconstruction schematic.	118
Figure 4.8: Validation of computational flow data with experimental flow data.	119
Figure 4.9: Calculated total network flow during baseline, and sympathetic receptor activation.....	121
Figure 4.10: Calculated total network resistance during baseline, and sympathetic receptor activation.....	122
Figure 4.11: Change in RBC flow heterogeneity at 2A to 5A during sympathetic receptor activation.....	124

List of Appendices

Appendix A: Copyright license agreement for Chapter 2	166
Appendix B: Animal use protocol approval	167
Appendix C: An automated cell-counting algorithm for fluorescently-stained cells in migration assays.....	168
Appendix D: Cell counting algorithm.....	182

Chapter 1: General introduction

The chapter was solely written by BKA. Excerpts of this chapter have been modified to assist in the preparation of the following manuscript:

Shoemaker JK, Badrov M, Al-Khazraji BK, Jackson DN. (2015). Neural control of vascular function (invited review). *Compr Physiol.* (in 2nd review, May 2015)

Manuscript ID: CPHY-15-0004

1.1 What is the microcirculation?

The microcirculation is comprised of the smallest vessels in the body, namely the arterioles, capillary networks and the venules. The microcirculation is embedded within a tissue or organ, allowing there to be an intimate interaction between these vessels and the surrounding parenchyma. This anatomical set-up provides immediate exchange of gasses, metabolites and nutrients both to and from the microcirculation and the proximate tissue. One of the unique features of the microcirculation is that it does not scale with species, in that capillary and red blood cell sizes are similar from mouse to large mammals (West *et al.*, 1997). This feature allows for cross-examination of hemodynamic responses between species, where conclusions drawn from microcirculatory studies likely carry relevance across a wide range of animal species.

Progressing from the larger conduit vessels (e.g., aorta and arteries) into the microcirculation, there is a large decrease in vascular inner diameter. Feed arterioles entering a tissue can be up to 200 μm in diameter, followed by an intermediate branching arteriolar network that leads to an interconnected parallel network of capillaries with 4-8 μm inner luminal diameter, and exiting venules. At the arteriolar level, this decrease in diameter is met with a large increase in vascular resistance as well as the greatest pressure drop in the circulatory system (Fronek & Zweifach, 1975). Poiseuille's flow equation (Equation 1.1) coupled with a variation on Ohm's law (Equation 1.2), describes the relationship between pressure, resistance, flow, and geometry in microvascular beds. Poiseuille's equation (Equation 1.1) is useful when modelling a vessel segment as a straight smooth bore tube with a constant radius, which contains steady laminar flow with Newtonian (i.e., constant) viscosity.

Equation 1.1

$$\Delta P = \frac{8\mu LQ}{\pi r^4}$$

Equation 1.2

$$\Delta P = QR$$

Where ΔP is change in pressure along a vessel segment (Equation 1.1) or across any two points in the circulatory system (Equation 1.2), μ is blood viscosity, L is length of vessel segment, Q is blood volume flow through a vessel segment (Equation 1.1) or across any two points in the circulatory system, r is the radius of a vessel segment. Equation 1.1 and 1.2 can be combined to solve for R , or resistance, for a given vessel,

Equation 1.3

$$R = \frac{8\mu L}{\pi r^4}$$

It is through modification of these hemodynamic parameters that resistance (R) in the microcirculation is controlled, and blood flow is regulated in a tissue. Therefore, in addition to metabolite exchange within the tissue and regulation of systemic arterial pressure via changes in total peripheral resistance, the microcirculation serves to regulate blood flow distribution both to and within tissues.

Blood is a suspension of formed elements in plasma (primarily made up of water, and contains dissolved proteins, electrolytes, sugars, clotting factors) and consists of a red blood cell (RBCs; 42-45%), white blood cells (1/600 of total cell volume), and platelets (1/800 of total cell volume). Blood flowing through a vessel segment generally follows a

two-phase model, where RBCs aggregate towards the center resulting in axial accumulation, and a plasma annulus is left near the inner wall of the vessel (Popel & Johnson, 2005). Poiseuille's equation (Equation 1.1) leads to a parabolic velocity profile, but blunted velocity profiles can be explained by radial variations in viscosity produced by variations in RBC density when blood flow is modelled as a two-phase model.

1.2 What is unique to skeletal muscle microcirculation?

Skeletal muscle comprises a large proportion of the body's weight [$\sim 40\%$ of total body mass (Janssen *et al.*, 2000)]. This large active tissue is fed with highly regulated vascular networks which allows skeletal muscle to increase its blood flow supply by up to 100-fold (Andersen & Saltin, 1985). The largest volume of resistance arterioles resides within skeletal muscle, and is also where the greatest contribution to total peripheral resistance occurs.

Each muscle fiber exhibits its own resting metabolic demand, which is primarily governed by its fiber type (Mackie & Terjung, 1983). This unique level of demand is precisely met by adequate blood flow, which is finely titrated by concurrent neurally-mediated vasoconstriction (supplied by the SNS) and metabolically mediated vasodilation. Thus, this myofiber-centric blood flow supply results in heterogeneous levels of blood flow distribution across a single muscle tissue (Koga *et al.*, 2014). As well, blood flow heterogeneity across striated muscle tissue may result from time-dependent variability in blood flow distribution, thereby illustrating that skeletal muscle is subject to both spatially- and temporally-dependent changes in blood flow heterogeneity (Iversen & Nicolaysen, 1989).

To summarize, the uniqueness of skeletal muscle microvasculature is a result of the following: 1) the majority of total peripheral resistance is controlled and maintained within skeletal muscle microvasculature, 2) the ability of skeletal muscle to increase its blood supply by up to 100-fold, 3) heterogeneous blood flow distribution within a single muscle, and 4) its microvasculature is fine-tuned to precisely match the metabolic demands of muscle fibers on a moment-by-moment basis. Furthermore, skeletal muscle is responsible for adjustments to posture and voluntary movement, both of which require instantaneous coordinated changes in blood flow supply.

To this end, investigating microvascular hemodynamics in skeletal muscle models provides the opportunity to characterize the behaviour of the microcirculation over a wide range of metabolic conditions (e.g., resting heterogeneous blood flow distribution to near instantaneous 100-fold increases in blood flow supply during muscular contraction).

Experiments utilizing skeletal muscle preparations for the study of blood flow provide insight to the vast capacity of control elicited by the microcirculation's innate regulatory mechanisms, and how these mechanisms may adapt or become disrupted during abnormal tissue conditions.

1.3 How is skeletal muscle microcirculation regulated?

The essence of microvascular regulation lies in maintaining the balance between oxygen supply in the microvessels, and the oxygen demand of the surrounding tissue. Regulation of skeletal muscle microvasculature involves fulfilling regional metabolic demands of single muscle fibers, as well as integrating local blood flow responses to ensure overall adequate blood supply to the whole tissue. Fick's law of diffusion, given by Equation 1.4, best describes the assimilated responses to oxygen extraction in microvascular networks.

Equation 1.4

$$F = -DkA \left(\frac{dP}{dx} \right)$$

In the context of oxygen transfer, Fick's law states that oxygen flux (F) occurs down a partial pressure gradient $\left(\frac{dP}{dx}\right)$, is proportional to the surface area of the membrane (A), and is inversely proportional to the thickness of the membrane through which oxygen must travel (x). D refers to oxygen diffusion constant, and k is oxygen's solubility in a given medium. To facilitate the exchange of oxygen in the microcirculation, oxygen transfer occurs in the arterioles as well as in the capillaries where the thinnest vascular walls reside (i.e., one endothelial cell thick), and the flow is significantly slower in order to provide enough time for oxygen extraction. As well, the greatest surface area throughout the vascular network occurs at the capillaries (Poole *et al.*, 2013), further optimizing oxygen extraction from RBCs.

As described, the topological features of the capillary bed facilitate oxygen extraction into the surrounding parenchyma. Capillaries are not directly regulated by the SNS, and must rely on the received blood volume flow in order to determine the hematocrit (or percentage of RBCs in whole blood) and RBC supply rate, and the ensuing oxygen available for extraction. The arterioles directly feed into the capillary network, which then immediately feed into the venular network. Microvascular regulation, and therefore coordinated blood flow delivery to and from the capillaries, occurs in both the arteriolar and the venular components of the microvascular system.

Skeletal muscle microvascular regulation is governed by a net effect of multiple vasostimulatory actions (Segal, 2005) including vasoconstriction, vasodilation, and the consequent “network” effect on responses as illustrated by the effects of upstream and/or downstream resistance. For a given site, local microvascular regulation is executed either through constriction or dilation at a given vessel. The degree to which constriction or dilation occurs depends on the integration of supply-demand relationships across an entire network. That is, resistance vessels may instantaneously dilate (allow for more blood flow when metabolic demands are high) (Naik *et al.*, 1999) or constrict (conserve blood flow when demands are low) in order to meet metabolic demands of the tissue on a moment-by-moment basis; however, in order to maintain perfusion throughout the whole tissue, constriction/dilation occurs within the confines of assimilating vasoregulation across multiple branch orders of a network. Thus, the underpinnings of microvascular regulation must reside in a network’s topology, where any investigation of regulation at this level ought to consider both the geometry (i.e., diameter) and the topology (i.e., length, branch order) of the network.

1.4 Sympathetic nervous system-mediated arteriolar vasoconstriction

The sympathetic nervous system (SNS) is the autonomic regulator of microvascular flow in skeletal muscle. Numerous locally derived/released endothelial factors evoke ongoing vasodilation [notably nitric oxide (NO), ATP (adenosine triphosphate), cyclooxygenase (COX), endothelial derived hyperpolarizing factor (EDHF), adenosine from 5’-nucleotidase (5’NUC)]. For the purposes of this thesis, only the SNS and its contributions to vascular resistance will be discussed.

The sympathetic nervous system innervates the adventitiomedial layer of arterioles, coming in direct contact with vascular smooth muscle cells. These nerves elicit tonic vasoconstriction of arterioles through the release of norepinephrine (NE), neuropeptide Y (NPY), and ATP acting on their associated receptors (α 1R and α 2R, Y1R, and P2X1R) located on smooth muscle cells. Independent of the SNS, vasomotor tone is set by the integration of myogenic contraction of smooth muscle and the vasodilator influence of the endothelium.

There are four vascular smooth muscle cell sympathetic receptors that are responsible for arteriolar vasoconstriction: α 1 adrenergic receptor, α 2 adrenergic receptor, NPY Y1 receptor, and P2X1 receptor. The two adrenergic receptors (O'Connell *et al.*, 2014) and the NPY Y1R receptor (Hirsch & Zukowska, 2012) are classified under the metabotropic G-protein coupled receptor (GPCR) family of receptors; whereas the purinergic receptor subunit type 1 receptor (P2X1R) is part of the ligand-gated ion channel family of receptors (specifically, an ATP-gated cation channel) (Surprenant & North, 2009).

The α 1 adrenergic receptor (α 1R) belongs to the Gq/11 family of heterotrimeric G proteins. Briefly, upon α 1R activation via norepinephrine or epinephrine binding, β -isoforms of phospholipase C are stimulated and generate IP_3 which then causes a release of calcium (Ca^{2+}) from intracellular stores and activation of protein kinase C (PKC; to phosphorylate and activate downstream cascade of protein signaling) via DAG (Exton, 1996). This release of Ca^{2+} binds onto calmodulin, which activates myosin light chain kinase to phosphorylate myosin heads, increasing myosin ATPase activity. Myosin cross-bridges are created causing actin to slide over using myosin power strokes (sliding filament theory) to contract the smooth muscle, resulting in overall vasoconstriction.

Both the NPY Y1R (Brothers & Wahlestedt, 2010) and the α_2 adrenergic receptor (α_2R) (Bylund, 1992) belong to the Gi family of the heterotrimeric G proteins. Upon ligand binding, this receptor acts through adenylyl cyclase inhibition, ultimately attenuating cyclic adenosine monophosphate (cAMP) production from ATP. The drop in cAMP increases the activity of myosin light chain kinase, thereby phosphorylating myosin light chain and resulting in overall vasoconstriction.

In contrast to the above metabotropic receptors, the P2X1 receptor is an ionotropic receptor and a member of the ligand-gated ion channel P2X receptor family (Valera *et al.*, 1994). Upon binding of ATP to an allosteric binding site, the P2X1 receptor changes conformation and allows for Ca^{2+} and Na^{2+} into the cell, depolarizing smooth muscle cells and resulting in overall vasoconstriction in the arteriole.

1.5 Importance of the SNS in microvascular control

Activation of the SNS receptors in the periphery largely contributes to the maintenance of total peripheral resistance (TPR) in the control of systemic blood pressure. To illustrate, the mere act of a person moving from a supine to a standing position, requires activation of the SNS in order to maintain mean arterial pressure when cardiac output falls in order to prevent neurally-mediated syncope (Fu & Levine, 2014). As well, SNS-mediated maintenance of blood pressure, via control of TPR, is achieved in the face of cardiac output distribution to various tissues and organs, as well as blood flow redistribution within tissues, based on local regional metabolic needs.

The SNS and its actions are graded with the level of exercise; in the case of high intensity exercise, cardiac output is redirected from the splanchnic circulation to the active limbs

(Rowell *et al.*, 1964). These regulatory mechanisms speak to the various degrees of control (peripherally) the SNS exerts on the cardiovascular system: from maintenance of blood pressure to fine-tuned distribution of blood flow fractions within microvascular networks, which will be further discussed in sections below.

1.6 The overlooked non-adrenergic control of skeletal muscle microcirculation

The majority of studies characterizing sympathetic neuronal density expression in skeletal muscle microvasculature have utilized data collected from adrenergic neuronal staining. One of the earliest reports of adrenergic nerve fiber density in a skeletal muscle vascular bed was from the cat gastrocnemius and tibialis anterior muscles, where adrenergic fibers uniformly innervated the microcirculation (Fuxe & Sedvall, 1965). Similarly, immunohistochemical analysis performed in the rat cremaster (Fleming *et al.*, 1989) and later in the hindlimb of the guinea pig (Anderson *et al.*, 1996) and in the hamster retractor muscle (Grasby *et al.*, 1999) resolved spatially-dependent co-localized tyrosine hydroxylase (TH; rate-limiting enzyme in the synthesis of norepinephrine) and NPY-containing axons, where these neurons uniformly innervated proximal to distal arterioles, but not veins or venules. As well, in the case of the hamster retractor and cheek pouch study, these NPY and TH co-localized adrenergic neurons were only present on the skeletal muscle region (retractor) and were absent on the epithelial (cheek pouch) portion of the preparation (Grasby *et al.*, 1999).

There are a limited number of studies investigating sympathetic neuronal density as a function of arteriolar network topology. The adrenergic plexus spatial density (via catecholaminergic neuronal staining with glyoxylic acid) has been shown to be

topologically-dependent within the arteriolar network, where there is a progressive increase in adrenergic nerve density when transitioning from the arcade to transverse arterioles in the rat spinotrapezius, and is absent in terminal arterioles (Saltzman *et al.*, 1992). As well, NPY-containing sympathetic axons profusely innervate resistance vessels (i.e., arterioles) and become progressively more dense with increasing arteriolar order (Sundler *et al.*, 1993). Evidence for a differential neuronal density distribution at the microanatomical level provides indication of topologically-dependent heterogeneous sympathetic control in skeletal muscle microvasculature.

One of the first detailed accounts of heterogeneous arteriolar responses to sympathetic stimulation in skeletal muscle was provided by Marshall's work on the microvascular bed of the rat spinotrapezius (Marshall, 1982). In congruence with aforementioned findings on spatially-dependent sympathetic innervation in skeletal muscle microvasculature, Marshall reported order-dependent differences in arteriolar responses, where 1st and 2nd order arterioles exhibited a gradual on-set in large vasoconstrictor responses to paravascular nerve stimulation at 8-10 Hz (up to an 85% decrease in diameter), which was in contrast to the rapid on-set of short-lived constriction responses exhibited by terminal arterioles.

Similarly, during sympathetic nerve stimulation, maximum constriction occurred in 4th order vessels, and there was a progressively greater "sympathetic escape" (i.e., secondary fall in vascular resistance) with increasing arteriolar orders of the cat sartorius (Boegehold & Johnson, 1988). Furthermore, in 1st to 6th order arterioles of the exteriorized cat sartorius muscle, 3rd order arterioles have the greatest levels of responses during concurrent sympathetic nerve stimulation at 8 Hz (Dodd & Johnson, 1991).

In complementary experiments, sympathetic neuronal stimulation in the rat cremaster elicited vasoconstriction along the arteriolar network; yet, responses were abolished in proximal vessels with the concurrent addition of prazosin (α 1R antagonist), and were also abolished in distal vessels with the addition of rauwolscine (α 2R antagonist). This study also suggested that sympathetic nerve stimulation at low frequencies (corresponding to basal neurogenic vascular tone) of 0.2-2 Hz results in preferential constriction of small arterioles via α 2-adrenergic receptor activation, and would largely contribute to changes in neurogenic resistance. At higher neuronal firing frequencies in the rat cremaster, proximal arterioles would be more responsive via α 1 adrenergic receptor activation and would be the predominant determinant of neurogenic tone (Ohyanagi *et al.*, 1991). These varying constrictor patterns could reflect variations in sympathetic neurotransmitter release patterns, post-junctional receptor sensitivity and/or post-receptor contractile properties of vascular smooth muscle.

In the rat hindlimb, sympathetic stimulation elicited blood flow responses during muscle contraction that were dependent on contraction intensity and muscle fiber type (i.e., high oxidative rat soleus did not exhibit functional sympatholysis (inhibition of SNS mediated vasoconstriction during skeletal muscle contraction) during maximal contractions, compared to absence of functional sympatholysis in the highly-glycolytic rat gastrocnemius-plantaris muscles during low-intensity contractions) (Thomas *et al.*, 1994). Despite these differences, application of specific adrenergic agonists elicited similar arteriolar vasoconstrictor responses between both the mouse fast-twitch extensor digitorum longus muscle and the slow-twitch soleus muscle, highlighting that vascular

responses to adrenergic receptor activation are independent from skeletal muscle type (Lambert & Thomas, 2005).

Interestingly, despite the existence of three different SNS neurotransmitters acting on their respective receptors, both the roles of NPY and ATP in skeletal muscle blood flow regulation remain to be characterized. The view, more recently considered as oversimplified, that sympathetic vascular control is dominated by the adrenergic system was primarily justified by a) baseline NE concentration and an increase in NE concentration during stress (Zukowska-Grojec *et al.*, 1988); and b) decrease in vascular resistance, and blood pressure, during prazosin administration (α 1R adrenergic blockade) (Oates *et al.*, 1976).

However, despite having negligible effects on blood pressure, NPY itself elicits vasoconstriction at interstitial concentrations that are nearly 1000 \times lower than NE (Hirsch & Zukowska, 2012; Mortensen *et al.*, 2012). In fact, NPY was shown to play an important role in microvascular flow regulation through its effects on Y1R in distal arterioles (Jackson *et al.*, 2004). As previously mentioned, the density of NPY-containing axons progressively increases with decreasing resistance vessel diameter (Sundler *et al.*, 1993). Therefore, despite higher interstitial concentrations of NE, the above highlights that NE and NPY possess spatially-dependent heterogeneous functions in the vasculature (i.e., proximal versus distal locations of action). This is further supported by work on cat microcirculatory beds showing that both NPY (Ekelund & Erlinge, 1997) and ATP studies in the rat (Gitterman & Evans, 2000) exert diameter-dependent vasoconstrictor responses, with peak responses occurring at the distal arterioles. Taken together, the classically accepted adrenergic view of vascular control may have evolved from a

shortage in comprehensive evaluations of SNS-mediated vasoconstrictor effects at multiple microvascular branch orders.

To further investigate the spatially- or topologically-dependent heterogeneous response to receptor activation, α -adrenoreceptor (i.e., α 1R and α 2R) arteriolar control of the rat cremaster (Faber, 1988; Ohyanagi *et al.*, 1991) and mouse gluteus maximus muscle (Moore *et al.*, 2010) were investigated. However, these studies were limited to adrenoreceptor control in partial networks (i.e., 1st to 3rd order arterioles), and primarily focused on acquiring functional bio-assay data on ligand sensitivity, leaving any consequent hemodynamic changes to speculation. Thus, our working hypothesis is that there may be an emerging relationship between network topology and ligand-receptor activation, suggesting there may be a heterogeneous vaso-active response to all 4 sympathetic receptors progressing from the proximal (feed artery) to the distal (pre-capillary terminal arterioles) arterioles.

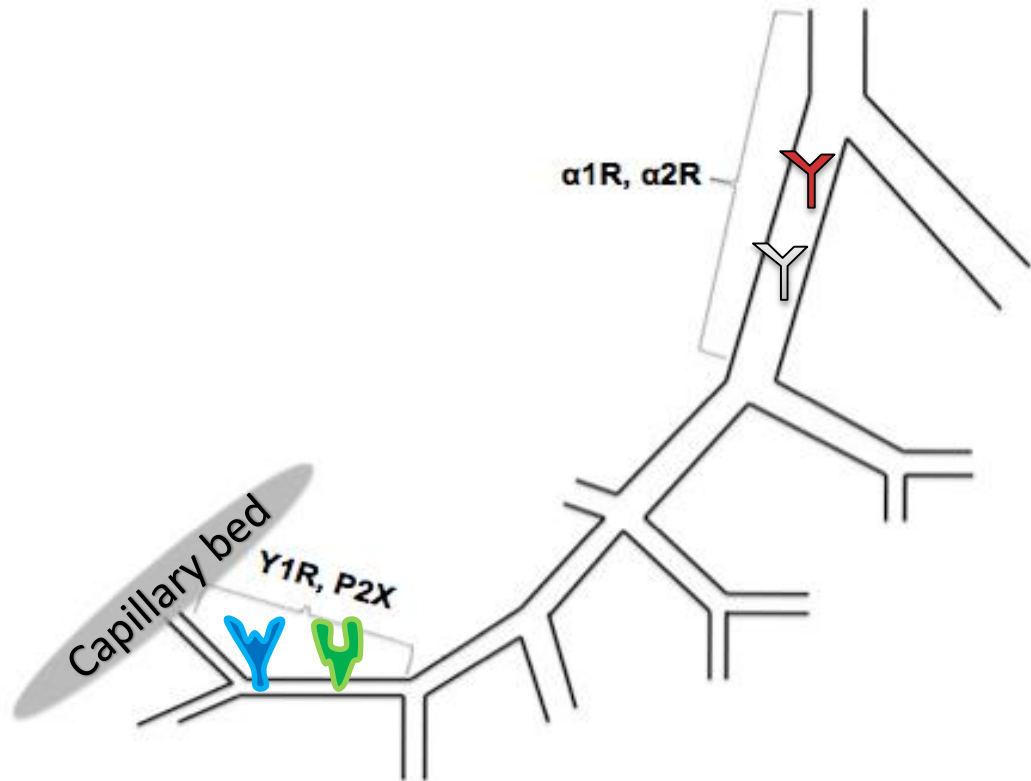


Figure 1.1: Topologically-dependent SNS receptor functionality.

Summary of SNS receptor functionality as a function of network topology. Based on previous literature, it is hypothesized that there is a progressively decreasing sensitivity to adrenergic ($\alpha 1R$ and $\alpha 2R$) receptor activation with increasing branch order (towards distal, pre-terminal arterioles that branch into the capillary bed), and a progressively decreasing sensitivity to purinergic and peptidergic receptor activation with decreasing branch order (towards proximal, inlet arterioles).

Since arteriolar network geometry (i.e., topology) plays a considerable role in setting network resistance, it necessarily follows that acute control of arteriolar diameter must coordinate with topology in order to regulate microvascular blood flow and RBC distribution efficiently. Currently, the impact of microvascular topology on sympathetically-mediated arteriolar control is unknown. The importance of assessing microvascular network hemodynamics has been either overlooked or not experimentally feasible.

1.7 Importance of network topology in microvascular regulation

Blood flow to capillary beds is affected by upstream vasoregulation (e.g., upstream dilation/constriction) (Segal *et al.*, 1989), topology, morphology, and hemodynamic parameters (Zweifach, 1974; Pries *et al.*, 1986; Duling & Damon, 1987; Pries *et al.*, 1995). Skeletal muscle microvascular data are predominantly collected from single microvessels within a network (VanTeeffelen & Segal, 2006; Moore *et al.*, 2010; Frisbee *et al.*, 2011), and the remaining network data are extrapolated from the experimentally collected data (Duling *et al.*, 1982). However, with the existence of blood flow heterogeneity in skeletal muscle microvasculature (Duling & Damon, 1987), it becomes necessary to collect data from more complete networks (Pries *et al.*, 1986; Pries *et al.*, 1995) as opposed to single sites of observation.

Blood can be described as a two-phase fluid, comprised of both red blood cell and plasma components. When blood meets a bifurcation, there may be uneven distribution of the red blood cell fraction (i.e., hematocrit) between the two daughter vessels, which contributes to the heterogeneous level of red blood cell distribution within a vascular network.

Therefore, even within a single bifurcation there may be differences in hematocrit in individual segments that will ultimately affect hematocrit at the level of the capillaries (Pries *et al.*, 1996).

Blood flow supplied to the microvasculature is also affected by the architecture of the supplied downstream network. As microvascular networks are more than an interconnected set of isolated vessels, changes in demand at the capillary end can be communicated to the preceding branches in order to receive the required level of adequate blood flow supply. As summarized by Bearden, signals are sent from the downstream vessels along the length of a vessel upstream, and are categorized as intercellular, mechanical, or countercurrent forms of communication (Bearden, 2006). Intercellular communication occurs when a segment of a vessel is exposed to a vasomotor stimuli, and sends a vasomotor signal upstream to a part of the network that is not experiencing the same stimulus to cause remote changes in vasodilation upstream (Segal & Duling, 1987). Mechanical communication is illustrated when downstream dilation causes an increase in shear stress upstream. Countercurrent communication describes the communication between a venule and an arteriole, through which the tissue can send a signal (via release of a vasoactive substance) to cause a dilation in upstream arterioles. As illustrated, the inherent network connectivity present in microvascular networks precludes complete acquisition of hemodynamic data from single sites of observation. Therefore, to more thoroughly investigate hemodynamic parameters within a network, it is pertinent to incorporate downstream and upstream changes in parameters, as well as network geometry and morphology.

Although experimental data on skeletal muscle microvascular hemodynamics are limited, the tenacious efforts of Pries, Secomb and their collaborators have greatly contributed to network hemodynamic analysis via decades of seminal work on microvascular networks from the rat mesentery. As it is experimentally difficult to acquire data from all segments within a network, Pries *et al.* have mastered the photomontage technique and collected experimental data that are complemented by computational simulations to assess full network hemodynamics (Pries *et al.*, 1986; Pries *et al.*, 1990; Pries *et al.*, 1994). This approach has been very useful in simulating network structural adaptations to elevated pressure (Pries *et al.*, 2001b), angio-adaptation in tumor microvascular networks (Secomb *et al.*, 2012), and general adaptations of the terminal network to changes in tissue demands (Pries *et al.*, 2001a). Much of the advances made in microvascular network flow simulations can be accredited to their work. With the development of more network-accessible skeletal muscle preparations, the experimentally collected and computationally simulated approach to data collection would serve as a powerful technique in calculating valuable hemodynamic data in skeletal muscle microvascular networks.

1.8 Where has skeletal muscle microvasculature classically been studied?

The first description of a systemic circulation was given by William Harvey in the early 1600s. In 1661, nearly 4 years after Harvey's death, Marcello Malpighi observed blood flowing through small tubes (nowadays known as capillaries) in the frog. He was the first to assert that capillaries were the connection between arteries and veins, thereby completing the systemic circuitry that was first laid out by Harvey (Pearce, 2007).

The majority of our understanding on microvascular regulation in skeletal muscle tissues comes from experiments conducted on *in vivo* preparations, all notably described in the 1973 5th Volume of the *Microvascular Research* journal. These preparations [namely the rat cremaster (Baez, 1973), hamster cheek pouch (Duling, 1973), rat spinotrapezius (Gray, 1973), and cat sartorius (Burton, 1973)] revolutionized microvascular research and pushed past the previous limits of *in vivo* research, launching a new realm of in-depth microvascular regulation studies.

The definitive objective of an *in vivo* skeletal muscle microvascular preparation is to best recreate the endogenous environment, while providing an opportunity to manipulate and observe the regulation of control systems within microvascular networks. The development of a functional, *in vivo* skeletal muscle preparation for intravital video microscopy is a difficult feat. Each step in the procedure must be executed with great care: from animal handling, to finely exposing the tissue with minimal surgical trauma and maintaining both the preparation and animal under stable conditions throughout the course of the experiment.

In 1961, the cremaster muscle was described as a valuable model for microvascular observation (Grant, 1964). This method of cremaster preparation was limited as there were three key characteristics which constrained the view of the microcirculatory network: a) curvature of the testes was left *in situ* thus creating a smaller field of view; b) the preparation oscillated with respiration; and c) the vessels found in the tunica albuginea lining of the cremaster provided a poor background of contrast for the cremaster vessels. As a means to evade the anatomical obstructions, a white enamel spatula was introduced through an abdominal incision to prevent curvature of the

preparation (thereby increasing its field of view), to better secure the muscle *in situ* (therefore preventing respiratory artifacts in imaging), and to provide a white background for imaging cremaster microcirculation (an improvement from the low-contrast vascularized tunica albuginea background) (Majno *et al.*, 1967). While introduction of the white enamel spatula improved the imaging quality of the cremaster microcirculation, it, along with the original method proposed by Grant *et al.*, depended on incident light illumination for microvascular imaging. This type of imaging can only be carried out under low magnification conditions, thereby preventing imaging at the resolution necessary for identifying a clear boundary between the lumen and the wall of the vessel.

To circumvent aforementioned obstructions to imaging, a detailed method was described in 1973 that involved fully opening and exposing the cremaster muscle, as well as implementing transillumination in lieu of incident light illumination (Baez, 1973). Fully opening up the cremaster along with the use of transillumination proved to be a powerful combination as this allowed, for the first time since the conception of utilizing the cremaster for microcirculatory observations, data collection from a large field of view as well as clearly defined borders between the lumen and vessel wall in the cremaster muscle.

The hamster cheek pouch was first described as a preparation for observing microcirculation in the late 1940's and early 1950's (Fulton *et al.*, 1947; Lutz & Fulton, 1954). In 1973, the hamster cheek pouch preparation for acute experimentation, its anatomical characteristics, and functional responses (to acetylcholine and oxygen) were described in full detail. This preparation has been praised for: 1) its dual nature in cell types (its anatomy involves a cheek skin pouch that is retained by a thin retractor muscle

(Grasby *et al.*, 1999), thereby possessing both striated muscle and cutaneous circulatory beds) providing the ability to conduct comparative studies, 2) being a thin tissue which is ideal for tissue transillumination and improving clarity of microvessel observations, and 3) providing visual access to multiple consecutive branch orders. While this preparation has lent its utility to the study of blood flow regulation in skeletal muscle, there exist important anatomical differences between the retractor muscle and true locomotor muscles and therefore may limit its generalisability to non-locomotor muscles (Loeb *et al.*, 1987; Williams & Segal, 1993; Welsh & Segal, 1997).

The spinotrapezius skeletal muscle preparation was introduced by Zweifach and Metz in 1955 (Zweifach & Metz, 1955), and its preparation was first described in detail by Hyman and Paldino who used the spinotrapezius to study local temperature regulation (Hyman & Paldino, 1962). Since then, the preparation was refined and modified (Gray, 1973), and has been used in recent work (Chen *et al.*, 2013). Due to the thickness of this muscle, the spinotrapezius has been used to measure capillary hemodynamics during muscle contractions (Bailey *et al.*, 2000; Richardson *et al.*, 2003). This locomotor muscle has been difficult to study during exercise paradigms as rodent treadmill experiment paradigms (the conventional training program used during exercise experimentation) do not activate the spinotrapezius, and in fact reduce blood flow within the muscle (Musch & Poole, 1996). It has been shown that the spinotrapezius is activated during downhill running; an eccentric movement that has been shown to elicit powerful muscle contractions (Meyer *et al.*, 2003) and induces muscle adaptation (Clarkson *et al.*, 1992) despite the potential muscle damage that may be accompanied with such exercise (Kano *et al.*, 2004a; Kano *et al.*, 2004b).

The cat sartorius muscle preparation was developed for microcirculatory studies as it exhibits two ideal characteristics necessary for improved visualization of the microvessels: thinness for optimized transillumination, and a parallel muscle fiber layout. Another key benefit to utilizing the cat sartorius muscle was that its blood supply (primarily, lateral circumflex femoral artery and vein; secondarily, femoral artery and vein) can be cannulated (Burton & Johnson, 1972; Burton, 1973), which is the ideal method for acquiring total flow to a tissue during hemodynamic experiments where data can then be used as inputs for experimental modelling. Of particular importance, the frog sartorius was extensively used by Tyml *et al.* to provide some of the first evidence showing the capillary as a medium of communication in the microvasculature (Dietrich & Tyml, 1992), as well as for highlighting the importance of capillary recruitment and blood flow heterogeneity within capillaries (Tyml, 1986). Although the sartorius muscle is simple to exteriorize, at its thinnest region, it may have up to 15 muscle fibers with capillaries exhibiting countercurrent flow near adjacent muscle fibers (Sullivan & Pittman, 1982).

In most preparations, thick fascia tissue hinders microvascular visibility, which limits the age range to younger subjects as they have less fascia tissue; however, this prevents the conduction of aging studies. The rat extensor digitorum longus (EDL) preparation was developed with the incentive that it would be an *in vivo* skeletal muscle preparation that provides good microvascular visibility independent of animal age or size (Tyml & Budreau, 1991). As the EDL is a tubular muscle, deep in the hindlimb muscles, where capillary beds and their small venules are easily observed at the surface of the muscle. A coverslip is placed on the muscle and is used to a) prevent air exposure to the muscle,

thus bypassing the use of superfusion (as employed by other studies), b) stabilizes preparation from breathing artifacts, and c) enables good visualization for use in epi-illumination. With this set-up and the microvascular anatomy of the preparation itself, live imaging of red blood cell velocity and perfused capillary density is possible. The major benefits of this preparation are a) it is a true locomotive skeletal muscle, b) the preparation can be used independent of animal age or size, c) does not depend on use of superfusion for stability, and d) can be used with a coverslip to maximize the field of view size (Tymml & Budreau, 1991). Despite the many benefits of the EDL preparation, its primary utility lies in the investigation of capillary beds, as its tubular anatomy does not allow access to a microvascular network. That is, the feed arteriole/exiting venule are embedded closer to the middle; subsequent vessels then bifurcate towards the surface of the muscle, where only capillaries are visible. As well, another drawback to the use of the coverslip is it does not allow for hemodynamic investigation of drug perturbations, which would otherwise have been easily dissolved in a superfusate solution flowing over the muscle.

These described preparations have been integral in providing a window into the microcirculation, a once ambitious experimental feat to have overcome. In addition, it is noteworthy to mention non-skeletal muscle preparations such as the rat mesenteric bed (McGregor, 1965), rabbit ear (Ahern *et al.*, 1949), and bat wing (Nicoll & Webb, 1946) that have also greatly contributed to the knowledge base of microvascular regulation.

1.9 How has skeletal muscle microcirculation classically been imaged?

The establishment of many viable models for visualizing the microcirculation was conveniently conducted in tandem with the development of techniques for quantifying red blood cell velocity and flow hemodynamics in microvessels. The different techniques were developed under various experimental conditions and are dependent upon many contributing factors (i.e., type/method of illumination, size of vessel, magnification, and cell velocity). Initially, observation of the microcirculation utilized a visual method approach, which was then followed by photographic methods; however, the majority of today's techniques either include to some capacity or directly evolve from electro-optical methods.

A complete, yet brief, history of red blood cell velocity quantification is described by Wiedeman *et al.*, (Wiedeman *et al.*, 1981) where they state the first attempt at visually determining the velocity of a red cell was made in the late 17th century by Anton Van Leeuwenhoek when he observed how far a red cell would travel in the time it took for him to recite four syllables. He concluded that the velocity of a red cell was $2 \text{ mm}\cdot\text{sec}^{-1}$, which is remarkably similar to what is measured today. There was a single criterion that had to have been met in order for Leeuwenhoek to determine the red cell velocity with such accuracy: he would have needed to observe and track either one cell or a small group of cells at a time in order to allow him to confidently obtain velocity measurements. The visual methods that followed Leeuwenhoek's measurement technique also pursued a similar timed-interval-of-travel course of action, although velocity measurements were limited to values of $2 \text{ mm}\cdot\text{sec}^{-1}$. This was accepted as a limitation in

microcirculatory observation up until the 1960's, when Monro developed a novel streak-image technique that measured up to $16 \text{ mm}\cdot\text{sec}^{-1}$ velocities by taking advantage of the human retina's ability to accurately measure the angle at which streaks of light (remains of fast moving objects) would pass in front of it (Wiedeman *et al.*, 1981).

Photographic, unlike visual, methods have the advantage of allowing measurements to be made off-line, and by multiple observers. These methods, however, also come with criteria which must be met prior to their use: a) the same target or cell must be in two consecutive image frames for a set interval of time between frames, and b) there must be high enough resolution to distinguish the target or cell in a given frame. In order to ensure that the first criterion is met, only one target must have passed in a pair of subsequent frames collected over a finite period of time, thereby necessitating use of high enough frame rates that would ensure the object has not passed by the time the second frame is captured.

By ensuring that the target is not in a state of transit during frame acquisition, the second criterion is met; the target must not be moving faster than the shutter speed, or the rate at which the image was taken. In this context, one is left with the issue of balancing shutter speed and frame rate. Too low of an exposure time does not allow enough light to enter the shutter leaving the potential for lower contrast in imaging. High exposure times improve contrast, however this is achieved at the expense of catching the target in transition (i.e., not still) as well as slowing down frame rate. Cinephotography was the preferred method of data acquisition for the photographic approach to measuring velocities. Although, high frame rates are required, this technique would require

unfeasibly large amounts of film in order to store the images for off-line analysis (Wiedeman *et al.*, 1981).

Both the visual and photographic methods rely on high contrast visibility of the target. The single red blood cell against the plasma provides high contrast for imaging. Thus, the eye recognizes the red cell itself as it exhibits a different light intensity compared to the formed plasma gaps found between each red cell. This visual algorithm can be implemented electronically by using electro-optical techniques, where a sensor is used to differentiate between the varying light intensities of the red cell and the plasma gaps. The sensor converts the light information into a signal with amplitude corresponding to the light intensity. If this sensor is fixed in a single position on a vessel, then it can detect red blood cell flow patterns as a function of time. Taking it one step further, if two sensors are placed at two different locations in a vessel, with the same cell flowing past each of the two sensors, then fixed distance between the two sensors must be traveled in the time it took for the single cell to pass from the first to the second sensor.

According to Wiedeman *et al.*, Müller was the first to execute an electro-optical technique in microcirculatory imaging in the early 1960's (Wiedeman *et al.*, 1981), and Wayland and Johnson later refined the method in the late 1960s. Wayland and Johnson used a photomultiplier tube as a sensor for detecting light (to increase the range of light that can be detected), and added two sensors instead of just one, which allowed them to account for the time of travel between the two sensors that were fixed in position. These adjustments (Wayland & Johnson, 1967) were pivotal in changing microvascular imaging, and the theories behind the two-slit photometric imaging technique remain to be one of the most widely used techniques in microvascular hemodynamic quantification.

The utility of the two-slit photometric method is accompanied by specific assumptions; namely, the red blood cell flow pattern (distance of the plasma gap occupied by two red cells) is assumed to remain constant in length as it travels between the upstream and downstream photo sensors. With regards to practicality, there are a number of limitations (Sapuppo *et al.*, 2004) associated to the original technique: 1) system parameters (e.g., system's clock frequency) must first be manually modified to give information about velocity, leaving room for operator bias; 2) correlated velocity peaks only give one velocity measurement resulting in non-reproducible values; 3) data cannot be saved in digital format; 4) although the system collects data in real-time, it does not cross-correlate peaks between the two sensors automatically, which does not allow the system to follow the time changes of velocity, thereby only providing average velocity values. In a recent study (Roman *et al.*, 2012), the dual-slit technique was replaced by two regions of interest in a simulation involving computer-generated image sequences of red blood cells flowing through a tube. This allowed for the control of hematocrit and velocity profile; two factors known to influence the outcome of dual-sensor measurements conducted on vessels that are larger than capillaries (i.e., non-single file flow vessels) (Pittman & Ellsworth, 1986; Roman *et al.*, 2012).

Laser Doppler velocimetry is a method which takes advantage of coherent light scattering, and infers changes in particle velocities based on the Doppler shift in laser light. When a laser light strikes biological tissue, a portion of the light will reflect back from static tissue with the same incident frequency. The other portion of light will reflect from moving particles (specifically, red blood cells), and experience a shift in frequency as a result of the Doppler shift (Nilsson *et al.*, 1980). However, due to Doppler

velocimetry's dependence on incident angle of the light, an issue arises with imaging microvascular beds as the directionality of blood flow is found in random orientations. To resolve this, a technique was developed which incorporated use of a uni-dimensional fringe pattern formation atop the region of interest (kept at an angle normal to the blood stream), and as blood particles passes the bands of the fringe pattern, reflections in the light bands are picked up by a photodetector (Le-Cong & Zweifach, 1979). These reflections are interpreted by the Doppler shift principle, are directly related to the number of red cells, and quantified as velocity measurements. The advantages of this technique are that it is non-invasive, does not require tracers or particle labeling, and allows for longitudinal tissue perfusion monitoring without influencing blood flow regulation in the tissue. This technique is limited by the lack of standardized interpretation available for the measured signals, use of arbitrary units, and its inability to be calibrated to units relevant to perfusion.

More recently, technological advances in ultra high-speed cameras and imaging microscopy have launched the acquisition of whole velocity fields in microvessels through the development of particle image velocimetry (PIV). This technique is used to reconstruct velocity profiles by measuring the instantaneous two- or three-dimensional velocity vector fields of particles seeded in flow. In microcirculation, PIV has been subjected to difficulties with optimal resolving power and out-of-focus effects of the microscopy system. Macro-PIV, or application of PIV to large-scale flows (e.g., such as in mechanical engineering practices) acquires velocity field vector data by illuminating a single 2-dimensional plane with lasers, and correlating wavelengths emitted by seeded particles with directional flow. Micro-PIV (μ -PIV), or application of PIV to small-scale

flows (e.g., micro-channels and microvasculature), requires illumination of the entire channel. This provides great loss of accuracy in vector field information as velocities are simultaneously collected from multiple stacked fields within the channel or microvessel and averaged in the orthogonal or z-direction.

To circumvent axial averaging errors, μ -PIV has been implemented with use of confocal microscopy to acquire single planes of velocity vector field data. Although coupling of confocal microscopy with μ -PIV is an advancement, the issue remains that use of a RBC as a particle tracker in μ -PIV may not provide high enough resolution for near-wall interactions due to the existence of the cell-free layer in microvessels (Popel & Johnson, 2005).

The optical section thickness for velocity data acquisition is largely dependent on the numerical aperture (NA) of the objective, where higher (compared to lower) NA values resolve thinner volume measurements and is commonly specified by the depth-of-field for a given microscope system. It is often the case that depth-of-field is mistaken for the absolute thickness of tissue under microscopic observation. In fact, this thickness, predicted using a Gaussian intensity distribution, is called depth-of-correlation and is largely dependent on the size of the tracer particle (Poelma *et al.*, 2012). Depth-of-correlation indicates a particle's contribution to the averaging of cross-correlated particle tracer velocities. Due to this depth-of-correlation parameter, both artificial and naturally occurring particle tracers (RBCs) provide identical blood flow measurements at low magnifications (Poelma *et al.*, 2012).

1.10 Purpose of thesis dissertation

The SNS has a vital role in maintaining microvascular network resistance in skeletal muscle microcirculation. Previous findings confirm that the SNS has differential control over the span of a microvascular network, and that the varying levels of control may be attributed to heterogeneous functional distribution of the SNS receptors within the network (Fig. 1.1). Despite the evidence for a relationship between the functionality of each SNS receptor and vascular diameter, there remains to be a comprehensive evaluation of receptor activation in a skeletal muscle microvascular network. These shortcomings are partly due to the absence of a single skeletal muscle microvascular preparation that provides access to a complete network for evaluation of SNS receptor activation along the network.

Moreover, the prominent role of the SNS in microvascular control presents a strong case for the SNS having an intimate role in skeletal muscle hemodynamics. However, the current set of blood flow measurement techniques is not conducive to assessing the role of the SNS in skeletal muscle microvascular hemodynamics (e.g., RBC velocity, flow, wall shear rate). Some of the limitations presented by the previously mentioned blood flow techniques are: 1) spatial averaging which poses the risk of over- or under-estimating blood flow calculations within a vessel segment, 2) difficulty in acquiring measures from fast-flowing arterioles, 3) use of non-native tracers (i.e., not naturally found in blood), and 4) in-depth post-experiment computation preventing fast data acquisition.

To this end, the objectives of the thesis herein are to: 1) develop a viable *in vivo* skeletal muscle preparation for use with intravital video microscopy that provides access to a complete microvascular network, 2) develop a blood flow measurement technique for acquisition and calculation of *in vivo* hemodynamic parameters (i.e., RBC velocity, flow, and shear rate), 3) characterize SNS receptor functional distribution along the network, and 4) assess how SNS receptor activation along the network affects skeletal muscle microvascular hemodynamics within various levels of the network. We hypothesize a topologically-dependent SNS receptor functionality, with adrenergic receptor activation primarily governing the proximal vessels and peptidergic and purinergic receptor activation primarily governing the distal vessels (Fig. 1.1).

1.11 References

- Ahern JJ, Barclay WR & Ebert RH. (1949). Modifications of the rabbit ear chamber technique. *Science* **110**, 665.
- Andersen P & Saltin B. (1985). Maximal perfusion of skeletal muscle in man. *J Physiol* **366**, 233-249.
- Anderson RL, Gibbins IL & Morris JL. (1996). Non-noradrenergic sympathetic neurons project to extramuscular feed arteries and proximal intramuscular arteries of skeletal muscles in guinea-pig hindlimbs. *J Auton Nerv Syst* **61**, 51-60.
- Baez S. (1973). An open cremaster muscle preparation for the study of blood vessels by in vivo microscopy. *Microvasc Res* **5**, 384-394.
- Bailey JK, Kindig CA, Behnke BJ, Musch TI, Schmid-Schoenbein GW & Poole DC. (2000). Spinotrapezius muscle microcirculatory function: effects of surgical exteriorization. *Am J Physiol Heart Circ Physiol* **279**, H3131-3137.
- Bearden SE. (2006). Effect of aging on the structure and function of skeletal muscle microvascular networks. *Microcirculation* **13**, 279-288.
- Boegehold MA & Johnson PC. (1988). Response of arteriolar network of skeletal muscle to sympathetic nerve stimulation. *Am J Physiol* **254**, H919-928.

- Brothers SP & Wahlestedt C. (2010). Therapeutic potential of neuropeptide Y (NPY) receptor ligands. *EMBO Mol Med* **2**, 429-439.
- Burton KS. (1973). Cat sartorius muscle: an isolated perfused skeletal muscle preparation for microvascular research. *Microvasc Res* **5**, 401-409.
- Burton KS & Johnson PC. (1972). Reactive hyperemia in individual capillaries of skeletal muscle. *Am J Physiol* **223**, 517-524.
- Bylund DB. (1992). Subtypes of alpha 1- and alpha 2-adrenergic receptors. *FASEB J* **6**, 832-839.
- Chen B, Mutschler M, Yuan Y, Neugebauer E, Huang Q & Maegele M. (2013). Superimposed traumatic brain injury modulates vasomotor responses in third-order vessels after hemorrhagic shock. *Scand J Trauma Resusc Emerg Med* **21**, 77.
- Clarkson PM, Nosaka K & Braun B. (1992). Muscle function after exercise-induced muscle damage and rapid adaptation. *Med Sci Sports Exerc* **24**, 512-520.
- Dietrich HH & Tysl K. (1992). Capillary as a communicating medium in the microvasculature. *Microvasc Res* **43**, 87-99.
- Dodd LR & Johnson PC. (1991). Diameter changes in arteriolar networks of contracting skeletal muscle. *Am J Physiol* **260**, H662-670.
- Duling BR. (1973). The preparation and use of the hamster cheek pouch for studies of the microcirculation. *Microvasc Res* **5**, 423-429.
- Duling BR & Damon DH. (1987). An examination of the measurement of flow heterogeneity in striated muscle. *Circ Res* **60**, 1-13.
- Duling BR, Sarelius IH & Jackson WF. (1982). A comparison of microvascular estimates of capillary blood flow with direct measurements of total striated muscle flow. *Int J Microcirc Clin Exp* **1**, 409-424.
- Ekelund U & Erlinge D. (1997). In vivo receptor characterization of neuropeptide Y-induced effects in consecutive vascular sections of cat skeletal muscle. *Br J Pharmacol* **120**, 387-392.
- Exton JH. (1996). Regulation of phosphoinositide phospholipases by hormones, neurotransmitters, and other agonists linked to G proteins. *Annu Rev Pharmacol Toxicol* **36**, 481-509.
- Faber JE. (1988). In situ analysis of alpha-adrenoceptors on arteriolar and venular smooth muscle in rat skeletal muscle microcirculation. *Circ Res* **62**, 37-50.

- Fleming BP, Gibbins IL, Morris JL & Gannon BJ. (1989). Noradrenergic and peptidergic innervation of the extrinsic vessels and microcirculation of the rat cremaster muscle. *Microvasc Res* **38**, 255-268.
- Frisbee JC, Wu F, Goodwill AG, Butcher JT & Beard DA. (2011). Spatial heterogeneity in skeletal muscle microvascular blood flow distribution is increased in the metabolic syndrome. *Am J Physiol Regul Integr Comp Physiol* **301**, R975-986.
- Fronek K & Zweifach BW. (1975). Microvascular pressure distribution in skeletal muscle and the effect of vasodilation. *Am J Physiol* **228**, 791-796.
- Fu Q & Levine BD. (2014). Pathophysiology of neurally mediated syncope: Role of cardiac output and total peripheral resistance. *Auton Neurosci* **184**, 24-26.
- Fulton GP, Jackson RG & Lutz BR. (1947). Cinephotomicroscopy of normal blood circulation in the cheek pouch of the hamster. *Science* **105**, 361-362.
- Fuxe K & Sedvall G. (1965). The Distribution of Adrenergic Nerve Fibres to the Blood Vessels in Skeletal Muscle. *Acta Physiol Scand* **64**, 75-86.
- Gitterman DP & Evans RJ. (2000). Properties of P2X and P2Y receptors are dependent on artery diameter in the rat mesenteric bed. *Br J Pharmacol* **131**, 1561-1568.
- Grant RT. (1964). Direct Observation of Skeletal Muscle Blood Vessels (Rat Cremaster). *J Physiol* **172**, 123-137.
- Grasby DJ, Morris JL & Segal SS. (1999). Heterogeneity of vascular innervation in hamster cheek pouch and retractor muscle. *J Vasc Res* **36**, 465-476.
- Gray SD. (1973). Rat spinotrapezius muscle preparation for microscopic observation of the terminal vascular bed. *Microvasc Res* **5**, 395-400.
- Hirsch D & Zukowska Z. (2012). NPY and stress 30 years later: the peripheral view. *Cell Mol Neurobiol* **32**, 645-659.
- Hyman C & Paldino RL. (1962). Local temperature regulation of microtissue clearance from rat skeletal muscle. *Circ Res* **10**, 89-93.
- Iversen PO & Nicolaysen G. (1989). Heterogeneous blood flow distribution within single skeletal muscles in the rabbit: role of vasomotion, sympathetic nerve activity and effect of vasodilation. *Acta Physiol Scand* **137**, 125-133.
- Jackson DN, Noble EG & Shoemaker JK. (2004). Y1- and alpha1-receptor control of basal hindlimb vascular tone. *Am J Physiol Regul Integr Comp Physiol* **287**, R228-233.

- Janssen I, Heymsfield SB, Wang ZM & Ross R. (2000). Skeletal muscle mass and distribution in 468 men and women aged 18-88 yr. *J Appl Physiol (1985)* **89**, 81-88.
- Kano Y, Padilla D, Hageman KS, Poole DC & Musch TI. (2004a). Downhill running: a model of exercise hyperemia in the rat spinotrapezius muscle. *J Appl Physiol (1985)* **97**, 1138-1142.
- Kano Y, Sampei K & Matsudo H. (2004b). Time course of capillary structure changes in rat skeletal muscle following strenuous eccentric exercise. *Acta Physiol Scand* **180**, 291-299.
- Koga S, Rossiter HB, Heinonen I, Musch TI & Poole DC. (2014). Dynamic heterogeneity of exercising muscle blood flow and O₂ utilization. *Med Sci Sports Exerc* **46**, 860-876.
- Lambert DG & Thomas GD. (2005). α -Adrenoceptor constrictor responses and their modulation in slow-twitch and fast-twitch mouse skeletal muscle. *J Physiol* **563**, 821-829.
- Le-Cong P & Zweifach BW. (1979). In vivo and in vitro velocity measurements in microvasculature with a laser. *Microvasc Res* **17**, 131-141.
- Loeb GE, Pratt CA, Chanaud CM & Richmond FJ. (1987). Distribution and innervation of short, interdigitated muscle fibers in parallel-fibered muscles of the cat hindlimb. *J Morphol* **191**, 1-15.
- Lutz BR & Fulton GP. (1954). The use of the hamster cheek pouch for the study of vascular changes at the microscopic level. *Anat Rec* **120**, 293-307.
- Mackie BG & Terjung RL. (1983). Blood flow to different skeletal muscle fiber types during contraction. *Am J Physiol* **245**, H265-275.
- Majno G, Gilmore V & Leventhal M. (1967). A technique for the microscopic study of blood vessels in living striated muscle (cremaster). *Circ Res* **21**, 823-832.
- Marshall JM. (1982). The influence of the sympathetic nervous system on individual vessels of the microcirculation of skeletal muscle of the rat. *J Physiol* **332**, 169-186.
- McGregor DD. (1965). The Effect of Sympathetic Nerve Stimulation of Vasoconstrictor Responses in Perfused Mesenteric Blood Vessels of the Rat. *J Physiol* **177**, 21-30.
- Meyer K, Steiner R, Lastayo P, Lippuner K, Allemann Y, Eberli F, Schmid J, Saner H & Hoppeler H. (2003). Eccentric exercise in coronary patients: central hemodynamic and metabolic responses. *Med Sci Sports Exerc* **35**, 1076-1082.

- Moore AW, Jackson WF & Segal SS. (2010). Regional heterogeneity of alpha-adrenoreceptor subtypes in arteriolar networks of mouse skeletal muscle. *J Physiol* **588**, 4261-4274.
- Mortensen SP, Nyberg M, Winding K & Saltin B. (2012). Lifelong physical activity preserves functional sympatholysis and purinergic signalling in the ageing human leg. *J Physiol* **590**, 6227-6236.
- Musch TI & Poole DC. (1996). Blood flow response to treadmill running in the rat spinotrapezius muscle. *Am J Physiol* **271**, H2730-2734.
- Naik JS, Valic Z, Buckwalter JB & Clifford PS. (1999). Rapid vasodilation in response to a brief tetanic muscle contraction. *J Appl Physiol (1985)* **87**, 1741-1746.
- Nicoll PA & Webb RL. (1946). Intermittency of blood flow in peripheral fields. *Fed Proc* **5**, 76.
- Nilsson GE, Tenland T & Oberg PA. (1980). Evaluation of a laser Doppler flowmeter for measurement of tissue blood flow. *IEEE Trans Biomed Eng* **27**, 597-604.
- O'Connell TD, Jensen BC, Baker AJ & Simpson PC. (2014). Cardiac alpha1-adrenergic receptors: novel aspects of expression, signaling mechanisms, physiologic function, and clinical importance. *Pharmacol Rev* **66**, 308-333.
- Oates HF, Graham RM, Stoker LM & Stokes GS. (1976). Haemodynamic effects of prazosin. *Arch Int Pharmacodyn Ther* **224**, 239-247.
- Ohyanagi M, Faber JE & Nishigaki K. (1991). Differential activation of alpha 1- and alpha 2-adrenoceptors on microvascular smooth muscle during sympathetic nerve stimulation. *Circ Res* **68**, 232-244.
- Pearce JM. (2007). Malpighi and the discovery of capillaries. *Eur Neurol* **58**, 253-255.
- Pittman RN & Ellsworth ML. (1986). Estimation of red cell flow microvessels: consequences of the Baker-Wayland spatial averaging model. *Microvasc Res* **32**, 371-388.
- Poelma C, Kloosterman A, Hierck BP & Westerweel J. (2012). Accurate blood flow measurements: are artificial tracers necessary? *PLoS One* **7**, e45247.
- Poole DC, Copp SW, Ferguson SK & Musch TI. (2013). Skeletal muscle capillary function: contemporary observations and novel hypotheses. *Exp Physiol* **98**, 1645-1658.
- Popel AS & Johnson PC. (2005). Microcirculation and Hemorheology. *Annu Rev Fluid Mech* **37**, 43-69.

- Pries AR, Ley K & Gaehtgens P. (1986). Generalization of the Fahraeus principle for microvessel networks. *Am J Physiol* **251**, H1324-1332.
- Pries AR, Reglin B & Secomb TW. (2001a). Structural adaptation of microvascular networks: functional roles of adaptive responses. *Am J Physiol Heart Circ Physiol* **281**, H1015-1025.
- Pries AR, Reglin B & Secomb TW. (2001b). Structural adaptation of vascular networks: role of the pressure response. *Hypertension* **38**, 1476-1479.
- Pries AR, Secomb TW & Gaehtgens P. (1995). Structure and hemodynamics of microvascular networks: heterogeneity and correlations. *Am J Physiol* **269**, H1713-1722.
- Pries AR, Secomb TW & Gaehtgens P. (1996). Biophysical aspects of blood flow in the microvasculature. *Cardiovasc Res* **32**, 654-667.
- Pries AR, Secomb TW, Gaehtgens P & Gross JF. (1990). Blood flow in microvascular networks. Experiments and simulation. *Circ Res* **67**, 826-834.
- Pries AR, Secomb TW, Gessner T, Sperandio MB, Gross JF & Gaehtgens P. (1994). Resistance to blood flow in microvessels in vivo. *Circ Res* **75**, 904-915.
- Richardson TE, Kindig CA, Musch TI & Poole DC. (2003). Effects of chronic heart failure on skeletal muscle capillary hemodynamics at rest and during contractions. *J Appl Physiol (1985)* **95**, 1055-1062.
- Roman S, Lorthois S, Duru P & Risso F. (2012). Velocimetry of red blood cells in microvessels by the dual-slit method: effect of velocity gradients. *Microvasc Res* **84**, 249-261.
- Rowell LB, Blackmon JR & Bruce RA. (1964). Indocyanine Green Clearance and Estimated Hepatic Blood Flow during Mild to Maximal Exercise in Upright Man. *J Clin Invest* **43**, 1677-1690.
- Saltzman D, DeLano FA & Schmid-Schonbein GW. (1992). The microvasculature in skeletal muscle. VI. Adrenergic innervation of arterioles in normotensive and spontaneously hypertensive rats. *Microvasc Res* **44**, 263-273.
- Sapuppo F, Longo D, Bucolo M, Intaglietta M, Arena P & Fortuna L. (2004). Real time blood flow velocity monitoring in the microcirculation. *Conf Proc IEEE Eng Med Biol Soc* **3**, 2219-2222.
- Secomb TW, Dewhirst MW & Pries AR. (2012). Structural adaptation of normal and tumour vascular networks. *Basic Clin Pharmacol Toxicol* **110**, 63-69.

- Segal SS. (2005). Regulation of blood flow in the microcirculation. *Microcirculation* **12**, 33-45.
- Segal SS, Damon DN & Duling BR. (1989). Propagation of vasomotor responses coordinates arteriolar resistances. *Am J Physiol* **256**, H832-837.
- Segal SS & Duling BR. (1987). Propagation of vasodilation in resistance vessels of the hamster: development and review of a working hypothesis. *Circ Res* **61**, II20-25.
- Sullivan SM & Pittman RN. (1982). Hamster retractor muscle: a new preparation for intravital microscopy. *Microvasc Res* **23**, 329-335.
- Sundler F, Böttcher G, Ekblad E & Håkanson R. (1993). PP, PYY and NPY, occurrence and distribution in the periphery. *The Biology of Neuropeptide Y and Related Peptides*, 157-196.
- Surprenant A & North RA. (2009). Signaling at purinergic P2X receptors. *Annu Rev Physiol* **71**, 333-359.
- Thomas GD, Hansen J & Victor RG. (1994). Inhibition of alpha 2-adrenergic vasoconstriction during contraction of glycolytic, not oxidative, rat hindlimb muscle. *Am J Physiol* **266**, H920-929.
- Tyml K. (1986). Capillary recruitment and heterogeneity of microvascular flow in skeletal muscle before and after contraction. *Microvasc Res* **32**, 84-98.
- Tyml K & Budreau CH. (1991). A new preparation of rat extensor digitorum longus muscle for intravital investigation of the microcirculation. *Int J Microcirc Clin Exp* **10**, 335-343.
- Valera S, Hussy N, Evans RJ, Adami N, North RA, Surprenant A & Buell G. (1994). A new class of ligand-gated ion channel defined by P2x receptor for extracellular ATP. *Nature* **371**, 516-519.
- VanTeeffelen JW & Segal SS. (2006). Rapid dilation of arterioles with single contraction of hamster skeletal muscle. *Am J Physiol Heart Circ Physiol* **290**, H119-127.
- Wayland H & Johnson PC. (1967). Erythrocyte velocity measurement in microvessels by a two-slit photometric method. *J Appl Physiol* **22**, 333-337.
- Welsh DG & Segal SS. (1997). Coactivation of resistance vessels and muscle fibers with acetylcholine release from motor nerves. *Am J Physiol* **273**, H156-163.
- West GB, Brown JH & Enquist BJ. (1997). A general model for the origin of allometric scaling laws in biology. *Science* **276**, 122-126.

- Wiedeman MP, Tuma RF & Mayrovitz HN. (1981). In *An introduction to microcirculation*, pp. 157-173. Academic Press, Inc., New York.
- Williams DA & Segal SS. (1993). Feed artery role in blood flow control to rat hindlimb skeletal muscles. *J Physiol* **463**, 631-646.
- Zukowska-Grojec Z, Konarska M & McCarty R. (1988). Differential plasma catecholamine and neuropeptide Y responses to acute stress in rats. *Life Sci* **42**, 1615-1624.
- Zweifach BW. (1974). Quantitative studies of microcirculatory structure and function. I. Analysis of pressure distribution in the terminal vascular bed in cat mesentery. *Circ Res* **34**, 843-857.
- Zweifach BW & Metz DB. (1955). Selective distribution of blood through the terminal vascular bed of mesenteric structures and skeletal muscle. *Angiology* **6**, 282-290.

Chapter 2:
A simple “streak length method” for quantifying and
characterizing red blood cell velocity profiles and blood
flow in rat skeletal muscle arterioles

A form of this manuscript has been published:

Al-Khazraji BK, Novielli NM, Goldman D, Medeiros PJ & Jackson DN. (2012). A simple "streak length method" for quantifying and characterizing red blood cell velocity profiles and blood flow in rat skeletal muscle arterioles. *Microcirculation* **19**, 327-335.

2.1 Introduction

The function of skeletal muscle, which is essential for locomotion and shares many basic features with other metabolically active tissues, relies on microvascular resistance networks that are directly involved in blood flow and pressure regulation (Popel & Johnson, 2005). The unique structure of the microvascular units (i.e., a terminal arteriole and the subsequent capillaries it supplies) within skeletal muscle are arranged to maximize diffusion and exchange. Arteriolar resistance is modulated by intrinsic systems (e.g., myogenic control and endothelium derived factors) and extrinsic systems (e.g., sympathetic nerves) that tightly match blood flow (oxygen delivery) to metabolic demand. Thus, for decades, physiologists have been interested in the characteristics of skeletal muscle blood flow, with an emphasis on measuring and understanding red blood cell velocity (V_{RBC}).

Blood flow through a vessel segment is generally calculated as a product of mean red blood cell flow velocity (V_{Mean}) and vessel cross sectional area (A_{Vessel}). Centerline V_{RBC} (V_{Center}) is commonly measured using Doppler velocimetry (VanTeeffelen & Segal, 2006; Jackson *et al.*, 2010) or the dual-slit/sensor technique (Sato & Ohshima, 1988; Lee & Duling, 1989) and is converted to V_{Mean} through use of the Baker and Wayland velocity ratio conversion factor (V_{Ratio} ; an index of profile bluntness and transition layer) of 1.6 (Baker & Wayland, 1974). Use of this conversion factor, however, disregards diameter- and hematocrit-dependent changes in luminal V_{RBC} profiles and depending on the size and location of the vessel of interest tends to erroneously estimate blood flow (Pittman & Ellsworth, 1986).

At present, evaluation of microvascular V_{RBC} profiles is limited to experiments investigating arterioles and/or venules in the mesentery (Tangelder *et al.*, 1985; Tangelder *et al.*, 1986; Tangelder *et al.*, 1988; Nakano *et al.*, 2003) and omentum (Schmid-Schoenbein & Zweifach, 1975), or skeletal muscle venules (Bishop *et al.*, 2004; Das *et al.*, 2007). However, due to experimental and technical limitations, these past studies have been constrained to a small range of arteriolar diameters (approximately 17-40 μm), limiting current knowledge of V_{RBC} profiles to this range.

Arteriolar networks in many tissues have a broad range of diameters; for example, skeletal muscle arterioles range from $\sim 15 \mu\text{m}$ to $\sim 100 \mu\text{m}$. Thus, there remains a need for a feasible *in vivo* experimental model enabling concurrent measurement of V_{RBC} profiles at multiple levels within microvascular networks. Having a means to acquire V_{RBC} profiles for a broad range of arteriolar diameters would provide accurate and detailed data necessary to derive V_{Ratio} . Such data would facilitate accurate blood flow calculations for a broad range of arteriolar diameters in studies limited to centreline V_{RBC} measurements that require V_{Ratio} to calculate V_{Mean} .

In the current study we used the rat gluteus maximus (GM) muscle preparation and intravital video microscopy to meet the following objectives: 1) develop a method (“streak length method”) for V_{RBC} detection, improved characterization of *in vivo* V_{RBC} profiles and blood flow for a broad range of diameters in continuously branching arterioles and 2) obtain a best fit regression line describing the relationship between V_{Ratio} and arteriolar diameter.

2.2 Materials and methods

2.2.1 Preparations and protocols

2.2.1.1 Animal care and use

The Council on Animal Care at the University of Western Ontario approved the experimental protocol. Experiments were performed using 6 male Sprague Dawley rats (6-7 weeks old; mass: 168.5 ± 9 grams, mean \pm SD), purchased from Charles River Laboratories (Saint-Constant, Quebec, Canada) and housed on site for at least 1 week prior to study. Rats were housed in animal care facilities of the University of Western Ontario, at $\sim 24^{\circ}\text{C}$ on a 12 h–12 h light–dark cycle with access to food and water *ad libitum*. Upon completion of experimental procedures each day, the anesthetised rat was euthanized with an overdose of α -chloralose and urethane cocktail mix (intraperitoneal injection), and cervical dislocation.

2.2.1.2 Anesthesia and skeletal muscle preparation

Using intraperitoneal injection, the rat was anesthetised with a cocktail of α -chloralose (80 mg·kg⁻¹) and urethane (500 mg·kg⁻¹). A mid-neck incision was made and a tracheal cannula (PE-205) was introduced to facilitate spontaneous respiration. The right jugular vein was cannulated (PE-50 tubing) to maintain a constant infusion of anesthetic to the animal (α -chloralose: 8-16 mg·kg⁻¹·hr⁻¹, urethane: 50-100 mg·kg⁻¹·hr⁻¹) and a T-connector was used to inject fluorescent RBCs. The left carotid artery was cannulated (PE-50 tubing) to allow for recording of arterial blood pressure via the amplified signal of a pressure transducer using a PowerLab system (model ML118 PowerLab Quad Bridge Amplifier; model MLT0699 BP Transducer, AD Instruments, Colorado Springs, CO, USA). The rat was placed prone on a custom-fabricated animal platform using conducted

heat with animal temperature feedback to maintain rectal temperature at 37°C. With the animal shaved and skin prepared, under microscopic guidance the GM muscle was cut from its origin along the spine and along its rostral and caudal borders [adapted from the mouse preparation (Bearden *et al.*, 2004)]. With great care taken to preserve its neurovascular supply, the muscle flap was gently reflected away from the rat, spread evenly onto a transparent Sylgard® (Sylgard 184; Dow Corning, Midland, MI, USA) pedestal to approximate *in situ* dimensions and pinned to secure edges. The exposed tissue was superfused continuously (4-5 ml·min⁻¹) with bicarbonate-buffered physiological salt solution (PSS; 35°C at tissue, pH 7.4) of the following composition (mM): NaCl 137, KCl 4.7, MgSO₄ 1.2, CaCl₂ 2, NaHCO₃ 18 and equilibrated with 5% CO₂ / 95% N₂.

2.2.1.3 Fluorescent labelling of red blood cells

One day prior to experimentation, blood was drawn from a donor animal via cardiac puncture into a vial containing heparin. Sample was centrifuged at 1300g for 5 minutes, and the plasma layer and buffy coat were discarded. RBCs were then washed in Tris-buffered Ringer's solution (room temperature, pH = 7.4), and incubated in a freshly prepared FITC (fluorescein isothiocyanate, [0.4 mg·ml⁻¹], Cat# 4014f, Research Organics Inc., Cleveland, OH, USA) dye solution (FITC mixed into dimethyl sulfoxide and Tris-buffered Ringer's albumin (biotechnology grade bovine albumin, [0.005 g·ml⁻¹], Bioshop® Canada Inc.) solution, room temperature, pH = 7.4) for 2 hours. Cells were washed in Tris-buffered Ringer's albumin solution and stored overnight at 4°C. On day of experiment, excess dye was removed by washing cells in Tris-buffered Ringer's albumin solution, and hematocrit (Hct) was adjusted to ~30-35% with buffer. Prior to injection,

fluorescent RBCs were imaged on a microscope and qualitatively evaluated for fluorescence signal and cellular integrity. Prior to intravital video microscopy (IVVM), cells were injected (1% of total animal blood volume, blood volume estimated to be 6 ml·(100 g)⁻¹ rat) into the animal via the jugular vein (PE-50 tubing for cannula) and the line was flushed with heparinized saline. To confirm labelled cell fraction, post-experiment systemic blood samples were acquired and analysed using flow cytometry. In a separate set of experiments, the hang test (i.e., RBCs are free to fall on their edge in an oil suspension where their geometry can be observed) was conducted to derive sphericity factors, an indicator of RBC deformability (Canham & Burton, 1968), for both fluorescent and unstained RBCs. There was no significant difference in sphericity index between groups. Additionally, it has been previously shown that FITC labelled fresh blood (1 day or less) did not exhibit adherent or undeformable characteristics in the circulation (Chin-Yee *et al.*, 2009). In our experiments, no plugging of capillaries with FITC labelled cells was observed in the muscle preparation.

2.2.2 Intravital video microscopy

Upon completion of microsurgical procedures, the preparation was transferred to the stage of the intravital microscope (Olympus BX51). The preparation was equilibrated for ~30 minutes, during which time the arteriolar network was observed and a diagram was made to identify sites for data collection (vasomotion was not observed). Microvessels were observed under Kohler illumination using a long working distance condenser (NA = 0.80) and a long working distance water immersion objective (Olympus LUMPLFL: 10× NA = 0.30; depth of field ~9µm) with illumination from a 100-Watt halogen light source. To enhance contrast of the RBC column, a 450 nm/20 nm band-pass filter (450BP20,

Omega Optical, Brattleboro, VT, USA) was placed in the light path. In an effort to assess microvascular V_{RBC} , fluorescent RBCs were epi-illuminated using a 120-Watt Mercury Vapor Short Arc light source (EXFO, X-Cite 120PC Q) in line with a FITC (450-490 nm) filter. The optical image was coupled to a front-illuminated interline CCD camera (Qimaging EXi Blue) and viewed/stored to a hard drive using specialised imaging software (MetaMorph® 7.6). Following equilibration, baseline internal vessel lumen diameter was recorded and arterioles were tested for oxygen sensitivity by elevating superfusate O_2 from 0 to 21% (5% CO_2 , balance N_2) for 10 minutes, and recording arteriolar diameter. Equilibration with 5% CO_2 –95% N_2 was restored for the duration of experimental procedures. Video (.tiff) images were collected (15 fps) under epi-illumination for off-line analysis of V_{RBC} , and blood flow. Corresponding bright-field video (.tiff) images were collected (15 fps) under Kohler bright-field illumination for off-line analysis of RBC column (and luminal) diameters.

2.2.3 RBC streaks, velocity profiles and flow calculations

Fluorescent images were collected (15 fps) at 5-20 millisecond (msec) exposure times (lower exposure times for faster flow in larger arterioles, and higher exposure times for slower flow in smaller arterioles), causing fluorescing RBCs to form streaks in images (Fig. 2.1). Arteriolar lumens were divided into “lanes” (lane width was maintained from vessel to vessel) based on the number of RBCs spanning the lumen. Multiple streak measurements (manual; ImageJ 1.43u, National Institute of Health, USA) were made across the vessel lumen within each lane, and average V_{RBC} ($n = 5-12$ velocity measurements in each lane) for each lane were plotted to create V_{RBC} distribution profiles for each vessel segment (Fig. 2.2, Panel A).

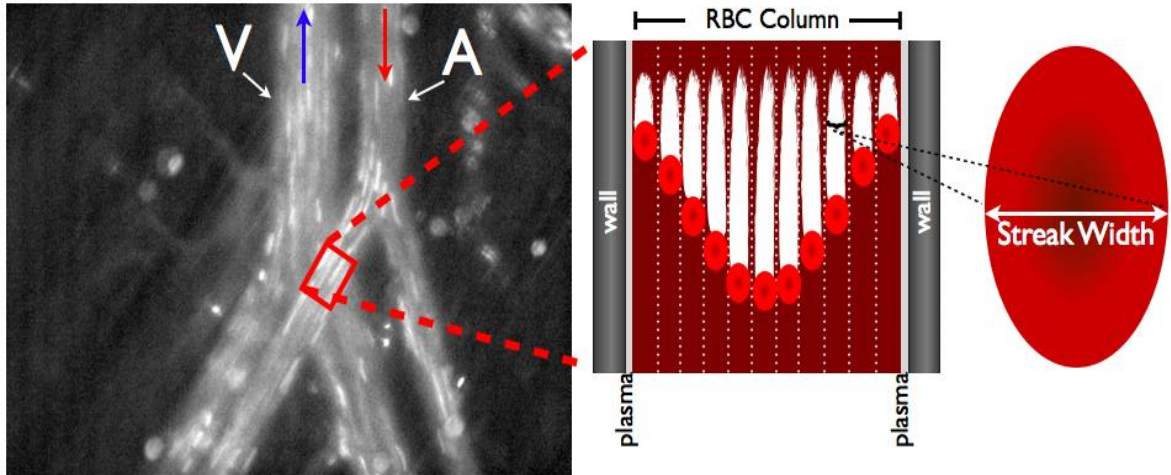


Figure 2.1: Schematic of streak length method technique.

Epi-fluorescent image of an arteriolar (A) and a venular (V) bifurcation in the rat gluteus maximus muscle (red and blue ↓: direction of flow); exposure time: 10 msec; 15 fps at 10×. Arteriolar lumen was divided into “lanes” based on number of RBCs spanning the RBC column, with RBC width represented by streak width.

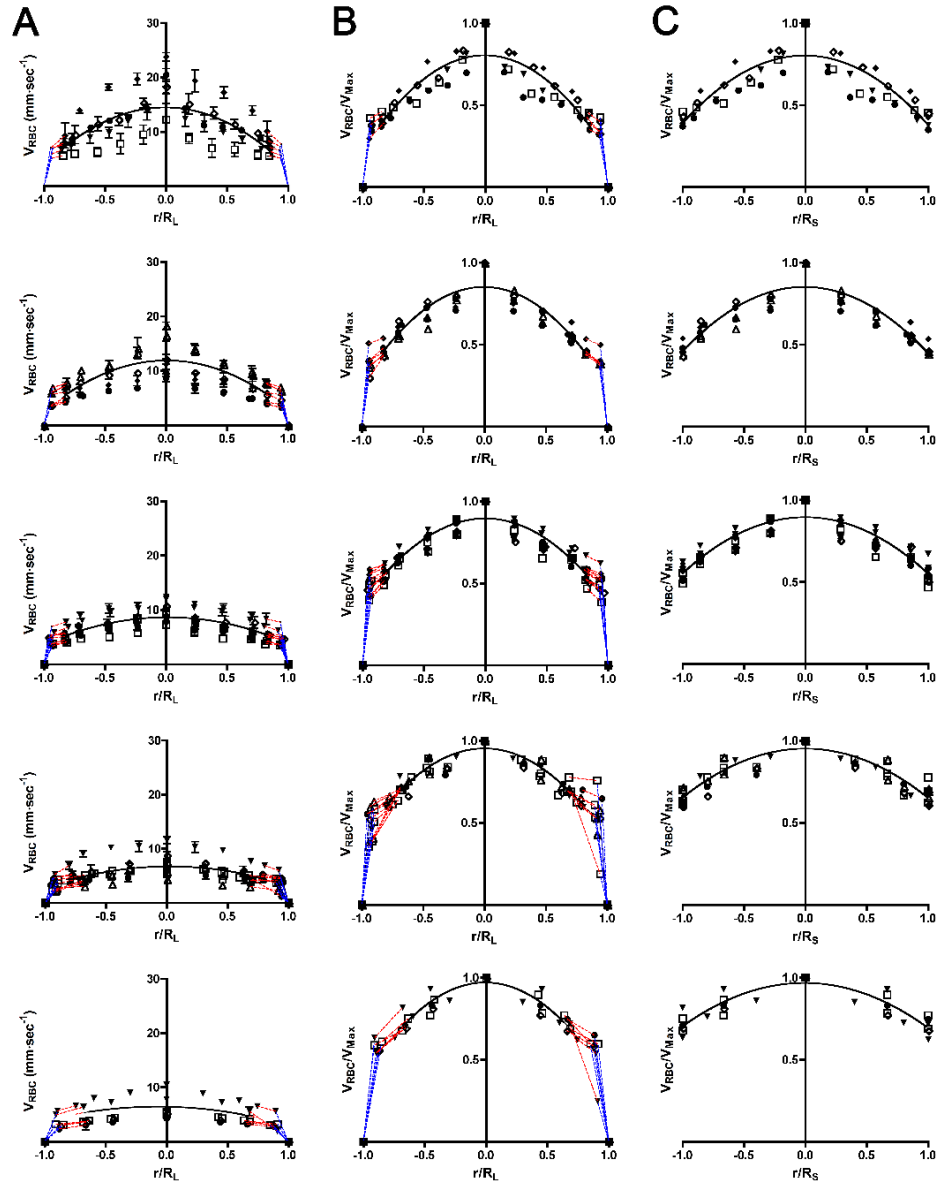


Figure 2.2: Velocity profiles from binned diameters of arteriolar segments.

Top to bottom binned diameter ranges: 83+ μm , 66-82 μm , 50-65 μm , 36-49 μm , 20-35 μm . Red dashed lines indicate extrapolated data from R_S to R_C . Blue dashed lines indicate extrapolated data from R_C to vessel wall (R_L). Panel A column: Absolute V_{RBC} distributions across normalized arteriolar lumens ($-R_L$ to R_L , including transition layer). Panel B column: Data normalized to V_{Max} across normalized RBC column ($-R_L$ to R_L , including transition layer). Panel C column: Data normalized to V_{Max} with across normalized RBC column ($-R_S$ to R_S). Data represent mean \pm SD of repeated V_{RBC} measurements ($n=5-12$ streaks) at each radial (“lane”) placement in lumen.

Velocity measurements were taken from fluorescent streaks that satisfied the following inclusion criteria:

- 1) Streaks must begin and end within the field of view of a single frame.
- 2) To ensure velocity measures were from the equatorial plane of the vessel at any given radial position (or “lane”): i) prior to epi-illumination, the equatorial plane (center) of the vessel was in the plane of focus under bright-field illumination, and ii) only streaks with the longest and lowest level of pixel intensity were measured. This excluded streaks that may have been travelling closer to the vessel wall, but still in the center lane (as indicated by short, bright streaks).
- 3) To ensure data were not collected from overlapping fluorescent red cells travelling behind one another, only streaks with similar light intensity across the length of the streak were included.

Single V_{RBC} values were calculated by using Equation 2.1.

Equation 2.1

$$V_{RBC} = \frac{\mathbf{RBC\ Streak\ Length} - \mathbf{RBC\ Length}}{\mathbf{Exposure\ Time}}$$

With the assumption that the biconcave characteristic of the RBC was preserved [RBC thickness was approximated as constant (Canham *et al.*, 1984)] during flow through any arteriole, the RBC was modelled as an elliptical cross section (AlMomani *et al.*, 2008). RBC width was set to the width of each individual streak and RBC length was calculated using Equation 2.2, where A_{RBC} (calculated from average rat red blood cell diameter of $7.18\ \mu\text{m}$, i.e., $A_{RBC} = \pi r^2$) is the coronal cross sectional area of the RBC.

$$A_{RBC} = \pi \left(\frac{RBC\ Width}{2} \right) \left(\frac{RBC\ Length}{2} \right)$$

Equation 2.2

$$RBC\ Length = \frac{4A_{RBC}}{\pi(RBC\ Width)}$$

At the outermost edge of the RBC column (R_C), velocity was extrapolated from the middle of the outermost streak (R_S , centroid of the outermost RBC) to the edge R_C (for both left and right sides of the profile; Equation 2.3. Indicated in red dashed lines on Fig. 2.2, Panels A and B). Using experimentally acquired velocity distribution profile plots, velocity curves (Equation 2.3) were fit to both left and right side of each profile to determine the power “a”, which is also an indicator of profile bluntness within the RBC column.

Equation 2.3

$$V(r) = V_{Center} - (V_{Center} - V_{R_S}) \left(\frac{r}{R_S} \right)^a, \quad 0 < r < R_C$$

Using Matlab[®] (R2010a, The Mathworks[™], Inc.), the sum of integration (trapezoidal approximation) for each profile was performed to calculate flow (\dot{Q}_{RBC}) over the RBC column (Equation 2.4). Plasma flow through the cell-free layer (\dot{Q}_{CFL}) was calculated by integrating over an assumed linear velocity gradient (between R_C and R_{Wall}) which also satisfied the no-slip condition at vessel wall ($V(R_{Wall}) = 0$) and is indicated by blue dashed lines in Fig. 2.2, Panels A and B. Total blood flow through vessel cross section was taken as a sum of \dot{Q}_{RBC} and \dot{Q}_{CFL} .

Equation 2.4

$$\begin{aligned}
 \dot{Q} &= 2\pi \int_0^{R_{Wall}} V(r)rdr = 2\pi \int_0^{R_C} V(r)rdr + 2\pi \int_{R_C}^{R_{Wall}} V(r)rdr \\
 &= 2\pi \sum_{r_i=0}^{r_i=R_C} V(r_i)r_i\Delta r + 2\pi \int_{R_C}^{R_{Wall}} V(R_C) \frac{(R_{Wall} - r)}{(R_{Wall} - R_C)} rdr \\
 &= \dot{Q}_{RBC} + \dot{Q}_{CFL}
 \end{aligned}$$

To calculate V_{Mean} , calculated blood flow values were divided by vessel cross sectional area (A_{Vessel}), and corresponding velocity ratios (V_{Ratio}) were calculated by dividing V_{Max} by V_{Mean} .

$$A_{Vessel} = \pi(R_{Wall})^2$$

$$V_{Mean} = \frac{\dot{Q}}{A_{Vessel}}$$

$$V_{Ratio} = \frac{V_{Max}}{V_{Mean}}$$

2.2.3.1 Streak length method validation

To test the reliability of flow calculations acquired through streak length method, mass balance error calculations were performed at bifurcations where theoretically:

$$\dot{Q}_{Parent} = \dot{Q}_{Daughter1} + \dot{Q}_{Daughter2}$$

$$\text{Mass Balance Error} = \frac{|(\dot{Q}_{Daughter1} + \dot{Q}_{Daughter2}) - \dot{Q}_{Parent}|}{\dot{Q}_{Parent}} \times 100\%$$

2.2.4 Statistical analyses and data presentation

Systemic measures are presented as mean \pm SD, unless otherwise stated. Data were analyzed using Prism[®] software (version 4.0a, GraphPad Software Inc., La Jolla, CA, USA) and differences were accepted as significantly different at $P < 0.05$. In an effort to discriminate the degree of bluntness in V_{RBC} profiles (specifically for Fig. 2.2), it was necessary to discretely bin arterioles into specific ranges of diameters. V_{RBC} profiles within each binned diameter range of arterioles were fit to a 2nd order polynomial ($Y = C_2x^2 + C_1x + C_0$), and an F-test was performed for all parameters of the polynomial to test whether profiles of a given bin were significantly different from one another (performed on profiles from Fig. 2.2, Panel C). Linear regression was performed to evaluate the correlation between V_{Ratio} and arteriolar diameter for each animal (Fig. 2.4). To test bilateral (left and right) symmetry of individual velocity profiles, left and right “a” values (see Equation 2.3) were compared using a paired t-test ($n = 37$ vessels). Linear regression was performed to evaluate the correlation between calculated blood flow and arteriolar diameter for experimental flow calculations (Fig. 2.3). An experimental power law relationship of blood flow as a function of diameter was derived from a linear equation (not shown) fit to a log-log plot.

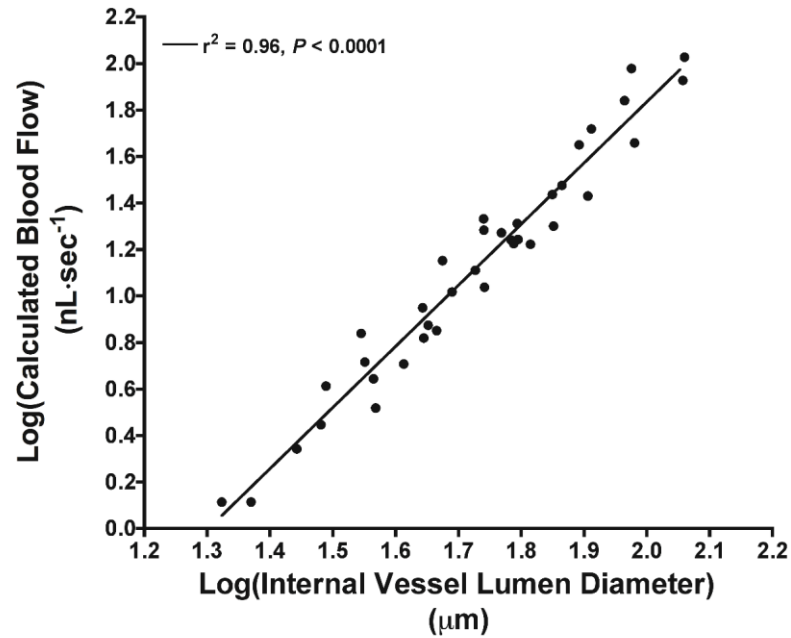


Figure 2.3: Relationship between experimental blood flow and arteriolar diameter.

Log-log plot of pooled experimental blood flow (nL·sec⁻¹; calculated from profiles) versus diameter (μm) for 37 vessel segments (n = 6 animals); slope of linear regression line = 2.63; $r^2 = 0.96$, $P < 0.0001$.

2.3 Results

2.3.1 Systemic measures and arteriolar responses to O₂

Animals were normotensive (mean arterial pressure = 94 ± 8 mmHg), and had normal systemic Hct levels ($42 \pm 4\%$) within and across experiments. In all experiments, arterioles were viable as tested by their reactivity to elevated (21%) O₂, which resulted in a 9 ± 2 μm diameter decrease in vessels ranging from 21 to 76 μm in diameter.

2.3.2 Streak length method validation

There was $0.6 \pm 3.2\%$ error (mean \pm SEM., $n = 5$ bifurcations) in mass balances calculated at bifurcations. Post-experiment flow cytometry on systemic blood samples confirmed total percentage of labelled cells did not exceed 1%, with total number of counted cells ($>200,000$ RBCs) providing less than 5% coefficient of variation in determining exact percentage of labelled cells (Sarelius & McKinlay, 1985). Additionally, post-experiment blood samples imaged on a hemocytometer confirmed maintenance of fluorescence signal and cellular integrity of labelled cells.

2.3.3 *In vivo* velocity profiles, experimental blood flow calculations, and velocity ratios

A total of 37 profiles were generated from continuous branching arteriolar trees ($n = 5-10$ arterioles per network; diameter range: 21-115 μm ; $n = 6$ animals). There were no significant differences between left and right curve fit values of “a”, indicating symmetry across all 37 profiles (with significant effective pairing of left and right values, $P < 0.0001$). Profiles within a bin were plotted ($n = 37$ individual vessels; Fig. 2.2, Panel A), and illustrated congruency in V_{RBC} profile shape (in the experimentally measured portion of RBC column; -Rs to Rs) among arterioles within the binned diameter range (fit to a 2nd

order polynomial; Fig. 2.2, Panel C). Velocity profiles became progressively more blunt with decreasing diameter with the quadratic coefficient (C_2 from the 2nd order polynomial fit) becoming less negative moving from largest (83+ μm) to smaller (20-35 μm) diameters ($C_2 = -0.42$ to -0.27 , respectively; Fig. 2.2, Panel C).

Experimental blood flow values ranged from $1.3 \text{ nL}\cdot\text{sec}^{-1}$ to $106 \text{ nL}\cdot\text{sec}^{-1}$ (diameters: 21-115 μm , respectively), and were correlated with diameter in the log-log plot (Fig. 2.3; $r^2 = 0.96$, $P < 0.0001$). Experimental blood flow data, as a function of arteriolar diameter (in μm), are described by the power equation: $\text{Blood Flow} = 10^{-3.43} \times \text{Diameter}^{2.63}$.

There was a positive linear correlation between V_{Ratio} and arteriolar diameter. From this, the least-squares linear regression of V_{Ratio} on arteriolar diameter (D ; in μm) yielded

Equation 2.5

$$V_{\text{Ratio}} = 0.0071 \times (D) + 1.15$$

with an r^2 of 0.90 (Fig. 2.4, $P < 0.0001$). V_{Ratio} values ranged from 1.35 to 1.98 (obtained from diameters ranging from 21-115 μm), indicating that profiles across the rat gluteal arteriolar network exhibit a wide range of bluntness, and become approximately parabolic ($V_{\text{Ratio}} = 2$) at diameters $\geq 115 \mu\text{m}$.

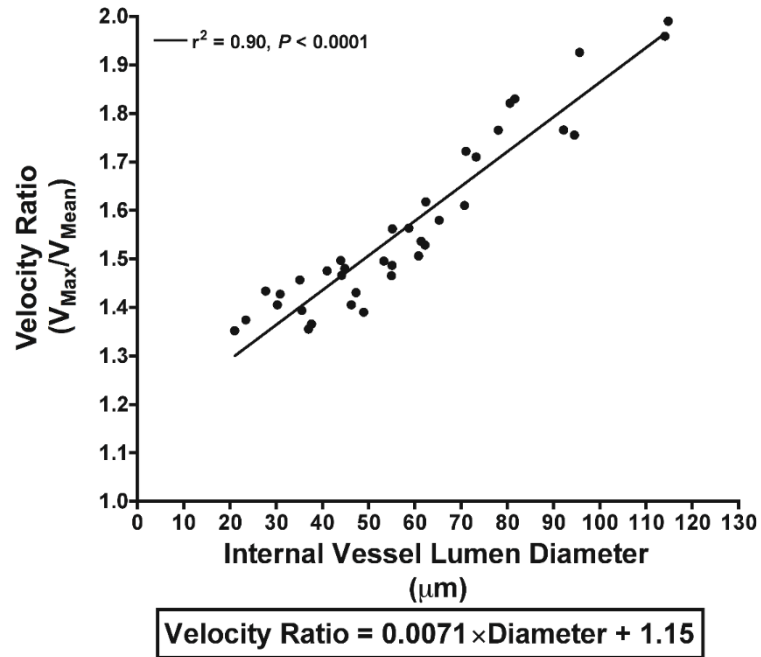


Figure 2.4: Relationship between velocity ratio and arteriolar diameter.

Velocity ratios for arterioles with diameters ranging from 21 to 115 μm (5-10 arterioles per animal; $n = 6$ animals). Within all animals, there was a positive correlation between diameter and V_{Ratio} ($r^2 = 0.90$; $P < 0.0001$). For all data, the velocity ratio, as a function of arteriolar diameter (in μm), is described by the experimentally-derived equation shown below the graph.

2.4 Discussion

In the current study we successfully developed and validated a novel *in vivo* method for characterizing V_{RBC} profiles, V_{Ratio} , and blood flow in arterioles with a broad range of diameters from microvascular networks in rat skeletal muscle. Furthermore, we derived a linear relationship between V_{Ratio} and arteriolar diameters (from 21-115 μm). From this relationship we have derived an equation that may be used in other studies to calculate blood flow based on the arteriolar diameter of interest.

2.4.1 Measuring V_{RBC} in skeletal muscle arterioles

In the present study, *in vivo* velocity profiles across continuously branching skeletal muscle arterioles were determined using fluorescent-labelled RBCs and a novel video method for determining V_{RBC} . Previously described microscopic video methods for single V_{RBC} detection use video playback on conventional video systems and analyses that require single RBC tracking from frame to frame. As discussed by Parthasarathi *et al.* these conventional video methods, that generally use cameras with frame rates of 25-30 Hz, are capable of resolving V_{RBC} of only 2 $\text{mm}\cdot\text{sec}^{-1}$ or less (Parthasarathi *et al.*, 1999).

In an effort to overcome this limitation and resolve single particle velocities, specialized methods capable of resolving high V_{RBC} ($\sim 15\text{-}40 \text{ mm}\cdot\text{sec}^{-1}$) have been presented; however, they require specialized strobe illumination (Tangelder *et al.*, 1986), asynchronous flash illumination (Pries *et al.*, 1994), or high speed synchronized shuttering (Parthasarathi *et al.*, 1999). More recently, Nakano *et al.* described a technique called particle image velocimetry (PIV), which uses an intravital microscope and transillumination coupled to an ultra-high speed digital camera (1000 fps) (Nakano *et al.*,

2003). Although this method is capable of high-resolution instantaneous V_{RBC} detection, it is limited to velocities of $6 \text{ mm}\cdot\text{sec}^{-1}$. Furthermore, due to the necessary use of high magnification objectives all of these past methods are limited due to a shallow depth of focus and thus have an upper limit on the arteriolar diameter ($< 50 \text{ }\mu\text{m}$) that can be studied.

For the first time, we have measured V_{RBC} in continuously branching arterioles in a broad range of diameters from single frame captures using conventional IVVM. With our streak length method, we investigated arterioles with diameters ranging from 21 to 115 μm and were able to measure V_{RBC} greater than $20 \text{ mm}\cdot\text{sec}^{-1}$ with a maximum detectable V_{RBC} of approximately $100 \text{ mm}\cdot\text{sec}^{-1}$. Using our streak length method V_{RBC} is measured based on the exposure time of a single frame, thus eliminating the need for specialised illumination or high camera frame rates. It is important to note that our method is limited by the sensitivity of the camera to resolve streaks under low exposure times.

In contrast to other methods, we can effectively resolve V_{RBC} using a low power ($10\times$) objective. Thus, data can be collected from larger fields of view (facilitating simultaneous V_{RBC} measurements at bifurcations) with greater depth of focus (necessary for data collection from the equatorial plane in large arterioles). Based on the above, it is implicit that our streak length method is capable of measuring V_{RBC} in all vessels (independent of diameter), so long as they can be brought into the focal plane. Finally, capturing V_{RBC} within single frames enables measurement of rapid changes in V_{RBC} , which may be useful for future microvascular studies involving muscle stimulation and/or the administration of vasoactive drugs, where blood flow changes occur rapidly.

2.4.2 Arteriolar RBC velocity profiles

This is the first study to evaluate velocity ratios from *in vivo* V_{RBC} profiles in skeletal muscle for continuously branching arterioles encompassing a large range of diameters (21-115 μm). Arterioles within this range represent the major resistance pathways responsible for the redistribution of blood flow within tissues (Zweifach *et al.*, 1981). Arteriolar velocity profiles demonstrated bilateral symmetry at all levels of the network and, as expected, velocity profiles became blunter in descending diameters of arterioles; where larger arterioles exhibited a more parabolic profile, and as diameter decreased there was a trend towards plug flow (V_{Mean} and V_{Max} are equal). In support, velocity ratios positively correlated with arteriolar diameter (Fig. 2.4). In accordance with work in rabbit mesenteric networks (Tangelder *et al.*, 1986), profiles in a given arteriolar diameter range were similar regardless of differing centerline velocities, as indicated by normalized velocity distributions (Fig. 2.2, Panels B and C).

Baker & Wayland first proposed a V_{Ratio} of 1.6 for arterioles (Baker & Wayland, 1974), which represents a correction made for the instrumental artefacts due to vertical averaging of velocity profiles. This correction factor is commonly used for blood flow calculations and has been confirmed by other studies (Seki & Lipowsky, 1989; Koutsiaris, 2009). Our V_{Ratio} values describe the true shape of the velocity profiles that were acquired from the equatorial plane of the vessels. Thus, we propose that using the generalized V_{Ratio} of 1.6 underestimates or overestimates flow calculations by up to 20% in arterioles smaller or larger than $\sim 65 \mu\text{m}$ respectively (Fig. 2.4). Even when accounting for a maximum systematic error of 3.8% (calculated from mass balance at bifurcations), there remains over 16.2% of unresolved error using a V_{Ratio} of 1.6.

In an effort to account for diameter-dependent differences in V_{Ratio} and reduce errors in blood flow calculations, we propose a linear equation derived from the relationship between velocity ratio and arteriolar diameter (21-115 μm) as measured *in vivo* (Fig. 2.4). Tangelder *et al.* derived a linear equation describing this relationship for rabbit mesentery arterioles; however, due to experimental constraints, their equation is limited to diameters in the range of 17 to 32 μm (Tangelder *et al.*, 1986). The rat GM preparation represents true locomotive striated skeletal muscle and offers several advantages for investigating hemodynamics.

First, arteriolar networks are anatomically arranged such that concurrent evaluation of multiple arteriolar levels (from 1st order to terminal arterioles) is conveniently achieved within the same focal plane. Second, the vascular anatomy is maintained across animals, as has been shown in mice (Bearden *et al.*, 2004) and confirmed in the rat (qualitative observations), enabling investigation of the same sets of vessels from experiment to experiment. We have outlined the advantages of our streak length method above (see: *Measuring V_{RBC} in skeletal muscle arterioles*), which facilitate the calculation of blood flow from the large range of arteriolar diameters that can be observed using the GM preparation.

2.4.3 Relationship between blood flow and arteriolar diameter

In the current study we derived the following equation to describe the relationship between experimentally derived blood flow and arteriolar diameter: $\text{Blood Flow} = 10^{-3.43} \times \text{Diameter}^{2.63}$, where the exponent associated with diameter (2.63) describes the slope of the log-log linear relationship. The slope of 2.63 is in close agreement with blood flow

data taken from rat cremaster muscle where power law regression yielded an exponent of 2.73 (House & Lipowsky, 1987). Additionally, the power law exponent of 2.63 is in agreement with Murray's law (Murray, 1926) and other similar studies where experimentally-derived exponents from power laws ranged from approximately 2 in larger arteries (Zamir *et al.*, 1992) to 3 in arterioles (Mayrovitz & Roy, 1983).

In conclusion, using the rat GM model we have developed a new method for V_{RBC} detection in skeletal muscle arterioles that is compatible with conventional microscopes and video systems. Our streak length method eliminates the need for frame-to-frame cell tracking that requires specialized illumination, video shuttering, or high-speed cameras. By simply altering exposure time, our method is capable of resolving a large range of V_{RBC} up to $\sim 100 \text{ mm}\cdot\text{sec}^{-1}$. From the data generated herein, we have provided a linear equation for calculating velocity ratios for arterioles (in skeletal muscle and other tissues) ranging from 21 to 115 μm in diameter.

2.5 Conclusion

We have described a relatively simple means for acquiring V_{RBC} from a broad range of arteriolar diameters (from 21-115 μm). Furthermore, a linear relationship was derived between V_{Ratio} and arteriolar diameter. From which, we present an equation that may be used in future studies to more accurately calculate blood flow based on the arteriolar diameter. This work provides significant insight to the field of blood flow and single RBC dynamics in complete microvascular networks.

2.6 References

- AlMomani T, Udaykumar HS, Marshall JS & Chandran KB. (2008). Micro-scale dynamic simulation of erythrocyte-platelet interaction in blood flow. *Ann Biomed Eng* **36**, 905-920.
- Baker M & Wayland H. (1974). On-line volume flow rate and velocity profile measurement for blood in microvessels. *Microvasc Res* **7**, 131-143.
- Bearden SE, Payne GW, Chisty A & Segal SS. (2004). Arteriolar network architecture and vasomotor function with ageing in mouse gluteus maximus muscle. *J Physiol* **561**, 535-545.
- Bishop JJ, Nance PR, Popel AS, Intaglietta M & Johnson PC. (2004). Relationship between erythrocyte aggregate size and flow rate in skeletal muscle venules. *Am J Physiol Heart Circ Physiol* **286**, H113-120.
- Canham PB & Burton AC. (1968). Distribution of size and shape in populations of normal human red cells. *Circ Res* **22**, 405-422.
- Canham PB, Potter RF & Woo D. (1984). Geometric accommodation between the dimensions of erythrocytes and the calibre of heart and muscle capillaries in the rat. *J Physiol* **347**, 697-712.
- Chin-Yee IH, Gray-Statchuk L, Milkovich S & Ellis CG. (2009). Transfusion of stored red blood cells adhere in the rat microvasculature. *Transfusion* **49**, 2304-2310.
- Das B, Bishop JJ, Kim S, Meiselman HJ, Johnson PC & Popel AS. (2007). Red blood cell velocity profiles in skeletal muscle venules at low flow rates are described by the Casson model. *Clin Hemorheol Microcirc* **36**, 217-233.
- House SD & Lipowsky HH. (1987). Microvascular hematocrit and red cell flux in rat cremaster muscle. *Am J Physiol* **252**, H211-222.
- Jackson DN, Moore AW & Segal SS. (2010). Blunting of rapid onset vasodilatation and blood flow restriction in arterioles of exercising skeletal muscle with ageing in male mice. *J Physiol* **588**, 2269-2282.
- Koutsiaris AG. (2009). A velocity profile equation for blood flow in small arterioles and venules of small mammals in vivo and an evaluation based on literature data. *Clin Hemorheol Microcirc* **43**, 321-334.
- Lee JS & Duling BR. (1989). Role of flow dispersion in the computation of microvascular flows by the dual-slit method. *Microvasc Res* **37**, 280-288.
- Mayrovitz HN & Roy J. (1983). Microvascular blood flow: evidence indicating a cubic dependence on arteriolar diameter. *Am J Physiol* **245**, H1031-1038.

- Murray CD. (1926). The Physiological Principle of Minimum Work: I. The Vascular System and the Cost of Blood Volume. *Proc Natl Acad Sci U S A* **12**, 207-214.
- Nakano A, Sugii Y, Minamiyama M & Niimi H. (2003). Measurement of red cell velocity in microvessels using particle image velocimetry (PIV). *Clin Hemorheol Microcirc* **29**, 445-455.
- Parthasarathi AA, Japee SA & Pittman RN. (1999). Determination of red blood cell velocity by video shuttering and image analysis. *Ann Biomed Eng* **27**, 313-325.
- Pittman RN & Ellsworth ML. (1986). Estimation of red cell flow microvessels: consequences of the Baker-Wayland spatial averaging model. *Microvasc Res* **32**, 371-388.
- Popel AS & Johnson PC. (2005). Microcirculation and Hemorheology. *Annu Rev Fluid Mech* **37**, 43-69.
- Pries AR, Secomb TW, Gessner T, Sperandio MB, Gross JF & Gaehtgens P. (1994). Resistance to blood flow in microvessels in vivo. *Circ Res* **75**, 904-915.
- Sarelius IH & McKinlay SM. (1985). Statistical constraints on microvascular measurements using fluorescent erythrocytes. *Am J Physiol* **248**, H577-586.
- Sato M & Ohshima N. (1988). Velocity profiles of blood flow in microvessels measured by ten channels' dual-sensor method. *Biorheology* **25**, 279-288.
- Schmid-Schoenbein GW & Zweifach BW. (1975). RBC velocity profiles in arterioles and venules of the rabbit omentum. *Microvasc Res* **10**, 153-164.
- Seki J & Lipowsky HH. (1989). In vivo and in vitro measurements of red cell velocity under epifluorescence microscopy. *Microvasc Res* **38**, 110-124.
- Tangelder GJ, Slaaf DW, Arts T & Reneman RS. (1988). Wall shear rate in arterioles in vivo: least estimates from platelet velocity profiles. *Am J Physiol* **254**, H1059-1064.
- Tangelder GJ, Slaaf DW, Muijtjens AM, Arts T, oude Egbrink MG & Reneman RS. (1986). Velocity profiles of blood platelets and red blood cells flowing in arterioles of the rabbit mesentery. *Circ Res* **59**, 505-514.
- Tangelder GJ, Teirlinck HC, Slaaf DW & Reneman RS. (1985). Distribution of blood platelets flowing in arterioles. *Am J Physiol* **248**, H318-323.
- VanTeeffelen JW & Segal SS. (2006). Rapid dilation of arterioles with single contraction of hamster skeletal muscle. *Am J Physiol Heart Circ Physiol* **290**, H119-127.

Zamir M, Sinclair P & Wonnacott TH. (1992). Relation between diameter and flow in major branches of the arch of the aorta. *J Biomech* **25**, 1303-1310.

Zweifach BW, Kovalcheck S, De Lano F & Chen P. (1981). Micropressure-flow relationships in a skeletal muscle of spontaneously hypertensive rats. *Hypertension* **3**, 601-614.

Chapter 3:
Taking the “stress” out of shear rate calculations: An
experimentally-derived shear rate equation for use in
skeletal muscle microvasculature

3.1 Introduction

Transmural pressure gives rise to forces exerted on the vessel wall, such as circumferential and longitudinal stress. Shear stress, a tangential force, is due to the viscous friction of RBC laminae brushing past one another, and when blood flows along the vessel wall, the friction results in wall shear stress. Shear stress experienced at the endothelium, or wall shear stress, is involved in modulating vasoregulatory mechanisms such as endothelial-derived nitric oxide release (Kuchan *et al.*, 1994). Shear-mediated nitric oxide release in skeletal muscle microcirculation is involved in healthy vascular regulation (Koller & Kaley, 1991; Davies, 1995; Boegehold, 1996), and is altered in vascular dysfunction conditions associated with peripheral vascular disease, as seen in spontaneously hypertensive rats (Koller & Huang, 1995).

In the skeletal muscle microcirculation, a wall shear rate (or radial velocity gradient) exists in the plasma (i.e., cell free layer or CFL)-endothelium interface. Since shear rate is dependent on blood flow velocity profiles through vessel segments, the wall shear rate can be most accurately described by the slope of blood flow velocity profile evaluated over the width of the CFL. Experimentally, under the assumption of steady plasma flow and a linear slope in the velocity gradient in the CFL (Namgung *et al.*, 2011), the wall shear rate equation is defined as the edge velocity of the red blood cell column over the

$$\text{CFL width: } \gamma_E = \frac{V_{EDGE}}{\text{Width}_{CFL}}.$$

Obtaining the necessary data for computing experimental wall shear rate is difficult and time consuming. Thus, many groups have commonly quantified shear rate from experimentally-derived mean blood velocity and arteriolar diameter (Hester & Duling,

1988; Kurjiaka & Segal, 1995; Welsh & Segal, 1996) using the equation: $\gamma_{Wall} = \frac{8V_{Mean}}{D}$.

Mean blood velocity is calculated as: $V_{Mean} = \frac{V_{Max}}{1.6}$, where a fixed velocity profile along the microvascular network is assumed, as indicated by using a constant velocity ratio for all diameters [Baker Wayland ratio of 1.6 (Baker & Wayland, 1974)]. However, our group has shown that velocity profile in the gluteus maximus muscle microcirculation is dependent on the arteriolar diameter [Chapter 2 (Al-Khazraji *et al.*, 2012)] and, as a result, previous calculations in skeletal muscle microvascular networks may be subject to over- or under-estimation (depending on diameter) of wall shear rate and wall shear stress.

Although a few past studies have calculated shear rate values from velocity profiles, their data were limited to narrow ranges of diameters from the mesenteric microcirculation (Tangelder *et al.*, 1988) or skeletal muscle arterioles (Ortiz *et al.*, 2014), or estimated from computational simulations (Sriram *et al.*, 2014). To date, wall shear rate values from experimentally derived velocity profiles in complete, continuously branching, skeletal muscle arteriolar trees have not been calculated. Using the rat gluteus maximus preparation [GM, adapted from the mouse (Bearden *et al.*, 2004)] and our “streak length” method from Chapter 2 (Al-Khazraji *et al.*, 2012) for assessing red blood cell (RBC) velocity profiles, the current study was carried out with the following objectives:

- 1) Calculate wall shear rate from *in vivo* RBC velocity profiles in gluteus maximus arterioles for a wide range of diameters.
- 2) Provide an experimentally-derived and straightforward wall shear rate estimation function for use in skeletal muscle microvascular studies (and possibly in other tissues).

3) Compare our calculated wall shear rate values to those from conventional wall shear rate calculation methods.

3.2 Materials and methods

3.2.1 Data source

In vivo data were utilized from analysis of previous work involving the assessment of RBC velocity profiles for a total of 39 arterioles in the gluteus maximus muscle preparation from 6 Sprague Dawley rats, using fluorescently-labeled red blood cells (Al-Khazraji *et al.*, 2012). Arteriolar lumenal diameters ranged from 0.021 to 0.115 mm, and mean velocities were calculated from flow values determined by integrating *in vivo* velocity profiles using trapezoidal rule. In particular, this analysis provided values for the thickness of the red blood cell-free layer near the vessel wall and the axial flow velocity at the outer edge of the RBC column. This analysis also provided centerline RBC velocity and its relation to mean blood velocity.

3.2.2 Data analysis: Wall shear rate estimation

We first estimated experimental wall shear rate, γ_E , using experimental edge RBC velocities taken from our *in vivo* red blood cell velocity profiles and assumed a linear velocity profile across the cell free layer width, with a boundary condition of zero velocity at the wall,

Equation 3.1

$$\gamma_E = \frac{\bar{V}_{RBC\ EDGE}}{Width_{CFL}}$$

where $\bar{V}_{RBC\ EDGE}$ is a mean of the most left and right red blood cell velocity values in the velocity profile. $Width_{CFL}$ is the width of the red blood cell free layer (CFL), determined by the difference between the position of the edge red blood cell, and the internal vessel luminal wall, and averaged between both left and right sides of the profile. γ_E was then plotted as a function of diameter.

3.2.3 Data analysis: Development of an experimentally derived and straightforward wall shear rate equation

In an effort to develop an accurate equation from experimentally acquired velocity profiles for use in microcirculatory studies such that minimal experimental input is required (i.e. arteriolar diameter and centerline velocity), we first determined $Width_{CFL}$, $\bar{V}_{RBC\ EDGE}$ (average velocities of edge red blood cells) and V_{Max} (centerline red blood cell velocity) as linear functions of arteriolar diameter. As well, $Width_{CFL}$ was normalized to arteriolar radius and fitted to a power law equation to obtain a power law relationship with arteriolar inner diameter.

Velocity-diameter relationships were used to determine a conversion factor, which we denote $V_{Edge\ Factor}$, relating experimental V_{Max} to $\bar{V}_{RBC\ EDGE}$. $V_{Edge\ Factor}$ should be of benefit in experiments that acquire centerline RBC velocity, where it may be difficult to acquire edge velocities.

Equation 3.2

$$V_{Edge\ Factor} = \frac{\bar{V}_{RBC\ EDGE}(D)}{V_{Max}(D)}$$

Edge velocities, $V_{Expt\ RBC\ Edge}$, can then be estimated from experimentally acquired centerline velocities, $V_{Expt\ Max}$, using the velocity conversion factor, $V_{Edge\ Factor}$,

Equation 3.3

$$V_{Expt\ RBC\ Edge} = V_{Edge\ Factor} \times V_{Expt\ Max}$$

As well, after plotting $Width_{CFL}$ as a function of diameter, we tested whether $Width_{CFL}$ values were independent of changes in V_{Max} by plotting the slope of $Width_{CFL}(D)$ against V_{Max} . The slope of $Width_{CFL}(D)$ was determined by evaluating

Equation 3.4

$$\text{Slope of } Width_{CFL} = \frac{Width_{CFL} - b}{D}$$

Where b is equal to the intercept from the regression fit of $Width_{CFL}(D)$ plotted as a function of arteriolar diameter.

Therefore Equation 3.1 can be modified to require experimentally acquired arteriolar diameter, and *in vivo* experimental centerline velocity as input variables for estimating experimental wall shear rate, $\gamma_{Expt\ Wall}$, in microvascular studies

Equation 3.5

$$\gamma_{Expt\ Wall} = \frac{V_{Expt\ RBC\ Edge}}{Width_{CFL}(D)}$$

Finally, in order to test the experimentally-derived wall shear rate equation, we calculated wall shear rate using the derived equation and compared it to the experimentally-acquired wall shear rates.

3.2.4 Data analysis: Comparison to other wall shear rate calculation methods

In an effort to compare conventional wall shear rate calculation methods (Hester & Duling, 1988) to the wall shear rates estimated from experimentally acquired velocity profiles (Equation 3.1), we calculated wall shear rate under the assumption of a parabolic velocity profile with Poiseuille flow characteristics,

Equation 3.6

$$\gamma_{Wall} = \frac{8V_{Mean}}{D}$$

where D is arteriolar diameter, and V_{Mean} is calculated by adjusting centerline velocity using an assumed static velocity ratio (V_{Ratio}). For true parabolic flow V_{Ratio} is 2, where V_{Max} is two-fold greater than V_{Mean} . However, investigators commonly set V_{Ratio} to 1.6 as a global correction factor for velocity profile blunting [Baker Wayland ratio (Baker & Wayland, 1974)].

Equation 3.7

$$\gamma_{Wall} = \frac{8V_{Max}}{V_{Ratio} \times D}$$

However, we have recently shown that V_{Ratio} is dependent on arteriolar diameter [in μm ; (Al-Khazraji *et al.*, 2012)] where:

$$V_{Ratio}(D) = 0.0071 \times (D) + 1.15$$

Thus, using Equation 3.7, wall shear rate was calculated for three cases: 1) $V_{Ratio} = 1.6$, 2) $V_{Ratio} = 2$, and 3) $V_{Ratio}(D) = 0.0071 \times (D) + 1.15$ [for arteriolar diameters in μm (Al-Khazraji *et al.*, 2012)].

Our experimentally acquired wall shear rates, γ_E , was then compared to the wall shear rates calculated for the three cases.

3.2.5 Statistical analysis

To test for differences between the three cases for calculating wall shear rate, a linear regression statistical comparison for slope and y-intercepts was conducted. Comparisons were made using a linear regression statistical comparison for differences in slope and y-intercept values. For all linear regression fitting, the dependent variable (y) was considered to be linearly related to the independent variable (x) when the slope was significantly different from zero. Differences between the various calculation methods were accepted when P value was less than α level of significance of 0.05. All data were plotted and analyzed using Graphpad Prism (V. 4.0a, La Jolla, CA, USA).

3.3 Results

3.3.1 Wall shear rate estimation from *in vivo* velocity profiles

Experimentally acquired wall shear rates, γ_E , ranged from 1317 to 3684 sec^{-1} , for arteriolar diameters ranging from 0.021 to 0.115 mm, and there was no relationship between γ_E and arteriolar diameter (Fig. 3.1). There was a positive linear relationship between $Width_{CFI}$ and diameter (Fig. 3.2; $P < 0.05$; $r^2 = 0.64$), for arteriolar diameters ranging from 0.021 to 0.115 mm, described by

Equation 3.8

$$Width_{CFL}(D) = 0.022 \times (D) + 0.00074$$

Average cell free layer width (left and right wall luminal measurements) ranged from 0.001 to 0.0043 mm, and the mean cell free layer width for the 39 arterioles was 0.00198 \pm 0.0007 mm. There was a negative power law relationship between normalized $Width_{CFL}$ values and arteriolar diameter, highlighting the importance of the cell free layer with decreasing diameter (Fig. 3.3, $r^2=0.74$).

RBC velocities at the edge of the velocity profile, $\bar{V}_{RBC\ EDGE}$, were positively linearly correlated with arteriolar diameter (Fig. 3.4; $r^2 = 0.44$; $P < 0.05$), and are described by

Equation 3.9

$$\bar{V}_{RBC\ EDGE}(D) = 44 \times (D) + 1.99$$

Centerline RBC velocities, V_{Max} , were positively linearly correlated with arteriolar diameter (Fig. 3.5; $r^2 = 0.71$; $P < 0.05$) and are described by

Equation 3.10

$$V_{Max}(D) = 166 \times (D) + 0.39$$

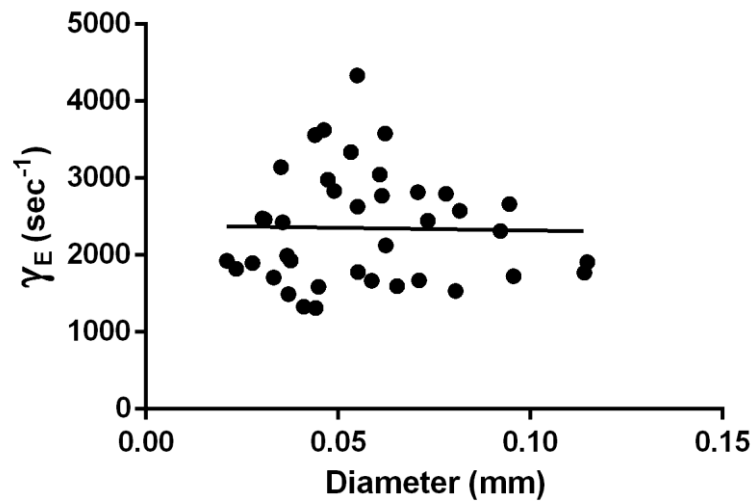


Figure 3.1: Relationship between experimentally acquired wall shear rate and arteriolar diameter.

Calculated wall shear rate values (using edge velocities) as a function of diameter.

Calculated experimental wall shear rate (γ_E) were independent of arteriolar diameter. γ_E values ranged from 1317 to 3684 sec⁻¹, for arteriolar diameters ranging from 0.021 to 0.115 mm.

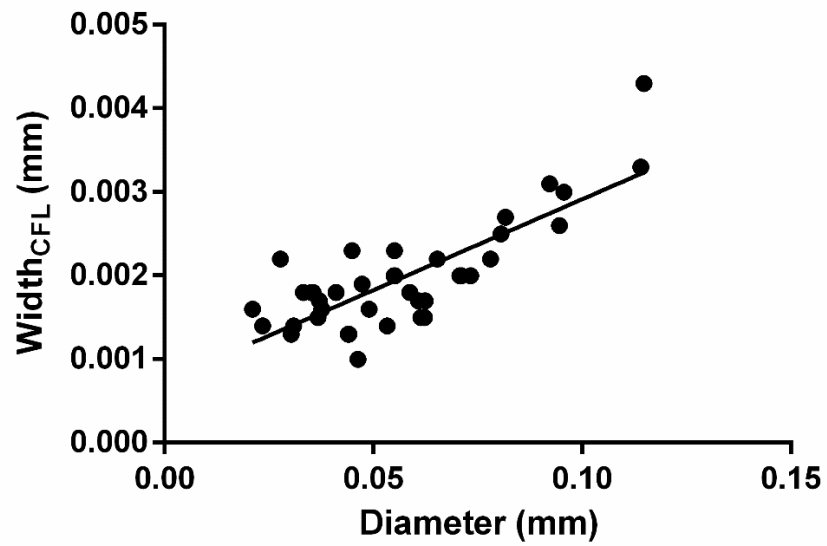


Figure 3.2: Relationship between cell free layer width and arteriolar diameter.

Arteriolar diameter ranging from 0.021 to 0.115 mm; $r^2=0.64$; and $P<0.05$, relationship described by $Width_{CFL}(D) = 0.022 \times (D) + 0.00074$.

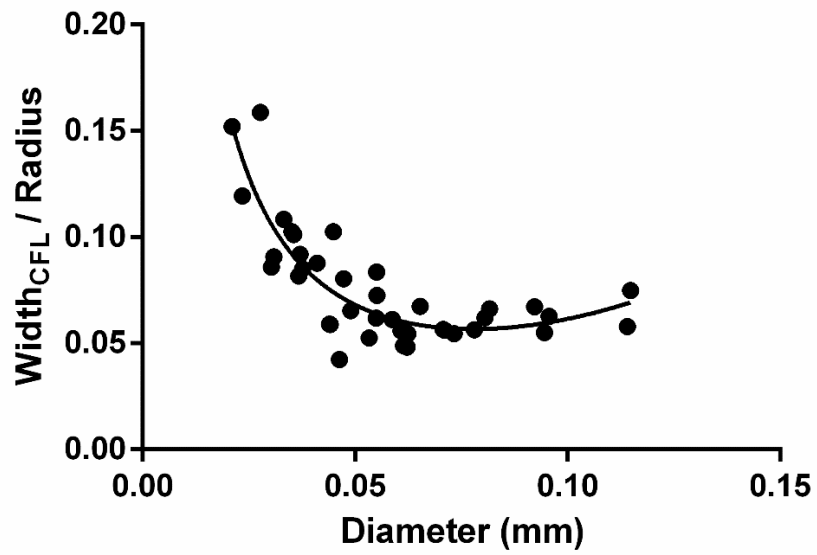


Figure 3.3: Normalized cell free layer as a function of arteriolar diameter.

Arteriolar diameter ranging from 0.021 to 0.115 mm ($r^2=0.74$), power relationship described by $Width_{CFL}/Radius = 6.3 \times (D)^{2.3} + 0.003 \times (D)^{-1.04}$

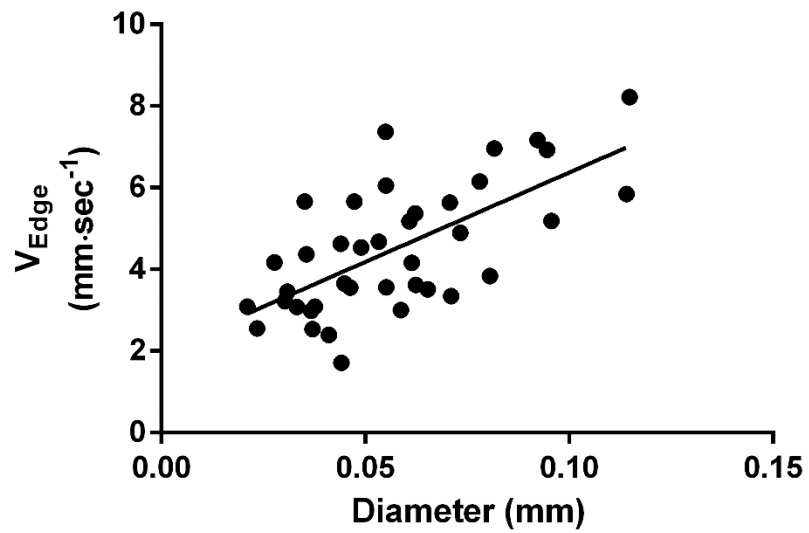


Figure 3.4: Relationship between profile edge velocity and arteriolar diameter.

Arteriolar diameter ranging from 0.021 to 0.115 mm, $r^2=0.44$; $P<0.05$, relationship described by $V_{Edge} = 44 \times (D) + 1.99$

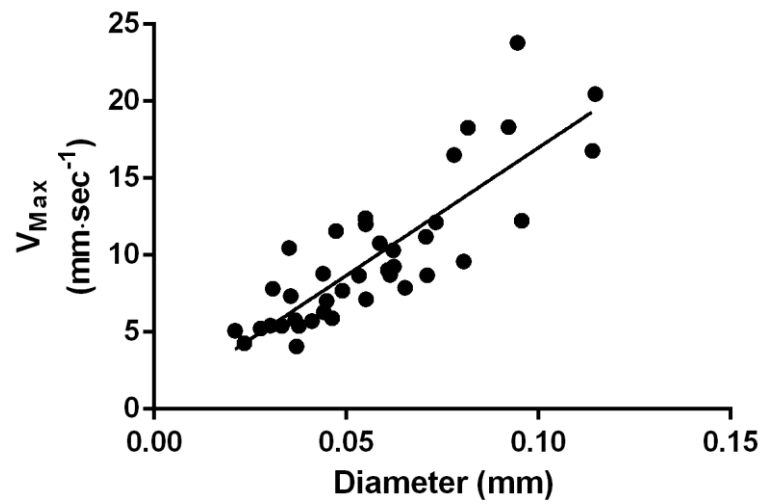


Figure 3.5: Relationship between centerline velocity and arteriolar diameter.

Arteriolar diameter ranging from 0.021 to 0.115 mm, $r^2=0.71$; $P<0.05$, relationship described by $V_{Max} = 166 \times (D) + 0.39$

3.3.2 Development of an experimentally-derived and straightforward wall shear rate equation

As both $\bar{V}_{RBC\ EDGE}$ and V_{Max} expressed a relationship with arteriolar diameter ($P < 0.05$), then the functions can be used to describe $V_{Edge\ Factor}$, the conversion factor for calculating experimental edge velocities from experimentally-acquired centerline velocities.

$$V_{Edge\ Factor} = \frac{\bar{V}_{RBC\ EDGE}(D)}{V_{Max}(D)} = \frac{44 \times (D) + 1.99}{166 \times (D) + 0.39}$$

Finally, in order to ensure that $Width_{CFL}$ independent of changes with V_{Max} , the slope of $Width_{CFL}(D)$, Equation 3.4 (using y-intercept from Equation 3.8, the regression fit of Fig. 3.2; $P < 0.05$) was plotted against V_{Max} .

From Equation 3.8, the b term is 0.00074; therefore, the slope of $Width_{CFL}$ is

Equation 3.11

$$Slope\ of\ Width_{CFL} = \frac{Width_{CFL} - 0.00074}{D}$$

Experimental $Width_{CFL}$, and D values were used as inputs to determine

$Slope\ of\ Width_{CFL}$. There was no relationship between $Slope\ of\ Width_{CFL}$ and V_{Max} (Fig. 3.6), indicating that $Width_{CFL}$ is independent of changes in V_{Max} .

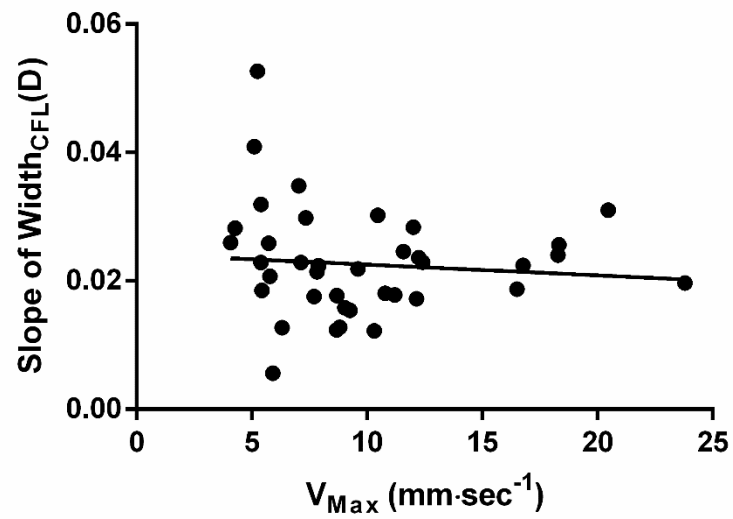


Figure 3.6: Relationship between change in cell free layer width and centerline velocity.

Plot of centerline RBC velocity, V_{Max} and $Slope\ of\ Width_{CFL}$ ($r^2=0.008$), where there was no relationship.

As CFL width exhibited a linear relationship with arteriolar diameter (Fig. 3.2; $P < 0.05$), then the linear relationship $Width_{CFL}(D) = 0.022 \times (D) + 0.00074$ can be used as an input function in Equation 3.5 for calculating experimental wall shear rate, $\gamma_{Expt Wall}$, using centerline velocities (in $mm \cdot sec^{-1}$) and arteriolar diameters (in mm) as inputs.

Recall, Equation 3.1 as a function of arteriolar diameter, D , and centerline velocity, V_{Max} , can be modified to Equation 3.5

$$\gamma_{Expt Wall} = \frac{V_{Expt RBC Edge}}{Width_{CFL}(D)}$$

As previously described, experimental centerline velocity can be converted to edge velocity using the following equation

$$V_{Expt RBC Edge} = V_{Edge Factor} \times V_{Expt Max}$$

$$V_{Edge Factor} = \frac{44 \times (D) + 1.99}{166 \times (D) + 0.39}$$

$$\gamma_{Expt Wall} = \frac{V_{Edge Factor} \times V_{Expt Max}}{0.022 \times (D) + 0.00074}$$

Equation 3.12

$$\therefore \gamma_{Expt Wall} = \frac{\left(\frac{44 \times (D) + 1.99}{166 \times (D) + 0.39} \right) \times V_{Expt Max}}{0.022 \times (D) + 0.00074}$$

Equation 3.12 can be used in microvascular skeletal muscle experiments, requiring only arteriolar diameter (in mm) and centerline velocity (in $\text{mm}\cdot\text{sec}^{-1}$), to calculate wall shear rate without the assumption of parabolic velocity profiles, and without requiring the use of a constant velocity ratio (e.g., commonly used Baker Wayland ratio of 1.6).

As previously mentioned, there was no relationship between wall shear rate calculated using Equation 3.1 and arteriolar diameter (Fig. 3.1). As well, there were no differences in slopes and y-intercept values for the regression lines of both values calculated (Fig. 3.7) using the experimentally-derived wall shear rate equation (Equation 3.12) and our experimentally-acquired wall shear rates (Equation 3.1).

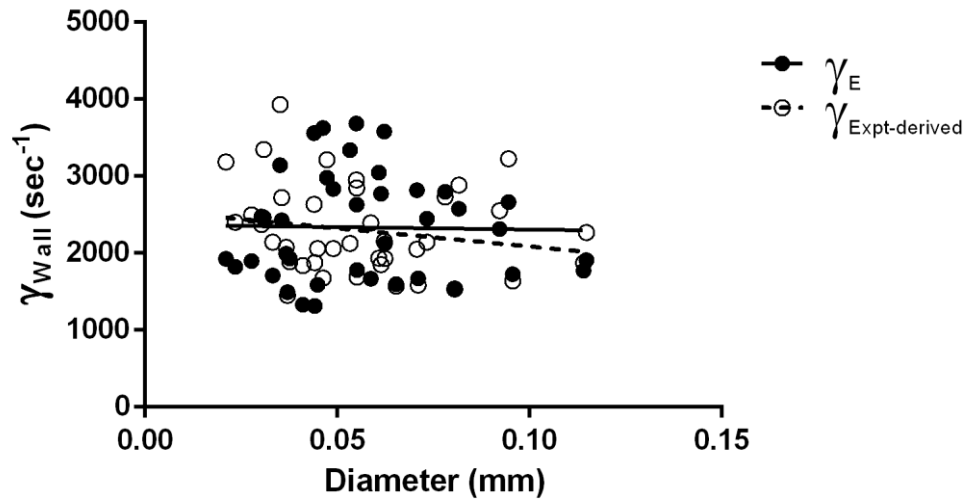


Figure 3.7: Comparison of experimental and calculated wall shear rates.

Comparison of estimated wall shear rates from experimentally-derived velocity profiles, γ_E (using Equation 3.1), versus calculated wall shear rates from the experimentally-derived equation, $\gamma_{Expt-derived}$ (using Equation 3.12). There were no differences between the slopes or y-intercepts of the two lines, and each set of wall shear rate values had no relationship with diameter. r^2 for γ_E is 0.0005; r^2 for $\gamma_{Expt-derived}$ is 0.04.

3.3.3 Comparison of wall shear rate calculation methodologies

There was no relationship between wall shear rate and arteriolar diameter (calculated using Equation 3.6) for $V_{Ratio} = 1.6$ and $V_{Ratio} = 2$ (Fig. 3.8). However, there was a relationship between wall shear rate and arteriolar diameter when $V_{Ratio}(D) = 0.0071 \times (D) + 1.15$, which is described by $\gamma_{Wall} = -5579 \times (D) + 1235$ (Fig. 3.8; $r^2 = 0.24$; $P < 0.05$). There was no significant difference between the slopes of the linear regressions for the three cases; however, there was a significant difference in y-intercept values ($P < 0.05$).

Upon comparison of each of the three cases with our experimental wall shear rates (from Equation 3.1; Fig. 3.8), experimental wall shear rate values were different from wall shear rate calculated from any one of the three cases for velocity ratio. Upon comparing values (percent change) evaluated at 0.021 mm and 0.115 mm using the fitted regression lines between wall shear rates when $V_{Ratio}(D)$ and when $V_{Ratio} = 1.6$ (Equation 3.6), there was a 20% and 25% over- and under-estimation, respectively.

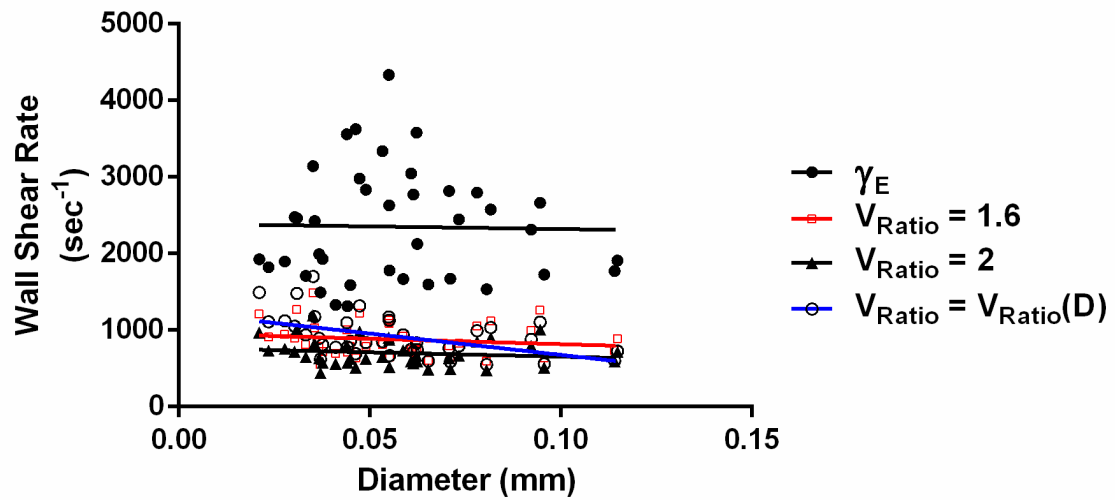


Figure 3.8: Comparison of wall shear rates (WSR) using different velocity ratios.

Wall shear rate as a function of arteriolar diameter for 1) experimental wall shear rate, γ_E , (black closed circles; no relationship with diameter), 2) $V_{Ratio} = 1.6$ (red open squares with red regression line; no relationship with diameter), 3) $V_{Ratio} = 2$ (black triangles with black regression line; no relationship with diameter), and 4) $V_{Ratio}(D) = 0.0071 \times (D) + 1.15$ (black open circles with blue regression line; positive linear relationship described by $WSR(D) = -5579 \times (D) + 1235$; $r^2 = 0.24$; $P < 0.05$). Y-intercepts are significantly different between the three linear regressions. γ_E values were greater than the other three cases with varying V_{Ratio} values ($P < 0.05$).

3.4 Discussion

The salient findings of the study herein are: 1) estimated wall shear rate calculated from experimentally-acquired velocity profiles does not have a relationship with arteriolar diameter (Fig. 3.1), 2) a straightforward wall shear rate equation has been derived from the relationship of experimental hemodynamic parameters with arteriolar diameter (Equation 3.12), and this equation yields wall shear rate calculations that are the same as our experimental values (Equation 3.1; Fig. 3.7), 3) our estimated wall shear rate (Fig. 3.1), γ_E , was significantly greater than wall shear rate values evaluated under Poiseuille parabolic flow assumption, regardless of the velocity ratio value (Fig. 3.8).

3.4.1 Wall shear rate estimation

Experimental data on the width of the microvascular cell free layer are limited; with conflicting findings showing both diameter-independent cell free layer width values as reported in cat cerebral microvessels (Yamaguchi *et al.*, 1992), as well as diameter-dependent cell free layer width values as seen in the human red blood cell perfused rabbit mesentery (Soutani *et al.*, 1995). In the study herein, using our estimated shear rate equation (Equation 3.1), we show that shear rate/stress is diameter independent (Fig. 3.1). This finding is in accordance with an extension on Murray's law (Murray, 1926), where it was shown that shear stress is independent of vessel diameter (Zamir, 1977). This process of maintaining constant shear stress would involve adjustments to diameter; that is, if blood flow changes within a vessel, the vessel diameter would respond accordingly to the increases in shear, and the shear stress is returned to normal baseline levels (Reneman *et al.*, 2006).

We provide novel evidence on the cell free layer-arteriolar diameter relationship for a wide range of arteriolar diameters (0.021 to 0.115 mm; Fig. 3.2) in an *in vivo* skeletal muscle preparation. The mean cell free layer width for the 39 arterioles was 0.00198 ± 0.0007 mm, and was in agreement with previous reported values of 0.0016 ± 0.0013 mm in the rat mesentery (Pries *et al.*, 1989), and 0.0008 to 0.0029 mm in the rat cremaster muscle (Kim *et al.*, 2007). As well, normalized CFL width values (Fig. 3.3) were in accordance with both experimental and theoretical values, as summarized by Sriram *et al.* (Sriram *et al.*, 2014).

The majority of *in vivo* data on cell free layer width and shear rate/stress have been collected from the rat cremaster muscle preparation (Kim *et al.*, 2007; Ong *et al.*, 2010; Ong *et al.*, 2011). To our knowledge, the study herein is the first to report these hemodynamic parameters from a microvascular network in true locomotive skeletal muscle.

3.4.2 Development of an experimentally derived and straightforward wall shear rate equation

We have also provided an equation which can be used to calculate wall shear rate using experimental inputs of arteriolar diameter and V_{Max} (Equation 3.12), both of which are parameters that are easily acquired from *in vivo* skeletal muscle microvascular studies.

This equation can also be used to calculate wall shear stress, as the gradient of the velocity profile is evaluated over the width of the CFL, thereby only requiring plasma viscosity for wall shear stress calculations. Using these profiles, we have provided equations describing relationships between edge and maximum velocities as functions of diameter (Figs. 3.4 and 3.5, respectively), which can be used as a conversion factor when

using experimental V_{Max} values for shear rate calculations. Additionally, experimental arteriolar diameter values can be used as inputs to calculate CFL, when it is not experimentally feasible to collect such data.

Recently, a wall shear stress correction factor has been described which corrects the conventional widely-used wall shear stress calculation which relies on Poiseuille's law, and only requires the additional input of discharge hematocrit, V_{Max} , and vessel radius (Sriram *et al.*, 2014). While this correction factor adjusts for important parameters that would certainly influence wall shear rate calculations, its utility is limited by 1) the assumption of parabolic Poiseuille flow profiles, and 2) the difficulty in acquiring *in vivo* discharge hematocrit measurements.

In the equation we propose for wall shear rate (Equation 3.12), there is no assumption of velocity profile shape as only the edge velocities were used to develop the equation, which would indirectly imply a diameter dependent velocity profile shape (Al-Khazraji *et al.*, 2012) as edge velocities are linearly correlated with arteriolar diameters (Fig. 3.4). As our wall shear rate equation depends on edge velocities and the cell free layer width, then our shear rate values can easily be converted to wall shear stress by multiplying the computed shear rate values by plasma viscosity. As plasma viscosity remains relatively constant throughout the microvasculature, as it is primarily affected by plasma protein content (Kesmarky *et al.*, 2008), our wall shear rates are a direct indication of wall shear stress for the full range of arteriolar diameters.

3.4.3 Comparison of wall shear rate calculation methodologies

We have shown in our previous study (Al-Khazraji *et al.*, 2012) that velocity ratios are diameter-dependent. Upon computing wall shear rates using our diameter-dependent velocity ratio, there was an over- and under-estimation of wall shear rate calculation compared to shear rates calculated using a fixed velocity ratio of 1.6. As well, upon comparison of our experimental wall shear rates (using Equation 3.1) against the wall shear rates computed using Poiseuille based wall shear rate equations under the three cases of velocity ratio, our experimental data were greater than all of the three cases. Despite utilizing a diameter-dependent velocity ratio in Poiseuille based wall shear rate equations, the computed wall shear rates did not adjust for computational error as data remained significantly less than our experimental wall shear rates.

Pseudoshear rate, or mean shear across a vessel lumen, is defined as: $\frac{V_{Mean}}{D}$, and is directly proportional to Poiseuille based calculations of wall shear rate (Equation 3.6). Thus, previous accounts of wall shear rate in microvascular studies that have utilized Equation 3.6 were greatly underestimating wall shear rate values and were indirectly reporting values proportional to mean shear rates, rather than the intended wall shear rates.

Shear rate is lowest (approximately zero) in the center of the vessel, and highest near the inner wall; thus, our method of computing shear rate that only involves shear rate evaluation over the thickness of the CFL provides a better estimate of wall shear rate than values that are computed over the entire lumen diameter. While data on CFL width, and RBC column edge velocities are difficult to obtain, we provide a straightforward equation

that can be adapted to other studies, and is derived from *in vivo* velocity profile data. In support, shear rate values calculated from *in vivo* velocity profiles in the rabbit mesentery were approximately 2 times higher than the values that would have been estimated under the assumption of a parabolic flow profile (Tangelder *et al.*, 1988).

It has been shown that wall shear stress is dependent on vascular diameter in the rat (Pries *et al.*, 1995a) and cat mesentery (Lipowsky *et al.*, 1978) and the rat cremaster (Koller & Kaley, 1991). Under the assumption of a fixed plasma viscosity (i.e., wall shear rate values are in direct proportion to wall shear stress), the relationship between our experimental wall shear rates and arteriolar diameter is in accordance with the above previous studies, where there is minimal dependence of shear stress values on arteriolar diameter for arterioles greater than 15 μm . Finally, Zamir concluded that while the “constant shear” arising from acceptance of Murray’s law is invalid across the entire circulatory system, it may certainly hold validity in groups of vessels (i.e., capillaries, arterioles, *etc.*), in which the major determinant regulating blood vessel radii is attributed to shear forces acting on the endothelium (Zamir, 1977). These concepts, presented 4 decades ago, now have some experimental support from our work on arteriolar diameters and calculated wall shear stress.

3.5 Conclusion

The acquisition of *in vivo* velocity profiles in fast-flowing arterioles using our fluorescently-labeled red blood cell velocity measurement technique has provided the ability to estimate wall shear rate without the assumption of fixed velocity profile shape. The optimized wall shear rate equation provided in the study herein can easily be adapted to use in several studies investigating wall shear rate. The equations provided in the study

herein are easily adaptable to use with other velocity measurement techniques in order to collect wall shear rate and (in cases where plasma viscosity is known) stress from skeletal muscle preparations for a wide range of arterioles.

3.6 References

- Al-Khazraji BK, Novielli NM, Goldman D, Medeiros PJ & Jackson DN. (2012). A simple "streak length method" for quantifying and characterizing red blood cell velocity profiles and blood flow in rat skeletal muscle arterioles. *Microcirculation* **19**, 327-335.
- Baker M & Wayland H. (1974). On-line volume flow rate and velocity profile measurement for blood in microvessels. *Microvasc Res* **7**, 131-143.
- Bearden SE, Payne GW, Chisty A & Segal SS. (2004). Arteriolar network architecture and vasomotor function with ageing in mouse gluteus maximus muscle. *J Physiol* **561**, 535-545.
- Boegehold MA. (1996). Shear-dependent release of venular nitric oxide: effect on arteriolar tone in rat striated muscle. *Am J Physiol* **271**, H387-395.
- Davies PF. (1995). Flow-mediated endothelial mechanotransduction. *Physiol Rev* **75**, 519-560.
- Hester RL & Duling BR. (1988). Red cell velocity during functional hyperemia: implications for rheology and oxygen transport. *Am J Physiol* **255**, H236-244.
- Kesmarky G, Kenyeres P, Rabai M & Toth K. (2008). Plasma viscosity: a forgotten variable. *Clin Hemorheol Microcirc* **39**, 243-246.
- Kim S, Kong RL, Popel AS, Intaglietta M & Johnson PC. (2007). Temporal and spatial variations of cell-free layer width in arterioles. *Am J Physiol Heart Circ Physiol* **293**, H1526-1535.
- Koller A & Huang A. (1995). Shear stress-induced dilation is attenuated in skeletal muscle arterioles of hypertensive rats. *Hypertension* **25**, 758-763.
- Koller A & Kaley G. (1991). Endothelial regulation of wall shear stress and blood flow in skeletal muscle microcirculation. *Am J Physiol* **260**, H862-868.
- Kuchan MJ, Jo H & Frangos JA. (1994). Role of G proteins in shear stress-mediated nitric oxide production by endothelial cells. *Am J Physiol* **267**, C753-758.

- Kurjiaka DT & Segal SS. (1995). Conducted vasodilation elevates flow in arteriole networks of hamster striated muscle. *Am J Physiol* **269**, H1723-1728.
- Lipowsky HH, Kovalcheck S & Zweifach BW. (1978). The distribution of blood rheological parameters in the microvasculature of cat mesentery. *Circ Res* **43**, 738-749.
- Murray CD. (1926). The Physiological Principle of Minimum Work: I. The Vascular System and the Cost of Blood Volume. *Proc Natl Acad Sci U S A* **12**, 207-214.
- Namgung B, Ong PK, Johnson PC & Kim S. (2011). Effect of cell-free layer variation on arteriolar wall shear stress. *Ann Biomed Eng* **39**, 359-366.
- Ong PK, Jain S, Namgung B, Woo YI & Kim S. (2011). Cell-free layer formation in small arterioles at pathological levels of erythrocyte aggregation. *Microcirculation* **18**, 541-551.
- Ong PK, Namgung B, Johnson PC & Kim S. (2010). Effect of erythrocyte aggregation and flow rate on cell-free layer formation in arterioles. *Am J Physiol Heart Circ Physiol* **298**, H1870-1878.
- Ortiz D, Briceno JC & Cabrales P. (2014). Microhemodynamic parameters quantification from intravital microscopy videos. *Physiol Meas* **35**, 351-367.
- Pries AR, Ley K, Claassen M & Gaehtgens P. (1989). Red cell distribution at microvascular bifurcations. *Microvasc Res* **38**, 81-101.
- Pries AR, Secomb TW & Gaehtgens P. (1995). Design principles of vascular beds. *Circ Res* **77**, 1017-1023.
- Reneman RS, Arts T & Hoeks AP. (2006). Wall shear stress--an important determinant of endothelial cell function and structure--in the arterial system in vivo. Discrepancies with theory. *J Vasc Res* **43**, 251-269.
- Soutani M, Suzuki Y, Tateishi N & Maeda N. (1995). Quantitative evaluation of flow dynamics of erythrocytes in microvessels: influence of erythrocyte aggregation. *Am J Physiol* **268**, H1959-1965.
- Sriram K, Intaglietta M & Tartakovsky DM. (2014). Non-Newtonian flow of blood in arterioles: consequences for wall shear stress measurements. *Microcirculation* **21**, 628-639.
- Tangelder GJ, Slaaf DW, Arts T & Reneman RS. (1988). Wall shear rate in arterioles in vivo: least estimates from platelet velocity profiles. *Am J Physiol* **254**, H1059-1064.

- Welsh DG & Segal SS. (1996). Muscle length directs sympathetic nerve activity and vasomotor tone in resistance vessels of hamster retractor. *Circ Res* **79**, 551-559.
- Yamaguchi S, Yamakawa T & Niimi H. (1992). Cell-free plasma layer in cerebral microvessels. *Biorheology* **29**, 251-260.
- Zamir M. (1977). Shear forces and blood vessel radii in the cardiovascular system. *J Gen Physiol* **69**, 449-461.

Chapter 4:
From one generation to the next: A comprehensive
account of sympathetic receptor control in branching
arteriolar trees

A form of this manuscript has been accepted for publication:

Al-Khazraji BK, Saleem A, Goldman D, Jackson DN. (2015). From one generation to the next: A comprehensive account of sympathetic receptor control in branching arteriolar trees. *J Physiol* (in press; April 2015).

4.1 Introduction

The sympathetic nervous system (SNS) promotes tonic vasoconstriction in skeletal muscle microvascular beds (Clifford & Hellsten, 2004; Segal, 2005) via neuronal release of norepinephrine (NE), neuropeptide Y (NPY), and adenosine-5'-triphosphate (ATP), which act on their respective receptors (i.e., α 1R and α 2R, Y1R, and P2X1R) located extraluminally on arteriolar vascular smooth muscle cells (Kiowski *et al.*, 1983; Ruffolo *et al.*, 1991; Malmstrom *et al.*, 1997; Burnstock, 2007). Vasoconstriction to SNS stimulation varies among arterioles due to arteriolar size and branch order (Marshall, 1982; Boegehold & Johnson, 1988; Dodd & Johnson, 1991). Arteriolar network geometry (i.e., topology) is a primary determinant of baseline network resistance (Pries *et al.*, 1995a); therefore, acute control of arteriolar diameter must coordinate with topology in order to effectively regulate microvascular blood flow and red blood cell (RBC) distribution.

Past and recent investigators of α -adrenoreceptor (i.e., α 1R and α 2R) arteriolar control of the rat cremaster (Faber, 1988; Ohyanagi *et al.*, 1991) and mouse gluteus maximus muscle (Moore *et al.*, 2010), concluded that proximal arterioles [i.e., first order (1A) to third order (3A)] are dominated by adrenergic control. This is in contrast to both NPY (Ekelund & Erlinge, 1997) and ATP (Gitterman & Evans, 2000), where peak responses have been reported to act at the distal pre-capillary terminal arterioles. However the scope of such studies is limited, as experimental past approaches enabled interrogation of partial networks (i.e., 1A to 3A arterioles at best) or discrete vessels. In an effort to reveal how the SNS regulates blood flow distribution in skeletal muscle microvasculature, the development of a preparation with access to a complete branching arteriolar trees is

necessary. To date, no studies have systematically and comprehensively defined the relationship between arteriolar order, activation of receptors for sympathetic neurotransmitters, and hemodynamics in skeletal muscle networks.

We recently developed a novel rat gluteus maximus (GM) preparation [Chapter 2, (Al-Khazraji *et al.*, 2012); adapted from the mouse (Bearden *et al.*, 2004)], which enables the investigation of sympathetic control in complete branching arteriolar trees. The aim of this study was to characterize topologically-dependent SNS modulation along arteriolar trees in the rat GM, and investigate the consequent hemodynamics. Thus, the objectives of this study were to: 1) systematically determine the arteriolar responses to specific sympathetic receptor activation as a function of branch order (i.e., from 1A to 5A), and 2) input these responses into an in-house developed computational blood flow model to estimate the functional consequence(s) of order-dependent sympathetic control on total blood flow and red blood cell distribution within the arteriolar tree. We predict that adrenergic control will be greatest in proximal arterioles, with progressive attenuation with increasing arteriolar order. Conversely, we predict that peptidergic and purinergic control will be greatest in distal arterioles, with progressive attenuation with decreasing arteriolar order. Finally, we anticipate that theoretical estimates of hemodynamic consequences will differ based on predicted topologically-dependent SNS control.

4.2 Materials and methods

4.2.1 Animal care and use

Experimental protocols were approved by The Council on Animal Care at the University of Western Ontario. Experiments were performed using 27 male Sprague–Dawley rats (six to seven weeks old; mass: 170 ± 12 g, mean \pm SD), purchased from Charles River Laboratories (Saint-Constant, Quebec, Canada), and housed on site for at least one week prior to the study. Rats were housed in animal care facilities of the University of Western Ontario, at 24°C on a 12–12 hour light–dark cycle with access to food and water *ad libitum*. At the end of the experiment, the anesthetized rat was euthanized with an overdose of α -chloralose and urethane cocktail mix (intraperitoneal injection), and cervical dislocation.

4.2.2 Anesthesia and skeletal muscle preparation

A more detailed description can be found elsewhere (Al-Khazraji *et al.*, 2012). Briefly, the rat was anesthetized with a cocktail of α -chloralose (80 mg/kg) and urethane (500 mg/kg) using intraperitoneal injection. The fur of the neck and lower back region were shaved, and the animal was tracheotomized and cannulated in both the jugular (for continuous intravenous drug delivery) and the carotid (for blood pressure recordings). Temperature was maintained at 37°C (rectal probe) using a customized temperature controlled platform. With the animal shaved and skin prepared, under microscopic guidance the GM muscle was cut from its origin along the spine and along its rostral and caudal borders. With great care taken to preserve its neurovascular supply, the muscle flap was gently reflected away from the rat, spread evenly onto a transparent Sylgard® (Sylgard 184; Dow Corning, Midland, MI, USA) pedestal to approximate in situ

dimensions and pinned to secure edges. The exposed tissue was superfused continuously (4–5 ml/min) with bicarbonate-buffered PSS (35°C at tissue, pH 7.4) of the following composition: NaCl 137 mM, KCl 4.7 mM, MgSO₄ 1.2 mM, CaCl₂ 2 mM, NaHCO₃ 18 mM, and equilibrated with 5% CO₂/95% N₂.

4.2.3 Intravital video microscopy (IVVM)

Upon completion of microsurgical procedures, the preparation was transferred to the stage of the intravital microscope (Olympus BX51, Olympus, Tokyo, Japan). The preparation was equilibrated for approximately 30 minutes, during which time the arteriolar network was observed for experimental sites of observation (vasomotion was not observed). Microvessels were imaged under Kohler illumination using a long working distance condenser (NA = 0.80) and a long working distance water immersion objective (Olympus LUMPLFL: 10× NA = 0.30; depth of field ~9 μm) with illumination from a 100-Watt halogen light source. The optical image was coupled to an EMCCD camera (Qimaging Rolera EMC², Qimaging©, Surrey, BC, Canada), viewed using specialized imaging software (MetaMorph 7.6, Molecular Devices Inc., Sunnyvale, CA, USA), and stored on a hard drive for offline analysis. Following equilibration, the baseline internal vessel lumen diameter was recorded and arterioles were tested for oxygen sensitivity by elevating superfusate O₂ from 0% to 21% (5% CO₂, balance N₂) for 5 minutes, and recording arteriolar diameter (Table 4.1). Equilibration with 5% CO₂–95% N₂ was restored for the duration of experimental procedures. Bright-field video (.tiff) images were collected (17 fps) under Kohler bright-field illumination for off-line analysis of internal vessel lumen diameters using ImageJ software (Schneider *et al.*, 2012).

4.2.4 Experimental protocols

All working solutions of drugs were prepared fresh daily and dissolved in the gassed and warmed PSS solution. The highest dose of drug was initially prepared, followed by preparation of the other concentrations of drug using a dilution series with logarithmic increments (dissolved in gassed PSS). Each concentration level was independently stored in its own tightly-sealed storage bottle, and placed in a heated water bath to maintain solution temperature of 37°C. Two water jacketed reservoir units (Radnoti LLC, CA, USA) were set up: 1) one provided warmed and gassed PSS that was gravity fed from a larger reservoir bottle, and 2) the other was used only for drug delivery. Each solution was then poured into the heated reservoir unit, and was topically applied to the preparation via gravity feed. Once the arteriolar responses for a given drug concentration were recorded, the solution in the reservoir was replaced with the next higher dose of drug solution. This procedure was repeated throughout concentration–response determinations. All solutions were pre-gassed prior to mixture, and received continuous bubbling of gas within the chamber to ensure continuous and homogenous gassing of the solution. For treatment with antagonists, the desired concentration was similarly prepared as a combined solution of agonist and antagonist.

Protocol 1: Regional activation of α 1R, α 2R, Y1R, and P2X1R

Five groups of animals were used to evaluate arteriolar responses to phenylephrine (PE; α 1R specific agonist; Sigma Aldrich, MO, USA), UK 14,304 (α 2R specific agonist; Tocris Biosciences, MO, USA), neuropeptide Y (NPY; Tocris Biosciences, MO, USA), and ATP (Sigma Aldrich, MO, USA). ATP has been shown to exhibit both vasoconstrictor [via P2X1R activation; (Hopwood & Burnstock, 1987)] and vasodilator

(Hellsten *et al.*, 1998) effects; therefore, in an effort to isolate ATP-mediated vasoconstriction (Buckwalter *et al.*, 2004), we conducted a separate set of experiments with a fifth group of animals receiving α,β -methylene ATP ($\alpha\beta$ -meATP; potent P2X1 receptor agonist; Sigma Aldrich, MO, USA), a stable non-degradable ATP analogue. All experiments were conducted in the rat GM arteriolar network, with one agonist evaluated per animal. Arteriolar responses were recorded at log increments (PE: 10^{-9} to 10^{-4} M; UK 14,304: 10^{-9} to 10^{-5} M; NPY: 10^{-13} to 10^{-8} M; ATP: 10^{-9} to 10^{-4} M; $\alpha\beta$ -meATP: 10^{-9} to 10^{-5} M), and were evaluated when diameter responses stabilized and remained static for a minimum of 5 to 10 minutes.

4.2.5 Selection of agonist concentrations

In all cases, the concentrations selected for each agonist application ranged from physiological resting levels to supra-physiological levels in an attempt to maximize constriction responses. The ranges selected for PE and UK 14,304 were based off of resting plasma levels of norepinephrine [1 to 4 nM (Mortensen *et al.*, 2012)], and high intensity exercise [\sim 50 nM (Stratton & Halter, 1985)]. The range selected for NPY concentrations were from resting conditions (\sim 1 pM), to high physiological stress such as high intensity exercise (10 pM), or vaginal birth delivery (\sim 10 nM) (Hirsch & Zukowska, 2012).

In an effort to characterize ATP's baseline activity as a vasoconstrictor (Galligan *et al.*, 2001; Gitterman & Evans, 2001; Erlinge & Burnstock, 2008), as well as its role in vasodilation as seen in exercise concentrations [2 μ M (Hellsten *et al.*, 1998)], we selected ATP concentrations which represented interstitial skeletal muscle levels ranging from resting conditions [\sim 100 nM (Mortensen *et al.*, 2011)] to those noted during heavy

exercise (Hellsten *et al.*, 1998). The range selected for $\alpha\beta$ -meATP encompassed the above ATP range, and is similar with the range used in a previous study (Buckwalter *et al.*, 2004).

4.2.6 Experimental data collection

Arteriolar responses at varying branch orders (from 1A to 5A) were recorded at each log increment of agonist concentration. The tissue was then superfused with PSS and arteriolar diameters were restored to that of baseline. Finally, maximal diameter responses to superfused sodium nitroprusside (SNP, 10^{-5} M) were recorded (Table 4.1). At baseline and during all drug interventions, continuously branching sets of arteriolar trees were scanned and imaged from 1A to 5A. Next, the same arteriolar tree was scanned and imaged from 5A to 1A to confirm that vessel responses were stable and there were no temporally-dependent alterations in responses during image scans. The total scanning/imaging time (1A to 5A, then from 5A to 1A) was under 30 seconds. In all cases, the responses at the beginning and end of imaging did not differ, indicating that there were no changes in responses over the scanning period.

Protocol 2: Selectivity of α 1R, α 2R, Y1R, and P2X1R agonist

To confirm specific functional responses to agonists, agonist data were also collected in the face of specific receptor antagonist delivery (α 1R antagonist: prazosin at 2×10^{-8} M; α 2R antagonist: yohimbine at 10^{-6} M; Y1R antagonist: BIBP3226 at 2×10^{-8} M; and P2X1R antagonist: NF023 at 10^{-6} M). Concentrations of antagonists were selected based on pilot work conducted in our laboratory that showed successful blockade at EC50 values of agonist.

4.2.7 Tissue viability and inclusion criteria

Preparations were evaluated for oxygen sensitivity as a means to test for vascular responsiveness. As well, responses to oxygen (before beginning agonist delivery protocol) and SNP (after completion of experimental protocol) were used as a metric (independent of the tested variables) to determine repeatability between preparations. Preparations that did not respond to either oxygen or SNP were discarded from data inclusion. All 27 animals used in this study responded physiologically to both O₂ and SNP (Table 4.1).

4.2.8 Arteriolar order classification

The arteriolar network was classified using the centrifugal arteriolar classification method (Ellsworth *et al.*, 1987), as follows: the first order (1A) was set as the first bifurcation coming off the feed vessel that entered the proximal end of the tissue. Each large bifurcation following thereafter was classified as the next generation of arterioles; e.g., second order (2A) daughter vessels bifurcated off a 1A vessel, *etc.* (Wiedemann, 1962; Boegehold & Johnson, 1988; Moore *et al.*, 2010).

To normalize arteriolar order classification across experiments and to avoid bias, we used the following criteria to define changes in branch order: 1) branch angle between two arterioles at a bifurcation must be less than 90° and greater than 15°, 2) bifurcations coming off of 1A to 3A must not bifurcate directly into a capillary bed, but rather give rise to another bifurcation (i.e., a bifurcation coming off a 3A is labeled a 4A arteriole and should give rise to 5A vessels, instead of a capillary bed), and 3) the diameters of the two arterioles at a bifurcation must be less than 80% of parent vessel diameter. As reported in other preparations (Murrant & Sarelius, 2000), the larger bifurcations (1A to 3A) of the

GM preparation were observed to be paired with the venular tree, while the smaller orders (4A to 5A) did not run alongside the venular tree.

In an effort to ensure only continuously branching arteriolar trees were analyzed, we outlined the arteriolar tree considered for observation and subsequent analysis was outlined using the following criteria: 1) each order must give rise to a subsequent interconnected series of bifurcations (i.e., a tree was outlined by selecting a 1A that is followed by 2A, *etc.* until 5A), and 2) similarly, each order, with the exception of 1A, must have bifurcated in line with a parent vessel that was within the same connected series of arterioles. For example, 4A vessel data were only accepted if that 4A bifurcation originated from a 3A vessel included in the original chosen arteriolar tree path.

4.2.9 Computational modelling

Computational modelling is useful in integrating measurements of diameter changes at various levels in the arteriolar tree to determine the resulting changes in overall network resistance and blood flow (Pries *et al.*, 1994). This is particularly important when seeking to compare the overall effects of SNS receptor activation between proximal and distal arterioles. Modelling is also useful in determining how measured diameter changes coordinate to alter flow distribution within the arteriolar tree, which requires having an accurate representation of *in vivo* network geometry. Thus, in an effort to estimate the hemodynamic consequences arising from SNS receptor activation along the branching arteriolar tree network, we incorporated our experimental findings into an in-house developed computational flow model.

We consistently observed high network homology across all rat GM preparations; thus, our model was developed from a single rat GM preparation that represented the topological mean of all experimental animals observed at baseline. Certainly, network homology has been reported in the mouse GM preparation (Bearden *et al.*, 2004). For blood flow simulations, arteriolar tree geometry was determined from vascular reconstructions using IVVM image montages of the rat GM and consisted of 27 unbranched (outlet) vessels. The arteriolar tree was discretized into 111 segments with a mean length of 33 μm and blood flow was calculated assuming a fixed pressure drop (7 mmHg) between the inlet segment (1A arteriole) and all the outlet segments (4A and 5A arterioles). At the inlet segment the discharge hematocrit was set to 0.42 (the normal value for blood sample hematocrit in these animals). Arteriolar orders were mathematically determined to best represent the ordering scheme used in the experimental analysis (order increasing at bifurcations when a vessel had a diameter <80% of parent, or a bifurcation angle > 15°).

A previously described two-phase (RBCs, and plasma) continuum blood flow model was used (Goldman & Popel, 2000, 2001). Based on the *in vivo* rheological model of Pries *et al.* (1994, 1990) the two-phase continuum flow model was used to calculate the steady-state distribution of total blood flow (Q) and discharge hematocrit (H_D) throughout the arteriolar tree. The flow model uses conservation equations for blood and RBC volume flow into each node j:

$$\sum Q_{iji} = 0,$$

$$\sum HD_{ij}Q_{iji} = 0,$$

where each vessel segment ij is labeled by its end nodes and the sums are over all nodes i connected to node j . The flow in segment ij is given by the pressure difference (Δp_{ij}) along the segment divided by the hydrodynamic resistance of the segment. The pressure-flow relationship is described by

$$Q_{ij} = \frac{\pi R^4 \Delta p_{ij}}{8 \mu_{pl} \mu_{rel} L}$$

where L and R are the length and radius of the vessel segment being considered, μ_{pl} is the viscosity of plasma, and μ_{rel} is the relative viscosity of blood which depends on both radius and hematocrit [Fahraeus-Lindqvist effect; (Pries *et al.*, 1990)]. The nonlinear relationship between RBC flow distribution at vessel bifurcations and overall blood flow distribution [plasma skimming effect; (Pries *et al.*, 1994; Goldman & Popel, 2000)] is also included in the model. The nonlinear rheological effects included in the model make it necessary to solve the steady-state equations using an iterative method (Pries *et al.*, 1994; Goldman & Popel, 2000). For the arteriolar geometries considered, the Matlab® flow simulation code typically required ~30 steps and <10 seconds to converge to a fixed solution for all node pressures, segment flows and hematocrits.

For baseline blood flow calculations, the arteriolar diameters used in the model were those measured under control conditions (i.e., in the absence of any SNS agonists or antagonists in the superfusion solution). In a separate set of experiments ($n = 39$ vessels), the computational model was validated against *in vivo* blood flow measurements, using the “streak length” method (Al-Khazraji *et al.*, 2012), in continuously branching arteriolar trees from the rat GM preparation under baseline control conditions.

To computationally determine hemodynamic consequences from experimental data, constriction levels for the various cases were input into the model as a function of both vessel order and drug concentration (evaluated from *in vivo* changes in constriction at PE, UK 14,304, ATP at 10^{-9} to 10^{-6} M, and NPY at 10^{-13} to 10^{-10} M). These data were used to alter diameters throughout the model arteriolar tree, based on a vessel ordering consistent with the experimental approach, and then the flow model described above was used to calculate the resulting hemodynamics. Total network flow, resistance, and RBC flow heterogeneity (coefficient of variation of RBC volume flow, i.e., standard deviation divided by mean) at each order were calculated for the given reconstructed network.

4.2.10 Data presentation and statistical analyses

Experimental data are presented as mean \pm SEM, except where otherwise stated.

Summary data for baseline diameters, responses to O₂ (O₂ Response = $D_{O_2} - D_{Baseline}$; in μm) and SNP (SNP Response = $D_{SNP} - D_{Baseline}$; in μm) are summarized in Table 4.1. For

constriction responses, values were calculated as changes from baseline diameter [% constriction = $(D_{Baseline} - D_{Response}) / D_{Baseline} \times 100\%$]. Reactivity between orders was

determined as percent change differences [$(\% \text{ constriction}_A - \% \text{ constriction}_B) / \% \text{ constriction}_A \times 100\%$, where A and B correspond to two different arteriolar orders]. At

each concentration of agonist, a one-way ANOVA was conducted, to observe the effect of arteriolar order on level of arteriolar constriction, with alpha level of 0.05 for statistical significance. For each agonist-antagonist plot, individual t-tests were conducted at each concentration of drug to evaluate the effect of the antagonist on constriction for each order. In the event of unequal variance, a Welsh correction was applied to the t-test.

Data for each agonist treatment were fit to a variable-slope sigmoid and, where sigmoidal convergence was possible, compared. Due to dichotomous (vasodilatory and vasoconstrictor) responses to ATP application and variable responses among arteriolar orders to $\alpha\beta$ -meATP application, data did not converge and sigmoidal (LogEC50) analyses were not possible.

To compare concentration-response curves (LogEC50) with differing absolute maximum constriction responses (E_{Max}), data for PE, UK 14,304, and NPY were transformed using Graphpad Prism. Responses were normalized to their respective E_{Max} , where the minimum and maximum (y-axis) values were set to 0 and 100% respectively and the x-axis was converted to a logarithmic scale. LogEC50 values were then compared across all orders using a one-way ANOVA with alpha level of 0.05 for statistical significance, followed by Tukey's HSD post-hoc test.

Table 4.1: Summary values for 5 arteriolar orders.

Responses are reported as change (O_2 Response = $D_{O_2} - D_{Baseline}$; SNP Response = $D_{SNP} - D_{Baseline}$) from baseline values. Data reported as mean \pm S.E.M.

<u>Arteriolar Order</u>	<u>Baseline Diameter</u> <u>(μm)</u>	<u>O₂ Response</u> <u>(μm)</u>	<u>SNP Response</u> <u>(μm)</u>
1A	93 \pm 2	-11 \pm 1	24 \pm 3
2A	70 \pm 2	-9 \pm 1	22 \pm 3
3A	55 \pm 1	-8 \pm 1	22 \pm 2
4A	42 \pm 1	-7 \pm 1	12 \pm 1
5A	35 \pm 1	-5 \pm 1	11 \pm 1

4.3 Results

Protocols 1 & 2: Activation and selectivity of α 1R, α 2R, Y1R, and P2X1R agonist

To confirm the receptor-mediated effects of the sympathetic agonists used in this study, we conducted a subset of experiments in the face of antagonist delivery. In all cases, antagonism of receptors for sympathetic neurotransmitters abolished vasoconstriction to respective sympathetic agonists.

4.3.1 Phenylephrine data

There was an order-dependent effect of PE on arteriolar constriction (Fig. 4.1, Top panel; N=8 rats). Arteriolar constriction at maximum PE concentration (10^{-4} M) was greatest at 1A which progressively decreased with increasing arteriolar order, such that 1A were 85% more reactive than 5A. Constriction to maximum PE concentration (10^{-4} M) was blocked by prazosin ($P<0.05$), confirming that responses were due to α 1R activation. Phenylephrine LogEC50 values were different across arteriolar orders (Fig. 4.1, Bottom panel; $P<0.05$), where the LogEC50 values (M) were: 1A, -6.23; 2A, -6.42; 3A, -6.43; 4A, -6.00; 5A, -5.86. Specifically, LogEC50 for 2A was greater than 4A and 5A, and LogEC50 for 3A was greater than 4A and 5A ($P<0.05$).

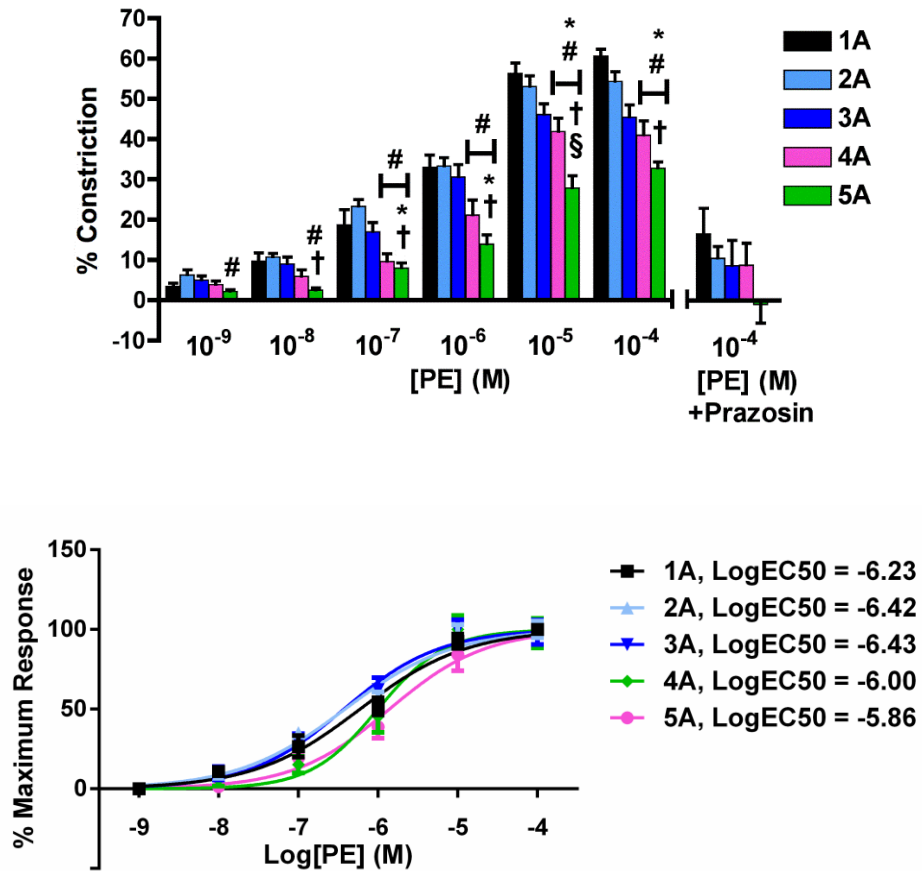


Figure 4.1: Arteriolar responses to α 1R activation at 5 arteriolar orders.

Top: Percent change in arteriolar constriction (from baseline) for 5 arteriolar orders (1A through 5A, $n = 8-17$ arterioles) at increasing concentrations (M) of phenylephrine (PE). Data presented as mean \pm S.E.M. * indicate different from 1A, # indicate different from 2A, † indicate different from 3A and § indicate different from 4A ($P < 0.05$). Constriction responses to peak concentrations of PE were blocked by prazosin (% indicates difference between responses with and without antagonist at PE 10^{-4} M, $P < 0.05$) for all orders.

Bottom: Normalized constriction responses fit to sigmoids. LogEC₅₀ values reported in legend for each arteriolar order. LogEC₅₀ values for 2A and 3A were greater than 4A and 5A ($P < 0.05$).

4.3.2 UK 14,304 data

There was an order-dependent effect of UK 14,304 on arteriolar constriction (Fig. 4.2, N=5 rats). Arteriolar constriction at maximum UK 14,304 (10^{-5} M) was greatest at 1A, 2A, and 3A, such that these arteriolar orders were up to 85% more reactive than 5A. Constriction to UK 14,304 at 10^{-7} to 10^{-6} M was blocked by yohimbine at all orders, and UK 14,304 at 10^{-5} M was blocked by yohimbine at 3A to 5A ($P<0.05$), confirming that responses were due to α_2R activation.

UK 14,304 LogEC50 values were similar across arteriolar orders (Fig. 4.2, Bottom panel), where the LogEC50 values (M) were: 1A, -7.07; 2A, -7.02; 3A, -7.26; 4A -7.19; 5A, -6.68.

4.3.3 Neuropeptide Y data

There was an order-dependent effect of NPY on arteriolar constriction (Fig. 4.3, Top panel; N=8 rats). Arteriolar constriction at maximum NPY concentration (10^{-8} M) was greatest at 5A, which progressively decreased with decreasing arteriolar order, such that 5A were 121% more reactive than 1A. Constriction to NPY at maximum concentration (10^{-8} M) was blocked by BIBP3226 ($P<0.05$), confirming that responses were due to Y1R activation.

NPY LogEC50 values were similar across arteriolar orders (Fig. 4.3, Bottom panel), where the LogEC50 (M) values were: 1A, -10.04; 2A, -10.28; 3A, -10.02; 4A -10.23; 5A, -10.59.

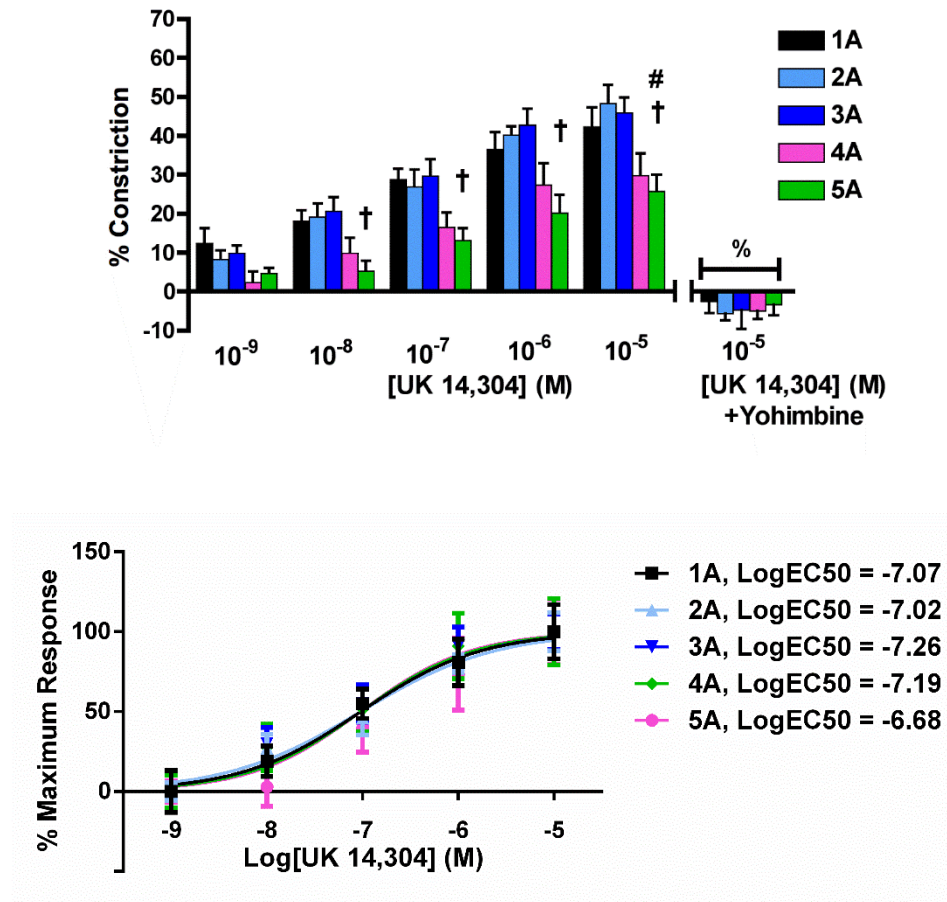


Figure 4.2: Arteriolar responses to α_2R activation at 5 arteriolar orders.

Top: Percent change in arteriolar constriction (from baseline) for 5 arteriolar orders (1A through 5A, $n = 6-22$ arterioles) at increasing logarithmic concentrations (M) of UK 14,304. Data presented as mean \pm S.E.M. # indicate different from 2A, and † indicate different from 3A ($P < 0.05$). Constriction responses to peak concentrations of UK 14,304 were blocked by yohimbine (% indicate difference between responses with and without antagonist at UK 14,304 10^{-5} M, $P < 0.05$) for all orders. **Bottom:** Normalized constriction responses fit to sigmoids. LogEC50 values are reported in legend, and were similar across arteriolar orders.

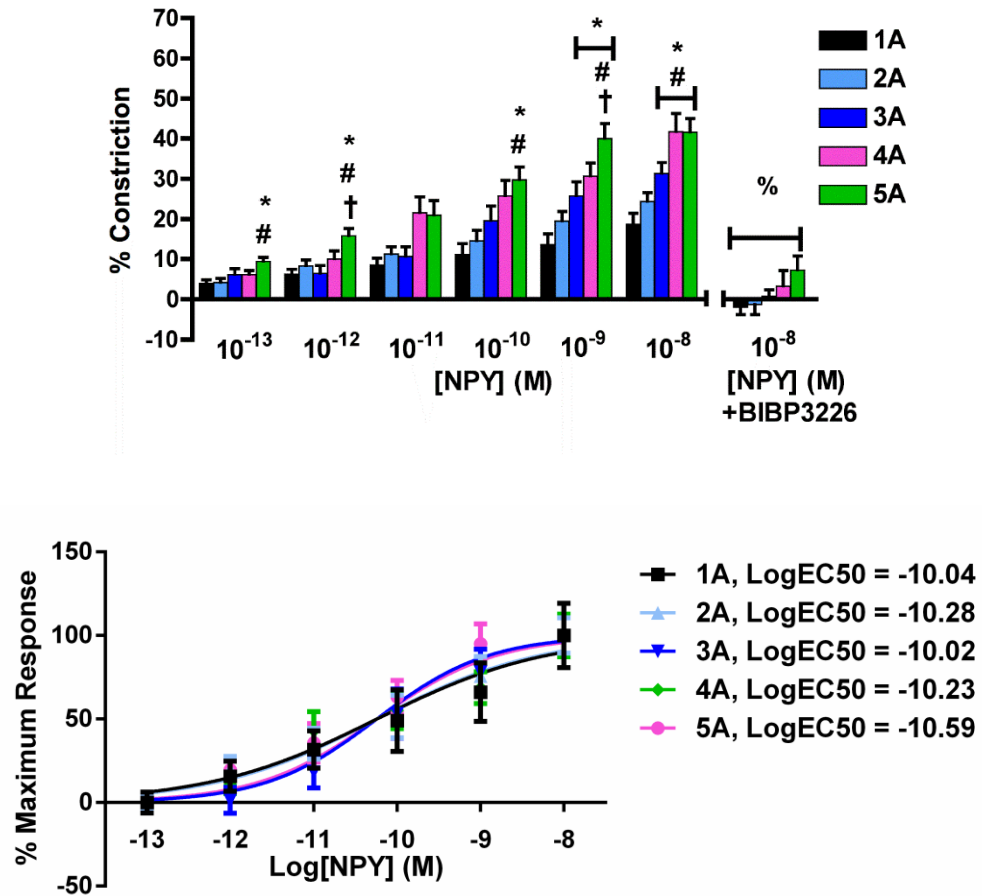


Figure 4.3: Arteriolar responses to Y1R activation at 5 arteriolar orders.

Top: Percent change in arteriolar constriction (from baseline) for 5 arteriolar orders (1A through 5A, n = 8-17 arterioles) at increasing logarithmic concentrations (M) of neuropeptide Y (NPY). Data presented as mean \pm S.E.M. * indicate difference from 1A, # indicate difference from 2A, and † indicate difference from 3A ($P < 0.05$). Constriction responses to peak concentrations of NPY were blocked by BIBP3226 (% indicate difference between responses both with and without antagonist, $P < 0.05$) for all orders.

Bottom: Normalized constriction responses fit to sigmoids. LogEC₅₀ values are reported in legend, and were similar across arteriolar orders.

4.3.4 ATP data

ATP produced concentration-dependent dichotomous arteriolar responses (Fig. 4.4).

Lower ATP concentrations (10^{-9} M to 10^{-7} M) evoked arteriolar constriction, with the following branch orders having the greatest level of constriction at each concentration:

10^{-9} M of ATP, 4A>1A and 3A; 10^{-8} M, 4A>1A; and 10^{-7} M, 4A>1A and 2A ($P<0.05$).

ATP evoked maximum arteriolar constriction at 10^{-8} M, with the following constrictor responses: 1A, 3.5%; 2A, 8%; 3A, 9%; 4A, 15%; 5A, 11%. These data indicate that 4A are the most responsive to ATP's constrictor effects.

At concentrations $>10^{-6}$ M, all orders dilated, with peak responses to maximal concentration of ATP 10^{-4} M as indicated: 1A, 18%; 2A, 22%; 3A, 24%; 4A, 17%; 5A, 21% (Fig. 4A).

Constriction to ATP at 10^{-9} to 10^{-7} M was blocked by NF023 (Fig. 4.5, $P<0.05$) indicating that responses to ATP were due to P2X1R activation.

4.3.5 α,β -methylene ATP data

All arteriolar orders constricted for the full concentration range of $\alpha\beta$ -meATP (Fig. 4.6).

Since $\alpha\beta$ -meATP is P2X1R specific, these data support that the dilation effects of ATP (shown in Fig. 4.4) were not P2X1R mediated. Furthermore, constriction effects of $\alpha\beta$ -meATP were blocked by NF023 (10^{-6} M) ($P<0.05$, Fig. 4.6).

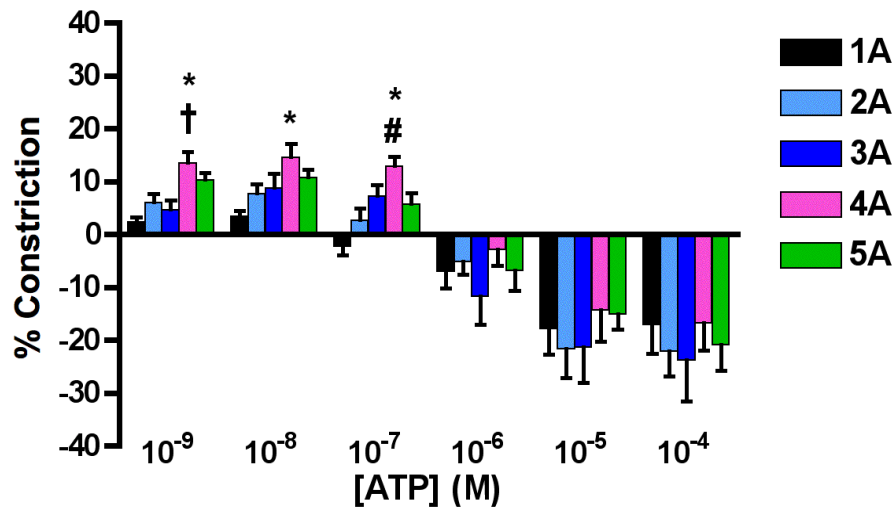


Figure 4.4: Arteriolar responses to ATP application at 5 arteriolar orders.

Percent change in arteriolar constriction (from baseline) for 5 arteriolar orders (1A through 5A, n = 6-22 arterioles) at increasing logarithmic concentrations (M) of adenosine triphosphate (ATP). Data presented as mean \pm S.E.M. A negative constriction is determined as a dilatory response. * indicate difference from 1A, # indicate difference from 2A, and † indicate difference from 3A ($P < 0.05$).

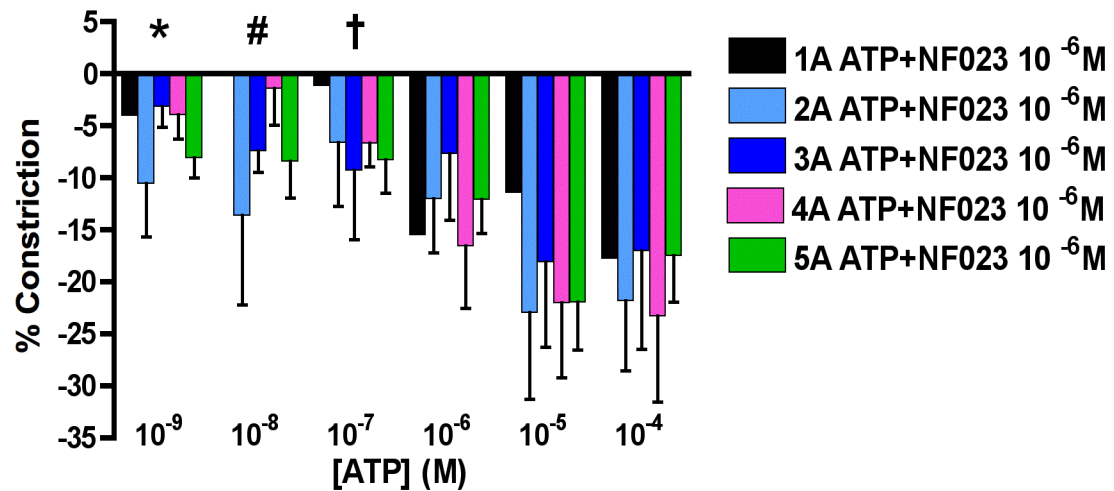


Figure 4.5: Arteriolar responses to ATP application with P2X1R blockade at 5 arteriolar orders.

Percent change in arteriolar constriction (from baseline) for 5 arteriolar orders (1A through 5A, $n = 5-20$ arterioles) at increasing logarithmic concentrations (M) of adenosine triphosphate (ATP) in the face of NF023 (P2X1R antagonist). Data presented as mean \pm S.E.M. A negative constriction is determined as a dilatory response. Data presented as mean \pm S.E.M. Constriction responses to ATP were blocked by NF023 for ATP concentrations of 10^{-9} M (* indicate difference in constriction responses for 2A-5A with and without antagonist, $P < 0.05$), 10^{-8} M (# indicate difference in constriction responses for 3A-5A with and without antagonist, $P < 0.05$), and 10^{-7} M († indicate difference in constriction responses for 4A-5A with and without antagonist, $P < 0.05$).

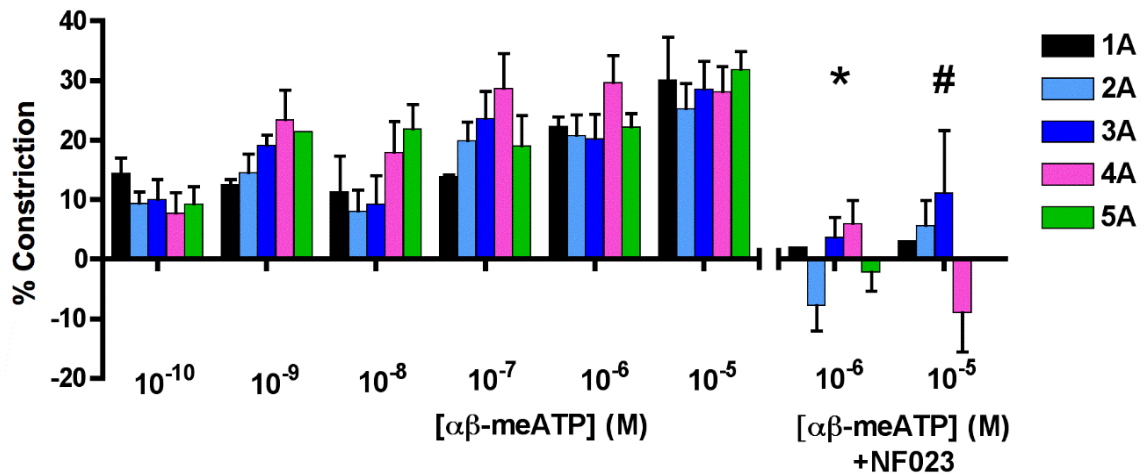


Figure 4.6: Arteriolar responses to $\alpha\beta$ -meATP application at 5 arteriolar orders.

Percent change in arteriolar constriction (from baseline) for 5 arteriolar orders (1A through 5A, $n = 5-15$ arterioles) at increasing logarithmic concentrations (M) of alpha-beta-methylene-ATP ($\alpha\beta$ -meATP). Data presented as mean \pm S.E.M. Constriction responses to $\alpha\beta$ -meATP were blocked by NF023 for $\alpha\beta$ -meATP concentrations of 10^{-6} M (*indicates difference in constriction responses for 2A, 4A-5A with and without antagonist, $P < 0.05$), and 10^{-5} M (#indicates difference in constriction responses for 4A with and without antagonist, $P < 0.05$).

4.3.6 Computational analysis: Calculating hemodynamic consequences from spatially-dependent SNS receptor activation

An arteriolar tree was modeled from *in vivo* network geometry, with centrifugal branch orders mathematically determined in the same way and represented using the same nomenclature (1A-5A) as in our experimental data analysis (Fig. 4.7). Comparison between computational calculations for baseline blood flow did not differ from experimental blood flow calculations, as slopes and intercepts between the two regression lines were similar (Fig. 4.8).

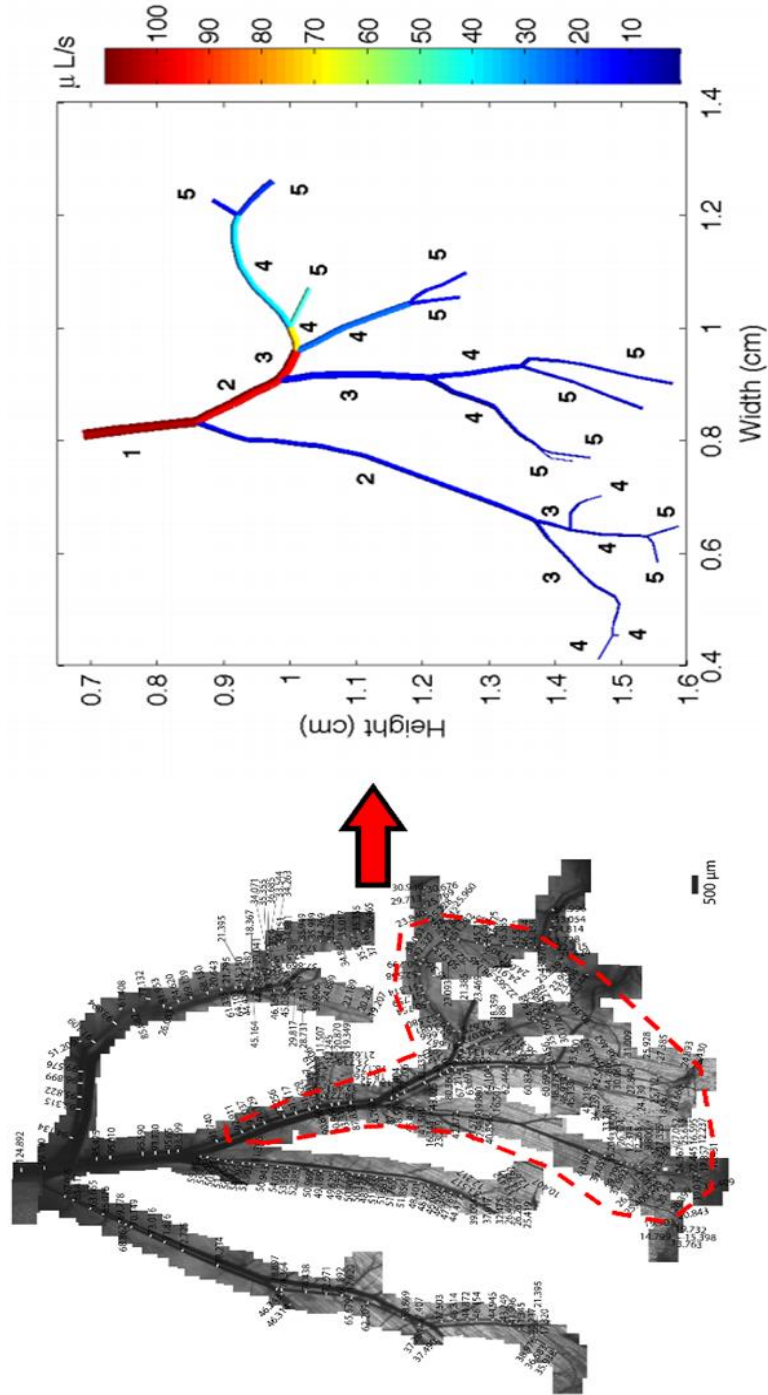


Figure 4.7: Computational network reconstruction schematic.

Numbers indicate arteriolar diameters (μm) on photomontage, and branch order on reconstructed network. The large vessel (inlet) is 1st order (1) and the smallest vessels (outlets) are 5th orders (5). Network is color-coded based on baseline (control) blood flow through vessel segments (from red being high flow to blue being low flow values).

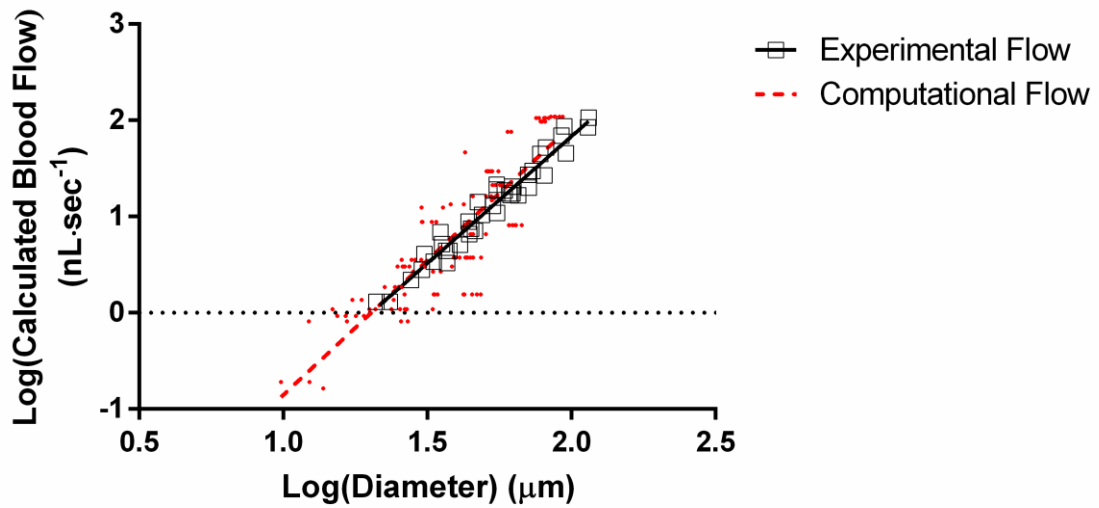


Figure 4.8: Validation of computational flow data with experimental flow data.

Comparison of blood flow values calculated from the computational model versus blood flow values calculated from experimental protocol. There was no significant difference between the slopes or the intercepts for both linear regressions. Experimental Flow: $\text{Log}(\text{Calculated Blood Flow}) = (2.64 \times \text{Log}(\text{Diameter})) - 3.44$; $r^2 = 0.96$, $P < 0.05$. Computational Flow: $\text{Log}(\text{Calculated Blood Flow}) = (2.79 \times \text{Log}(\text{Diameter})) - 3.65$; $r^2 = 0.76$, $P < 0.05$.

This reconstructed arteriolar tree was used in our hemodynamic calculations to obtain network flow (Fig. 4.9), total resistance (Fig. 4.10), and RBC flow heterogeneity at 2A-5A (Fig. 4.11). There was a progressive decrease in total flow within the simulated network with increasing concentrations of PE, UK and NPY (Fig. 4.9). Correspondingly, there was a progressive increase in total network resistance within the simulated network with increasing concentrations of PE, UK and NPY (Fig. 4.10). In parallel with the constriction data, ATP exhibited an effect on total flow and network resistance which was opposite to that of the other ligands; that is, ATP increased total flow with increasing concentration, and decreased network resistance with increasing concentration. Our group as well as our collaborators have previously shown that these results are attributed to ATP acting as a dilator at higher concentrations (Hellsten *et al.*, 1998; Nyberg *et al.*, 2013).

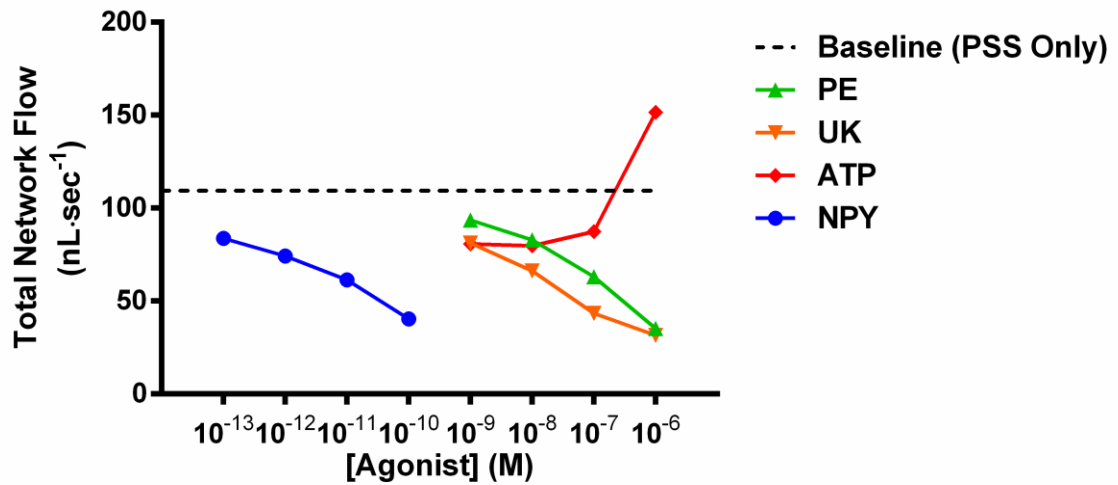


Figure 4.9: Calculated total network flow during baseline, and sympathetic receptor activation.

Calculated total network flow for baseline; PE, UK 14,304 (UK), and ATP from 10^{-9} to 10^{-6} M; NPY from 10^{-13} to 10^{-10} M. There was a progressive decrease in calculated total network flow with increasing concentration of agonist, with the exception of ATP as dilation occurs at higher concentrations.

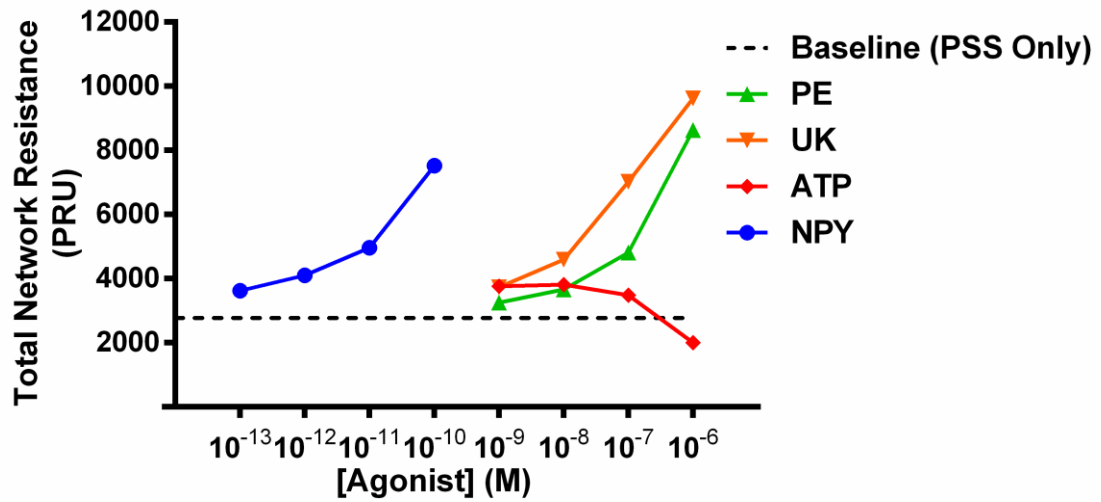


Figure 4.10: Calculated total network resistance during baseline, and sympathetic receptor activation.

Calculated total network resistance (PRU, peripheral resistance units) for baseline; PE, UK 14,304 (UK), and ATP from 10^{-9} to 10^{-6} M; NPY from 10^{-13} to 10^{-10} M. There was a progressive increase in calculated total network resistance with increasing concentration of agonist, with the exception of ATP as dilation occurs at higher concentrations.

To calculate changes in RBC flow heterogeneity, baseline heterogeneity was used as the reference value, and any changes from baseline heterogeneity were reflected as positive (increase in heterogeneity) or negative (decrease in heterogeneity) changes from baseline. This fractional change was calculated for each order (1A-5A) of the reconstructed network (Fig. 4.11). For 2A vessels, there was minimal change in RBC flow heterogeneity for all concentrations of the four ligands, with a maximum of 5% increase in heterogeneity exhibited by addition of 10^{-6} M UK 14,304. For 3A vessels, there was a 10-24% increase in RBC flow heterogeneity exhibited by PE and UK 14,304 at all concentrations, with smaller (~1-12%) effect of ATP and especially NPY. For 4A vessels, there was a progressive increase in RBC flow heterogeneity with increasing concentrations of PE and UK 14,304, and the greatest effect on heterogeneity (~50% increase) with 10^{-6} M concentration of UK 14,304. The changes in heterogeneity for 5A vessels do not follow a distinct pattern for each of the concentrations of UK 14,304 and ATP; however Fig. 4.11 serves to highlight two important outcomes: 1) PE and NPY have opposing effects on heterogeneity at 5A (increasing PE decreases heterogeneity while increasing NPY increases heterogeneity), and 2) while PE has a large impact on blood flow heterogeneity in the larger vessels (2A-4A), it decreases heterogeneity at 5A vessels.

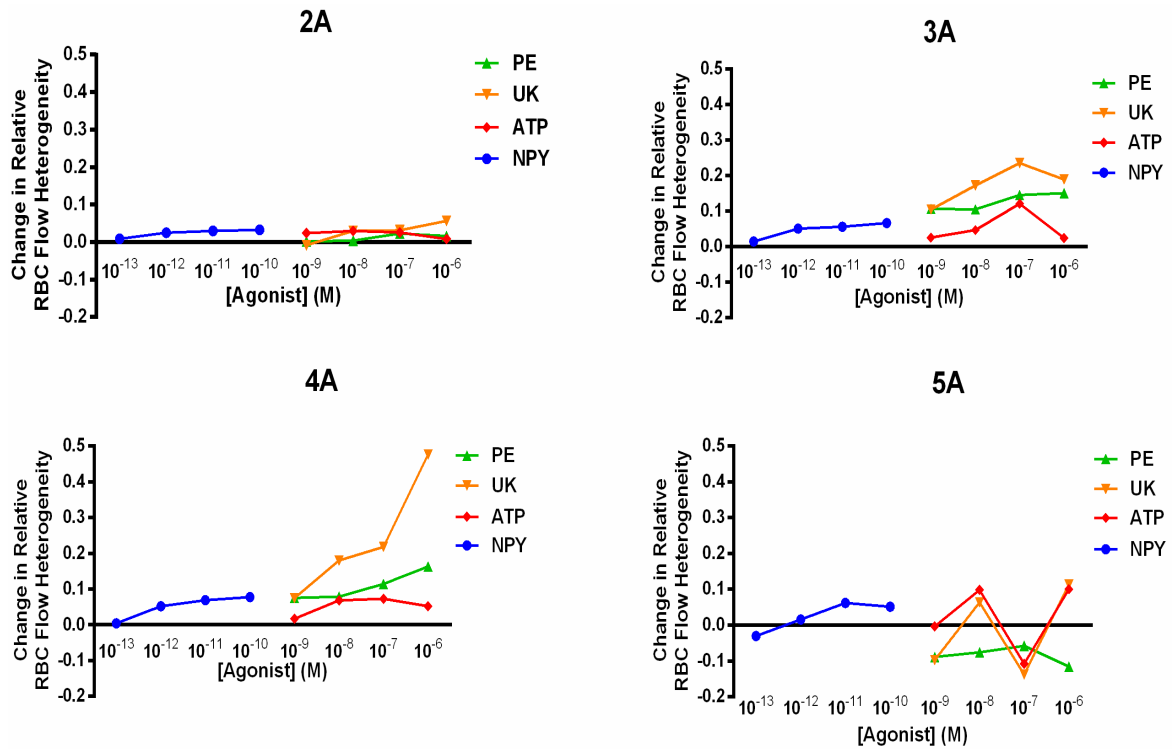


Figure 4.11: Change in RBC flow heterogeneity at 2A to 5A during sympathetic receptor activation.

The coefficient of variation of RBC flow heterogeneity as a function of agonist is normalized to baseline RBC flow heterogeneity. Heterogeneity is calculated for the following agonist concentrations: PE, UK 14,304 (UK), and ATP from 10^{-9} – 10^{-6} M; NPY from 10^{-13} – 10^{-10} M. Increase in heterogeneity is shown as a positive value, whereas decrease in heterogeneity is shown as a negative value.

4.4 Discussion

Herein we provide a comprehensive topological evaluation of sympathetic modulation in branching skeletal muscle arteriolar networks. This work provides much needed new data describing concentration- and order-dependent vasoconstrictor effects of adrenergic ($\alpha 1R$ and $\alpha 2R$), peptidergic (Y1R), and purinergic (P2X1R) receptor activation in complex skeletal muscle arteriolar trees. Furthermore, we have applied these experimental data to our computational blood flow model and described the hemodynamic consequences of heterogeneous modulation of receptors for sympathetic neurotransmitters across a skeletal muscle network. Our data support and build on the classic “adreno-centric” view of sympathetic vascular control, but most importantly illustrate equipotent roles for peptidergic and purinergic sympathetic components in skeletal muscle arteriolar hemodynamics.

4.4.1 Experimental findings: Topologically-dependent sympathetic control along arteriolar trees

4.4.1.1 Visualization and imaging of arteriolar networks

One of the prominent features of the rat GM muscle is its 2-dimensional planar geometry (Al-Khazraji *et al.*, 2012), whereby complete arteriolar networks can be quickly scanned and imaged with minimal changes in focal depth. For the present study, this enabled simultaneous and systematic evaluation of the topologically-dependent effects of sympathetic receptor activating receptors for sympathetic neurotransmitters along branching arteriolar trees (from 1A to 5A).

4.4.1.2 Topologically-dependent vasoconstrictor responses to adrenergic control

Prior studies describing differential α -adrenergic control in branching arterioles were limited to selected small groupings of arterioles in non-locomotive muscle (i.e., rat cremaster) (Faber, 1988; Ohyanagi *et al.*, 1991) or locomotive skeletal muscle arteriolar networks of limited branch orders (Moore *et al.*, 2010). In the rat cremaster, Faber (1988) binned groups of arterioles (based on luminal diameter) as either large or small. Where large arterioles were comprised of 1A and 2A (mean diameter of 100 μm) and small arterioles were comprised of 3A vessels (mean diameter of 25 μm). Ohyanagi *et al.* (1991) also used binning, but categorized large arterioles (mean diameter of 120 μm) as 1A, and terminal arterioles (mean diameter of 13 μm) as 3A vessels. Although their approach provided meaningful data, their binning approaches limited spatial resolution, which precludes topologically based analyses.

In the current study, arteriolar responses to PE were order-dependent, where 1A and 2A were 27% to 317% more reactive than 4A and 5A for the entire range of PE concentrations. As well, arteriolar constriction elicited by the highest PE concentration (10^{-4} M) was completely blocked by prazosin ($\alpha_1\text{R}$ antagonist; 2×10^{-8} M) (Fig. 4.1, Top panel). Although our data support many of the findings of Moore *et al.* (2010) on mice, we observed that 1A were most responsive to PE application, where they reported that 3A were most responsive to PE application. Although we cannot preclude species differences (i.e., rat versus mouse), such discrepancies are likely attributed to fundamental differences in experimental protocol. Specifically, Moore *et al.* applied a narrow PE concentration range (10^{-9} to 10^{-6} M) that did not elicit plateaus in arteriolar response

curves, suggesting that responses did not reach maximum constriction. In contrast, we employed a broader PE concentration range (10^{-9} to 10^{-4} M), resulting in maximum arteriolar constriction (i.e., plateau responses). Applying higher PE concentrations (10^{-5} and 10^{-4} M), we demonstrated that 1A and 2A constrict greater than 3A (Fig. 4.1, Top panel).

Since EC50 represents the potency of ligands on arteriolar responses and since efficacy (E_{Max}) differed among arteriolar orders, then arteriolar responses were normalized and plotted as concentration-response curves. In response to PE, LogEC50 differed among orders (Fig. 4.1, Bottom panel; $P < 0.05$), where LogEC50 of 2A and 3A were greater than 4A and 5A. Our data show that PE has greater potency (i.e., LogEC50) and efficacy (E_{Max} ; Fig. 4.1, Top panel) in proximal versus distal arterioles. These data suggest that proximal arterioles may have either greater receptor density and/or binding affinity; however, conclusions describing receptor density and/or binding affinity are beyond the scope of this study.

Arteriolar responses to UK 14,304 (α_2R activation, Fig. 4.2, Top panel) were order dependent, where (at 10^{-8} to 10^{-5} M) 2A was 87% to 261% and 3A was 78% to 289% more reactive than 5A vessels ($P < 0.05$). E_{Max} values in 2A and 3A were 87% and 78% greater, respectively, than E_{Max} in 5A (Fig. 4.2, Top panel). Since all arteriolar orders received the same range of agonist concentrations and reached plateaus in response, these E_{Max} data illustrate the profound efficacy of UK 14,304 in proximal versus distal arterioles. In contrast, there were no differences in LogEC50 values across arteriolar orders in response to UK 14,304 (Fig. 4.2, Bottom panel), illustrating its similar potency among all arteriolar orders.

As previously discussed, Faber (1988) and Ohyanagi *et al.* (1991) binned arterioles (based on luminal diameter), which is fundamentally different than the ordering scheme used in the current study. Despite differences in arteriolar nomenclature, strictly comparing based on diameters instead of orders, our data are in alignment with Faber and with Ohyanagi *et al.*, in that we too found that “larger” arterioles (~100 μm) responded more to $\alpha 2\text{R}$ activation than “smaller” arterioles (~25 μm). However, strictly comparing based on arteriolar orders, we were not able to resolve differences among 1A-3A for $\alpha 2\text{R}$ activation.

Recently, Moore *et al.* (2010) reported that 1A (versus 2A and 3A) were most responsive to $\alpha 2\text{R}$ activation (via UK 14,304) in the GM of the C57BL/6 mouse. This is in contrast to our current data where we observed the greatest responses to UK 14,304 in 2A and 3A vessels in the GM of the rat. Albeit, our findings are in direct alignment with work completed in the cremaster of the C57BL/6 mouse by Moore *et al.* (2010). These findings highlight the complexity in arteriolar control among different species and experimental preparations. Notably, topological differences in microvascular networks between different species may contribute to such discrepancies in comparison and interpretation. To illustrate, our laboratory has recently published that there are at least 4 orders of arterioles (from 1A to terminal arterioles) in the same C57BL/6 mouse (Novielli & Jackson, 2014). In contrast, we reported up to 6 orders of arterioles (from 1A to terminal arterioles) in the Sprague-Dawley rat GM (Al-Khazraji *et al.*, 2012). The microvasculature is designed to provide adequate O_2 delivery to the muscle tissue, yet the geometry is constrained by the dimensions of the capillary bed (as capillary size does not scale with species (West *et al.*, 1997)); therefore, the pre-capillary arterioles should

behave the same despite the difference in species. Based on noted differences in network complexity, it could be argued that a 4A arteriole in the mouse should be similar hemodynamically to a 5A or 6A arterioles in the rat; however this remains to be tested. If SNS control of arteriolar networks is order-dependent, then we would expect subtle differences in control among species and preparations with differing arteriolar network complexities.

4.4.1.3 Topologically-dependent vasoconstrictor response to peptidergic control

In the current study, arteriolar responses to NPY were order-dependent, where 5A was 70% to 151% more reactive than 1A and 2A (Fig. 4.3, Top panel; $P < 0.05$). As well, arteriolar constriction elicited by the highest NPY concentration (E_{Max} ; 10^{-8} M) was completely blocked by BIBP3226 (Y1R antagonist; 2×10^{-8} M) (Fig. 4.3, Top panel; $P < 0.05$). E_{Max} values in 4A and 5A were 124 and 71% greater than E_{Max} in 1A and 2A respectively (Fig. 4.3, Top panel). Since all arteriolar orders received the same range of agonist concentrations and reached plateaus in responses, these E_{Max} data illustrate the profound efficacy of NPY in distal versus proximal arterioles. However, there were no differences in $LogEC_{50}$ values across arteriolar orders in response to NPY (Fig. 4.3, Bottom panel), illustrating its similar potency among all arteriolar orders.

Our data are the first to show differential responses to Y1R activation as a function of arteriolar order. To date, there have been few studies that have directly investigated the effects of NPY on branching skeletal muscle arteriolar trees (from 1A to pre-terminal arterioles). Although we believe we are the first to describe NPY effects in locomotive skeletal muscle arteriolar networks, Joshua (1991) was the first to examine NPY-induced

arteriolar tree vasoconstriction in the rat cremaster studied by IVVM (Joshua, 1991). Despite fundamental differences in approach, and that their data were limited to only 3 generations of arterioles, their findings are in close agreement with those in the current study.

To test the effect of NPY on vascular resistance in the cat gastrocnemius muscle, Ekelund & Erlinge (1997) used arterially infused NPY and indirect estimations of resistance changes from pressure/bulk flow relationships. Although their data lacked spatial resolution (i.e., detailed topology) and simply indicated that NPY provided preferential vasoconstriction in small-bore (<25 μm) compared to large-bore (>25 μm) arterioles, our findings are in general agreement.

Our data further corroborate previous work which showed NPY's prominent role in regulating distal microvasculature (Joshua, 1991; Jackson *et al.*, 2004; Evanson *et al.*, 2012). However, these past studies were limited in scope and did not provide any information on network topology or order dependency. For example, Evanson *et al.* (2012) limited their investigation to isolated 1A vessels from rat gastrocnemius muscle, Jackson *et al.* (2004) made generalized inferences from bulk blood flow profiles measured at the femoral artery of rats, and Joshua (1991) limited findings to 3 arteriolar orders in non-locomotive skeletal muscle (cremaster).

4.4.1.4 Topologically-dependent vasoconstrictor response to purinergic control: Dichotomous effects of ATP

In the current study, arteriolar responses to ATP were order-dependent, where 4A was up to 333% more reactive than 1A (for 10^{-9} to 10^{-7} M), 285% more reactive than 2A (at 10^{-7} M) and 189% more reactive than 3A (at 10^{-9} M). ATP exhibited vasoconstriction (at low

concentrations) and vasodilation (at high concentrations) (Fig. 4.4). ATP-mediated vasoconstriction was primarily a result of P2X1R activation (Fig. 4.5), as vasoconstrictor effects were completely blocked by application of NF023 (a specific P2X1R antagonist; 10^{-6} M) (Fig. 4.5, $P < 0.05$). While ATP has been more commonly described as a vasodilator (Hellsten *et al.*, 1998; Clifford & Hellsten, 2004; Mortensen *et al.*, 2009), the vasoconstriction elicited by ATP in this study is in agreement with work reported from experiments in the rat tail and hindlimb (Johnson *et al.*, 2001), and the rat heart (Hopwood & Burnstock, 1987).

ATP acts on P2X receptors, located on the abluminal smooth muscle of the vessel (Hirst & Jobling, 1989), as well as P2Y receptors (responsible for dilation), located on the intraluminal endothelium (Burnstock, 1996). In the current study, ATP promoted vasoconstriction in all arteriolar orders at 10^{-9} and 10^{-8} M, (Fig. 4.4, $P < 0.05$). However, with progressive increases in ATP concentration (10^{-6} and 10^{-5} M), we observed vasodilation in all arteriolar orders ($P < 0.05$). Interestingly, similar ATP concentrations in exercising human skeletal muscle have been reported, where interstitial ATP levels (measured from intramuscular microdialysate) ranged between 2 to 5×10^{-6} M, depending on exercise intensity (Hellsten *et al.*, 1998).

During micropipette application of ATP to arterioles in the hamster cheek pouch preparation, the vasodilator effect of interstitial ATP was suggested to be mediated (in part) by the formation of adenosine (from ATP degradation) via 5'-ectonucleotidase activity (Duza & Sarelius, 2003). This mechanism of ATP-mediated dilation (via breakdown to adenosine) would then differ from intravascular ATP-mediated dilation which is solely based on ATP binding onto P2Y receptors residing on the endothelium

(and is independent of adenosine's vasodilatory effects). While Duza and Sarelius applied ATP at concentrations of 10^{-7} M to 10^{-3} M, we used lower concentrations of ATP (10^{-9} to 10^{-7} M), which elicited vasoconstriction. Our conditions correspond to interstitial ATP concentrations measured with intramuscular microdialysis at baseline in humans (Mortensen *et al.*, 2011). The results from the current and past experiments suggest that 5'ectonucleotidase is either not active at low concentrations of ATP, or that the breakdown of ATP to adenosine does not override the vasoconstrictor effects of ATP for these concentrations.

We recently reported that vasodilation, and ensuing blood flow changes, in response to high ATP concentrations (10^{-6} and 10^{-5} M) can be abolished by L-NA and indomethacin in the rat GM. Thus, the vasodilator effects of high abluminal ATP concentrations are best explained by NO and prostanoid formation, respectively (Nyberg *et al.*, 2013). Certainly, ATP can diffuse from the interstitial space into the vessel lumen and to invoke P2Y-mediated vasodilation; however a 50-fold difference in ATP concentration difference across the vessel wall is required for this cross over to occur (Mo & Ballard, 2001).

Notably, the whole blood concentration of ATP in the Sprague Dawley rat is 3 to 5×10^{-6} M (Jagger *et al.*, 2001), which would lead to no net flux of ATP from the interstitium to the blood in the current study. Thus, vasodilation induced by 10^{-6} to 10^{-5} M [ATP] in our study cannot be due to diffusion and subsequent P2Y activation.

When applying ATP in the face of P2X1R blockade, ATP acted as a vasodilator at all concentrations (Fig. 4.5, $P < 0.05$). These data suggest that ATP-induced vasodilation buffers its vasoconstrictor effects at all (physiologically relevant) concentrations. This was further corroborated by the pure vasoconstrictor effect of $\alpha\beta$ -meATP (Fig. 4.6) (also

blocked by NF023, highlighting vasoconstriction was specific to P2X1R activation), an ATP analogue that does not degrade at the same rate as ATP with high affinity for P2X1R receptors.

Based on our findings and that of previous work, we conclude that ATP acts as a vasoconstrictor in skeletal muscle so long as it 1) is not degraded to adenosine, 2) cannot cross over into the lumen to act on P2Y receptors, and/or 3) is available at low concentrations, as high concentrations of ATP induce NO and prostacyclin formation (Nyberg *et al.*, 2013) which masks ATP's capacity to vasoconstrict (Fig. 4.5). The dichotomous roles of ATP may serve to optimize resistance and perfusion pressure in contracting muscle (in areas of lower concentration) and, in areas of high concentration, participate in localized exercise-induced functional sympatholysis (Kirby *et al.*, 2011).

4.4.2 Computational findings: Total network resistance and flow changes as a result of a differential distribution of receptors for sympathetic neurotransmitters

The inlet, or 1A, vessel to the arteriolar network provides the bulk flow to the outlets (or all the 5A vessels); therefore, having access to tree geometry allows for calculation of “upstream” and “downstream” effects on hemodynamics as a result of topologically-dependent differential responses of arterioles to activation of receptors for sympathetic neurotransmitters. The ability to assess the “up/downstream” effects is unique to network analysis, and underscores the benefit of analyzing networks of interconnected bifurcations, as opposed to acquiring data from single sites of observation (Pries *et al.*, 1995c).

In our previous work, we speculated that Y1R blockade (via BIBP3226) modulated downstream systemic vascular resistance, as shown by changes in diastolic conductance of the rat hindlimb (Jackson *et al.*, 2004). A remarkable outcome of our present hemodynamic calculations was that NPY greatly contributed to total network resistance. NPY decreased calculated network flow to the same degree as PE (Fig. 4.9); however, NPY operated in a range of concentrations that were 1000x lower than PE. Per mole of concentration, it can be stated that NPY is a more potent vasoconstrictor, and therefore greatly contributes to resistance, when compared to either PE or UK 14,304 alone. As previously stated, this highlights the importance of understanding the consequent implications of neurotransmitter contribution, despite its concentration in the interstitial milieu. Microvascular surface area increases with progressively increasing arteriolar order, with the greatest level of surface area exhibited by the capillaries (Poole *et al.*, 2013).

4.4.2.1 Order and diameter-dependent changes in RBC heterogeneity as a result of a differential distribution of receptors for sympathetic neurotransmitters

Progressing down the arteriolar network, there is an increase in the number of arteriolar bifurcations, and a progressive decrease in hematocrit of single vessels for a given order (compared to parent orders) (Pries *et al.*, 1986). This assists in providing a baseline level of heterogeneous RBC delivery to capillary beds, where RBC flow preference is given to the daughter with the greater diameter (or path of lower resistance). It follows that small changes in resistance at the smaller (distal) arterioles, will result in robust changes in hematocrit (Pries *et al.*, 1990).

Traditionally, dilatory mechanisms have been put forth as the primary means for RBC distribution within the microvasculature (Clifford & Hellsten, 2004). From our experimental data, we illustrate that sympathetic ligands can promote differential and topologically-dependent changes in resistance for a wide range of ligand concentrations. We postulate that this is carried out through differential SNS control across the microcirculation. A topologically-dependent arrangement of sympathetic control would enable the SNS to coordinate with intrinsic dilatory mechanisms to precisely titrate RBC delivery throughout the network. With regards to the concept of phase separation, where blood flow fraction delivery is more sensitive to changes in resistance of smaller compared to larger arterioles (Pries *et al.*, 1990), topologically-dependent SNS receptor activation warrants large hemodynamic consequences in terminal arterioles feeding into capillary beds.

4.5 Conclusion

To conclude, we have comprehensively and systematically determined network responses to cumulative concentrations of specific sympathetic agonists among 5 arteriolar orders, and used these responses to mathematically determine the functional consequence(s) of heterogeneous sympathetic receptor distribution on network hemodynamics. We have shown differential responses to sympathetic ligands along the arteriolar tree, such that proximal arterioles are largely under adrenergic control, while distal arterioles are largely under peptidergic and purinergic control. Using computational modelling, we calculated that the adrenergic component of blood flow regulation is mainly responsible for maintaining total flow to the tissue, while the peptidergic and/or purinergic component(s) contribute both to total network resistance/flow and to RBC flow distribution within the

network. Finally, we have indicated that alongside the adrenergic system, the peptidergic and purinergic components of the SNS carry out integral roles in sympathetically-mediated microvascular control.

Our theoretical model illustrates that, due to topologically-dependent modulation, the SNS affects RBC heterogeneity differentially at each arteriolar order (Fig. 4.11). Under baseline healthy conditions, such control would contribute to setting baseline resistance and RBC distribution. At the onset of both healthy aging (Narkiewicz *et al.*, 2005) and cardiovascular diseases (Malpas, 2010), there exist concomitant increases in SNA, which may then act to exaggerate blood flow heterogeneity (Jackson *et al.*, 2010) and further exacerbate microvascular dysfunction, perhaps via upregulation of any or all of the receptors for sympathetic neurotransmitters. Certainly, in high stress conditions, Y1R is upregulated in microvessels of injured carotid arteries (Li *et al.*, 2005); as well, hypertensive patients have shown increased P2X1R activation (Steinmetz *et al.*, 2000; Hollah *et al.*, 2001). Our model flow calculations showed that (compared to PE and UK) NPY and ATP produced higher RBC flow heterogeneity (relative to baseline) in distal (5A) vessels (Fig. 4.11), indicating that heightened SNS receptor activation, as in disease conditions, would elicit detrimental consequences to RBC delivery.

4.6 References

- Al-Khazraji BK, Novielli NM, Goldman D, Medeiros PJ & Jackson DN. (2012). A simple "streak length method" for quantifying and characterizing red blood cell velocity profiles and blood flow in rat skeletal muscle arterioles. *Microcirculation* **19**, 327-335.
- Bearden SE, Payne GW, Chisty A & Segal SS. (2004). Arteriolar network architecture and vasomotor function with ageing in mouse gluteus maximus muscle. *J Physiol* **561**, 535-545.

- Boegehold MA & Johnson PC. (1988). Response of arteriolar network of skeletal muscle to sympathetic nerve stimulation. *Am J Physiol* **254**, H919-928.
- Buckwalter JB, Taylor JC, Hamann JJ & Clifford PS. (2004). Do P2X purinergic receptors regulate skeletal muscle blood flow during exercise? *Am J Physiol Heart Circ Physiol* **286**, H633-639.
- Burnstock G. (1996). P2 purinoceptors: historical perspective and classification. *Ciba Found Symp* **198**, 1-28; discussion 29-34.
- Burnstock G. (2007). Physiology and pathophysiology of purinergic neurotransmission. *Physiol Rev* **87**, 659-797.
- Clifford PS & Hellsten Y. (2004). Vasodilatory mechanisms in contracting skeletal muscle. *J Appl Physiol (1985)* **97**, 393-403.
- Dodd LR & Johnson PC. (1991). Diameter changes in arteriolar networks of contracting skeletal muscle. *Am J Physiol* **260**, H662-670.
- Duza T & Sarelius IH. (2003). Conducted dilations initiated by purines in arterioles are endothelium dependent and require endothelial Ca²⁺. *Am J Physiol Heart Circ Physiol* **285**, H26-37.
- Ekelund U & Erlinge D. (1997). In vivo receptor characterization of neuropeptide Y-induced effects in consecutive vascular sections of cat skeletal muscle. *Br J Pharmacol* **120**, 387-392.
- Ellsworth ML, Liu A, Dawant B, Popel AS & Pittman RN. (1987). Analysis of vascular pattern and dimensions in arteriolar networks of the retractor muscle in young hamsters. *Microvasc Res* **34**, 168-183.
- Erlinge D & Burnstock G. (2008). P2 receptors in cardiovascular regulation and disease. *Purinergic Signal* **4**, 1-20.
- Evanson KW, Stone AJ, Samraj E, Benson T, Prisby R & Kluess HA. (2012). Influence of estradiol supplementation on neuropeptide Y neurotransmission in skeletal muscle arterioles of F344 rats. *Am J Physiol Regul Integr Comp Physiol* **303**, R651-657.
- Faber JE. (1988). In situ analysis of alpha-adrenoceptors on arteriolar and venular smooth muscle in rat skeletal muscle microcirculation. *Circ Res* **62**, 37-50.
- Galligan JJ, Hess MC, Miller SB & Fink GD. (2001). Differential localization of P2 receptor subtypes in mesenteric arteries and veins of normotensive and hypertensive rats. *J Pharmacol Exp Ther* **296**, 478-485.

- Gitterman DP & Evans RJ. (2000). Properties of P2X and P2Y receptors are dependent on artery diameter in the rat mesenteric bed. *Br J Pharmacol* **131**, 1561-1568.
- Gitterman DP & Evans RJ. (2001). Nerve evoked P2X receptor contractions of rat mesenteric arteries; dependence on vessel size and lack of role of L-type calcium channels and calcium induced calcium release. *Br J Pharmacol* **132**, 1201-1208.
- Goldman D & Popel AS. (2000). A computational study of the effect of capillary network anastomoses and tortuosity on oxygen transport. *J Theor Biol* **206**, 181-194.
- Goldman D & Popel AS. (2001). A computational study of the effect of vasomotion on oxygen transport from capillary networks. *J Theor Biol* **209**, 189-199.
- Hellsten Y, Maclean D, Radegran G, Saltin B & Bangsbo J. (1998). Adenosine concentrations in the interstitium of resting and contracting human skeletal muscle. *Circulation* **98**, 6-8.
- Hirsch D & Zukowska Z. (2012). NPY and stress 30 years later: the peripheral view. *Cell Mol Neurobiol* **32**, 645-659.
- Hirst GD & Jobling P. (1989). The distribution of gamma-adrenoceptors and P2 purinoceptors in mesenteric arteries and veins of the guinea-pig. *Br J Pharmacol* **96**, 993-999.
- Hollah P, Hausberg M, Kosch M, Barenbrock M, Letzel M, Schlatter E & Rahn KH. (2001). A novel assay for determination of diadenosine polyphosphates in human platelets: studies in normotensive subjects and in patients with essential hypertension. *J Hypertens* **19**, 237-245.
- Hopwood AM & Burnstock G. (1987). ATP mediates coronary vasoconstriction via P2x-purinoceptors and coronary vasodilatation via P2y-purinoceptors in the isolated perfused rat heart. *Eur J Pharmacol* **136**, 49-54.
- Jackson DN, Moore AW & Segal SS. (2010). Blunting of rapid onset vasodilatation and blood flow restriction in arterioles of exercising skeletal muscle with ageing in male mice. *J Physiol* **588**, 2269-2282.
- Jackson DN, Noble EG & Shoemaker JK. (2004). Y1- and alpha1-receptor control of basal hindlimb vascular tone. *Am J Physiol Regul Integr Comp Physiol* **287**, R228-233.
- Jagger JE, Bateman RM, Ellsworth ML & Ellis CG. (2001). Role of erythrocyte in regulating local O2 delivery mediated by hemoglobin oxygenation. *Am J Physiol Heart Circ Physiol* **280**, H2833-2839.

- Johnson CD, Coney AM & Marshall JM. (2001). Roles of norepinephrine and ATP in sympathetically evoked vasoconstriction in rat tail and hindlimb in vivo. *Am J Physiol Heart Circ Physiol* **281**, H2432-2440.
- Joshua IG. (1991). Neuropeptide Y-induced constriction in small resistance vessels of skeletal muscle. *Peptides* **12**, 37-41.
- Kiowski W, Hulthen UL, Ritz R & Buhler FR. (1983). Alpha 2 adrenoceptor-mediated vasoconstriction of arteries. *Clin Pharmacol Ther* **34**, 565-569.
- Kirby BS, Crecelius AR, Voyles WF & Dinunno FA. (2011). Modulation of postjunctional alpha-adrenergic vasoconstriction during exercise and exogenous ATP infusions in ageing humans. *J Physiol* **589**, 2641-2653.
- Li L, Jonsson-Rylander AC, Abe K & Zukowska Z. (2005). Chronic stress induces rapid occlusion of angioplasty-injured rat carotid artery by activating neuropeptide Y and its Y1 receptors. *Arterioscler Thromb Vasc Biol* **25**, 2075-2080.
- Malmstrom RE, Balmer KC & Lundberg JM. (1997). The neuropeptide Y (NPY) Y1 receptor antagonist BIBP 3226: equal effects on vascular responses to exogenous and endogenous NPY in the pig in vivo. *Br J Pharmacol* **121**, 595-603.
- Malpas SC. (2010). Sympathetic nervous system overactivity and its role in the development of cardiovascular disease. *Physiol Rev* **90**, 513-557.
- Marshall JM. (1982). The influence of the sympathetic nervous system on individual vessels of the microcirculation of skeletal muscle of the rat. *J Physiol* **332**, 169-186.
- Mo FM & Ballard HJ. (2001). The effect of systemic hypoxia on interstitial and blood adenosine, AMP, ADP and ATP in dog skeletal muscle. *J Physiol* **536**, 593-603.
- Moore AW, Jackson WF & Segal SS. (2010). Regional heterogeneity of alpha-adrenoreceptor subtypes in arteriolar networks of mouse skeletal muscle. *J Physiol* **588**, 4261-4274.
- Mortensen SP, Gonzalez-Alonso J, Nielsen JJ, Saltin B & Hellsten Y. (2009). Muscle interstitial ATP and norepinephrine concentrations in the human leg during exercise and ATP infusion. *J Appl Physiol (1985)* **107**, 1757-1762.
- Mortensen SP, Nyberg M, Winding K & Saltin B. (2012). Lifelong physical activity preserves functional sympatholysis and purinergic signalling in the ageing human leg. *J Physiol* **590**, 6227-6236.

- Mortensen SP, Thaning P, Nyberg M, Saltin B & Hellsten Y. (2011). Local release of ATP into the arterial inflow and venous drainage of human skeletal muscle: insight from ATP determination with the intravascular microdialysis technique. *J Physiol* **589**, 1847-1857.
- Murrant CL & Sarelius IH. (2000). Coupling of muscle metabolism and muscle blood flow in capillary units during contraction. *Acta Physiol Scand* **168**, 531-541.
- Narkiewicz K, Phillips BG, Kato M, Hering D, Bieniaszewski L & Somers VK. (2005). Gender-selective interaction between aging, blood pressure, and sympathetic nerve activity. *Hypertension* **45**, 522-525.
- Novielli NM & Jackson DN. (2014). Contraction-evoked vasodilation and functional hyperaemia are compromised in branching skeletal muscle arterioles of young pre-diabetic mice. *Acta Physiol (Oxf)* **211**, 371-384.
- Nyberg M, Al-Khazraji BK, Mortensen SP, Jackson DN, Ellis CG & Hellsten Y. (2013). Effect of extraluminal ATP application on vascular tone and blood flow in skeletal muscle: implications for exercise hyperemia. *Am J Physiol Regul Integr Comp Physiol* **305**, R281-290.
- Ohyanagi M, Faber JE & Nishigaki K. (1991). Differential activation of alpha 1- and alpha 2-adrenoceptors on microvascular smooth muscle during sympathetic nerve stimulation. *Circ Res* **68**, 232-244.
- Poole DC, Copp SW, Ferguson SK & Musch TI. (2013). Skeletal muscle capillary function: contemporary observations and novel hypotheses. *Exp Physiol* **98**, 1645-1658.
- Pries AR, Ley K & Gaehtgens P. (1986). Generalization of the Fahraeus principle for microvessel networks. *Am J Physiol* **251**, H1324-1332.
- Pries AR, Secomb TW & Gaehtgens P. (1995a). Design principles of vascular beds. *Circ Res* **77**, 1017-1023.
- Pries AR, Secomb TW & Gaehtgens P. (1995b). Structure and hemodynamics of microvascular networks: heterogeneity and correlations. *Am J Physiol* **269**, H1713-1722.
- Pries AR, Secomb TW, Gaehtgens P & Gross JF. (1990). Blood flow in microvascular networks. Experiments and simulation. *Circ Res* **67**, 826-834.
- Pries AR, Secomb TW, Gessner T, Sperandio MB, Gross JF & Gaehtgens P. (1994). Resistance to blood flow in microvessels in vivo. *Circ Res* **75**, 904-915.

- Ruffolo RR, Jr., Nichols AJ, Stadel JM & Hieble JP. (1991). Structure and function of alpha-adrenoceptors. *Pharmacol Rev* **43**, 475-505.
- Schneider CA, Rasband WS & Eliceiri KW. (2012). NIH Image to ImageJ: 25 years of image analysis. *Nat Methods* **9**, 671-675.
- Segal SS. (2005). Regulation of blood flow in the microcirculation. *Microcirculation* **12**, 33-45.
- Steinmetz M, Bierer S, Hollah P, Rahn KH & Schlatter E. (2000). Heterogenous vascular effects of AP5A in different rat resistance arteries are due to heterogenous distribution of P2X and P2Y(1) purinoceptors. *J Pharmacol Exp Ther* **294**, 1182-1187.
- Stratton JR & Halter JB. (1985). Effect of a benzodiazepine (alprazolam) on plasma epinephrine and norepinephrine levels during exercise stress. *Am J Cardiol* **56**, 136-139.
- West GB, Brown JH & Enquist BJ. (1997). A general model for the origin of allometric scaling laws in biology. *Science* **276**, 122-126.
- Wiedemann MP. (1962). Lengths and diameters of peripheral arterial vessels in the living animal. *Circ Res* **10**, 686-690.

Chapter 5: General discussion

5.1 Development of the gluteus maximus skeletal muscle preparation

The investigation of *in vivo* skeletal muscle hemodynamics is greatly limited by inaccessibility to vascular networks of interest, and a lack of effective methods for acquiring *in vivo* hemodynamic parameters. In the thesis herein, we introduced a novel rat gluteus maximus (GM) skeletal muscle preparation which allows the greatest level of access to a microvascular network compared to any other published skeletal muscle preparation (i.e., widest range of reported vessel diameters, and orders). This high level of accessibility comes as a result of 3 characteristics intrinsic to the preparation: 1) there is an inherently large microvascular network (compared to mouse GM) due to a large mass of skeletal muscle which requires a greater blood supply, 2) the GM muscle is a highly active locomotive muscle which requires dense vasculature for maintaining adequate tissue metabolic integrity (Bearden *et al.*, 2004), and 3) the GM tissue is a thin muscle which allows for easy tissue transillumination, where its microvasculature is optimally positioned such that the entire network (arteriolar/venular trees, capillaries) is in a single focal plane (with minimal adjustment in fine focusing).

Through use of this GM preparation, we were able to nearly simultaneously scan multiple orders of arterioles for characterizing red blood cell velocity profiles as a function of vessel diameter, and evaluate vasoconstrictor responses from sub- to supra-physiological concentrations of 4 different sympathetic nervous system receptor agonists in multiple sequentially connected arteriolar orders. We took advantage of the planar layout of the vasculature and collected overlapping microscopic images of the arteriolar network such that we were able to computationally reconstruct an arteriolar network while preserving

its native *in vivo* geometry. This reconstructed network served as the basis for calculating hemodynamic parameters (e.g., blood flow, resistance, and red blood cell flow heterogeneity) as a consequence of topologically-dependent activation of sympathetic nervous system receptors for neurotransmission.

The utility of the GM preparation has begun to receive recognition, as it has been recently used alongside cellular and human data to show that interstitial ATP-mediated dilation in the microvasculature is dependent on prostanoid and nitric oxide formation in the rat GM muscle (Nyberg *et al.*, 2013). Additionally, the GM preparation was adapted for use in the hamster, where its data were compared to those from the rat cremaster which showed prostaglandins were involved in contraction-induced vasodilation in microvascular networks that were not secondary to the presence of extraluminal adenosine (Murrant *et al.*, 2014). As the GM preparation is one of the few true locomotive skeletal muscle microvascular preparations, it is foreseeable that it will continue to serve as a standalone microvascular preparation, or at least, accompany data collected from other *in vivo* preparations as a form of data validation or correlation.

5.2 Development of a method for calculating blood flow in fast-flowing arterioles

While blood flow techniques have been greatly improved upon, pushing past some of the previous limitations, the acquisition of centerline velocity via dual sensor technique, and assuming the Baker Wayland ratio of 1.6 (Baker & Wayland, 1974) for blood flow calculations remains to be the most utilized method for calculating *in vivo* blood flows in skeletal muscle microvascular networks (Duling *et al.*, 1982; Segal & Duling, 1987; Hester & Duling, 1988; VanTeeffelen & Segal, 2006; Jackson *et al.*, 2010).

The wide use of the Baker Wayland ratio of 1.6 is a direct consequence of limited data characterizing *in vivo* skeletal muscle velocity RBC profile shapes, as use of this ratio has been criticized for introducing errors in velocity, and therefore blood flow calculations (Pittman & Ellsworth, 1986; Tangelder *et al.*, 1986). These limitations arise as a result of both utilizing skeletal muscle preparations which provide access to a narrow range of vessel diameters, and the lack of a blood flow measurement technique which can be used to acquire *in vivo* velocity profile shapes for a large range of diameters.

Following the development and refinement of the GM preparation, we employed use of fluorescently-labeled red blood cells to act as tracers within the microvascular network in the GM muscle. As these labeled red blood cells maintained their intrinsic characteristics (e.g., biconcavity, and deformability), and the fraction of injected labeled red blood cells (1% of total blood volume) did not affect total hematocrit within the system, these fluorescent red blood cells acted as flow tracers which were representative of the native red blood cell flow patterns found within the microvasculature. Limiting the *in vivo* labeled fraction of red blood cells to 1% allowed for high contrast imaging between the labeled and unlabeled red blood cells. We then took advantage of our dual bright-field/epi-fluorescent microscopy system by optimizing camera exposure time during data acquisition. This allowed for these labeled red blood cells to form “streaks” of light along the vessel, displaying distance traveled in the time that the camera shutter was opened and closed, thus providing a way to measure *in vivo* red blood cell velocities. With the increase in network visibility provided by the GM preparation, we were able to measure these velocities across the vascular lumen, for an entire arteriolar tree spanning multiple branch orders. These data are the first of their kind for providing much needed

information on velocity profile shapes in skeletal muscle microvasculature that can be immediately implemented in blood flow calculations.

For true parabolic velocity profiles, the fixed velocity ratio ($V_{\text{Max}}/V_{\text{Mean}}$) would be 2, as the centerline velocity would be twice that of the mean velocity through the vessel. Baker and Wayland (Baker & Wayland, 1974) discovered that the average velocity profile through glass tubes had a blunted velocity profile shape where the centerline velocity was 1.6 times greater than the mean velocity averaged over the lumen. While Baker and Wayland assumed a parabolic velocity profile, the resulting velocity ratio factor of 1.6 comes as a consequence of spatial averaging that is inherent to the dual sensor red blood cell velocity measurement technique. Certainly, *in vivo* findings collected from the rabbit mesentery preparation have contradicted a constant velocity ratio for all diameters, as these velocity ratios were determined to be diameter-dependent (Tangelder *et al.*, 1986).

The consequences of assuming a fixed velocity ratio are striking, as subsequent blood flow calculations would thereby over- or under-estimate blood flow values compared to using a diameter-dependent velocity ratio value. Specifically, our data show that using a velocity ratio of 1.6 for calculating blood flow in arterioles with diameters less than or greater than $\sim 65 \mu\text{m}$ would result in under- and over-estimation of blood flow by up to 20%, respectively. Similar to Tangelder *et al.*, in the thesis herein, we also developed a diameter-dependent velocity ratio equation; however, the equation we provide, to our knowledge, is the first to describe diameter-dependent velocity ratios for skeletal muscle arterioles for a wide range of arteriolar diameters encompassing feed to pre-terminal arterioles (compared to a range of 17-32 μm in the rabbit mesentery (Tangelder *et al.*, 1986)). As well, the velocity ratio equation provided in this thesis (Chapter 2)

encompasses a large range of diameters, allowing it to be accessible for use in other microvascular preparations. As previously mentioned, data acquisition via use of the dual sensor technique is widely accepted, with many fundamental advancements in the field of microcirculatory hemodynamics made through its use. Certainly, we do not suggest that the dual sensor technique (or other red blood cell velocity measurement techniques) be replaced by use of our fluorescently-labeled red blood cell velocity measurement technique. We do recommend that our diameter-dependent velocity ratio equation be used, in conjunction with these measurement techniques, to determine an appropriate velocity ratio for use in blood flow calculations, as opposed to utilizing a constant velocity ratio such as the Baker Wayland ratio of 1.6. It should be noted that we recommend that the experimentally-derived velocity ratio equation be constrained for use in arteriolar diameters within the appropriate diameter range (21-115 μm).

Indeed, there are other groups who have identified a velocity ratio equation that varies with hemodynamic parameters. For instance, in the seminal work carried out by Pittman and Ellsworth (1986) in the arterioles and venules of the hamster retractor muscle, a velocity profile bluntness parameter (“B”) was estimated as a function of both diameter and the centerline dual sensor velocity. This parameter has been beneficial in determining velocity ratios for use in mathematical modelling of the rat mesentery (Pries *et al.*, 1989); however, as highlighted in their conclusions (Pittman & Ellsworth, 1986) their study was not based on absolute *in vivo* velocity calibrations such that any estimates made using their bluntness factor are subject to confounding variables that are inherent in the use of the dual sensor technique. Despite the fact that their bluntness parameter was not based on *in vivo* velocity calibrations, use of this parameter in calculation of velocity ratios is

far more advantageous than assuming a fixed velocity ratio. Our velocity ratio equation, described in the thesis herein, was derived from *in vivo* red blood cell velocity calibrations and only requires diameter as an input variable which can easily be collected from intravital experiments.

Moreover, the diameter-blood flow relationships acquired using our “streak length” velocity measurement technique was in accordance with diameter-blood flow relationships for both the rat cremaster muscle (Mayrovitz & Roy, 1983; House & Lipowsky, 1987), and the theoretical “cubic law” first described by Murray (Murray, 1926). Therefore, we prescribe use of our velocity ratio equation over others as it is derived from *in vivo* red blood cell velocity measurements, and the diameter-blood flow relationship derived in our study is in agreement with that found by other groups.

5.3 Use of *in vivo* red blood cell velocity profiles for estimating wall shear stress

Shear rate, or as commonly referred to pseudoshear rate, estimates the average shear rate across a vessel lumen, and requires input of mean velocity across lumen and luminal diameter. At low shear or pseudoshear rates, red blood cell aggregation increases and effective viscosity increases, attributing to the shear-thinning non-Newtonian behavior of blood (Chien *et al.*, 1967). Similar to blood flow calculations, the Baker Wayland ratio is used to convert centerline red blood cell velocity to acquire mean velocity values for use in calculating wall shear rate and stress and pseudoshear rate in microvascular preparations. In the thesis herein, we showed that using a constant velocity ratio, such as the Baker Wayland ratio of 1.6, would result in up to 25% difference in calculated values

compared to using our diameter-dependent velocity ratio function (Al-Khazraji *et al.*, 2012).

The widely accepted method for calculating wall shear rate, and wall shear stress, is dependent upon the assumption that the fluid flowing through a vessel segment is Newtonian (shear rate independent), follows a parabolic velocity profile as predicted by Poiseuille's law flow behaviour, and that this velocity profile shape is constant across the entire vascular network (Hester & Duling, 1988). It has been shown that the acceptance of these assumptions causes errors in wall shear stress calculations (Reneman *et al.*, 2006; Katritsis *et al.*, 2007); however, these assumptions are required due to the difficulty in acquiring *in vivo* velocity profile data. The techniques developed in the thesis herein allowed for computation of wall shear rates from *in vivo* velocity profiles for a range of arteriolar diameters (21-115 μm). These wall shear rates were 2-3 \times greater than those calculated from conventional approaches (Chapter 3, Fig. 3.8), and we were able to resolve differences between the various calculation methodologies.

It may be argued that any error resulting from conventional wall shear rate calculations is carried through; therefore, the absolute values of shear stress are not as important as the relative changes in shear rate between groups or for a given treatment. However, it is imperative to recognize that the discrepancy between calculated values is dependent upon the strong assumption that velocity profile shape is independent of diameter, and profile blunting can be incorporated into hemodynamic calculations by using a velocity ratio of 1.6. In fact, the calculation error is not linearly carried through for all diameters, as there is an under- and over-estimation of shear rate calculations depending on the arteriole of investigation (when comparing values calculated using a constant velocity ratio against

values calculated from use of diameter-dependent velocity ratios). Moreover, despite modifying the conventional wall shear rate equation to include velocity ratios as a function of diameter, the computation of wall shear rates under Poiseuille parabolic assumptions greatly underestimates wall shear rates compared to those derived from *in vivo* velocity profiles. With these reasons in mind, the discrepancy in values become more meaningful as they are grounded by assumptions which are deemed invalid by both theoretical (Sriram *et al.*, 2014) and experimental evidence (Reneman *et al.*, 2006; Reneman & Hoeks, 2008). Overall, the wall shear rate values calculated using our velocity profiles were significantly greater than the values calculated using conventional methods.

Certainly, the acquisition of velocity profiles required for the evaluation of *in vivo* wall shear rate and stress is challenging. With the “streak length” velocity measurement technique, we were able to acquire *in vivo* velocity profile data across numerous arteriolar orders; however, the most salient finding from this analysis was the development of a straightforward function for use alongside other velocity measurement techniques. Similar to the practical function we provided earlier, describing the relationship between arteriolar order and the velocity ratio required for *in vivo* blood flow calculations (Chapter 2, Equation 2.5), we described an equation which relates arteriolar diameter and centerline velocity to wall shear rate (Chapter 3, Equation 3.12). The utility of this equation can be extended to numerous aforementioned velocity and diameter measurement techniques that have been regularly used in *in vivo* experiments investigating control of skeletal muscle microcirculation. As well, due to the derivation of the equation (i.e., confined to the red blood cell free layer located between the edge of the

red cell column and the inner luminal wall), plasma viscosity is required for calculating wall shear stress. Plasma viscosity is mostly dependent on protein content (Kesmarky *et al.*, 2008), rather than vessel diameter, therefore it is acceptable to use a constant plasma viscosity value for calculating wall shear stress from wall shear rate values (Namgung *et al.*, 2011).

5.4 Recent use of “streak length” method in skeletal muscle microvascular studies

As previously mentioned, from the time of its development, the rat GM preparation has since been put to use by groups investigating skeletal muscle microvascular control mechanisms in both the rat (Nyberg *et al.*, 2013) and hamster GM muscles (Murrant *et al.*, 2014). In our collaborative study with Nyberg *et al.*, we also implemented the “streak length” red blood cell velocity measurement technique and were able to calculate changes in blood flow responses as a result of superfusion of ATP corresponding to interstitial ATP concentrations found during exercise. We were then able to recover these responses by blocking endothelial-mediated prostanoid and nitric oxide formation via superfusion of indomethacin and L-NA, respectively.

The results from this study demonstrate, for the first time, that increasing ATP concentration of skeletal muscle interstitial fluid, to concentrations measured in human and animal skeletal muscle interstitium during muscle contractions, results in both vasodilation and ensuing increases in blood flow within the skeletal muscle. This study was greatly strengthened by use of the GM and the “streak length” method for reasons described by: 1) experimental data were collected from a locomotive muscle resembling that of human muscle, 2) infusion of ATP via dialysis probes into human skeletal muscle

only results in local hemodynamic changes; therefore blood flow responses are undetectable, whereas the GM preparation coupled with the use of the “streak length” technique was able to provide detectable changes in blood flow responses, and 3) the GM preparation allowed for direct observation of vasodilation and blood flow responses, thereby confirming that ATP’s actions are located within the microvasculature. These findings greatly contribute to and corroborate findings in the human and rat microvascular endothelial cell data, and provide insight to the mechanisms associated with the interstitial ATP vasodilation response.

More recently, our laboratory has for the first time described the blood flow responses associated with the attenuation of vasodilation found in the skeletal muscle of pre-diabetic mice under electric field stimulation. Under both single tetanic and rhythmic muscle contraction paradigms, blood flow responses in branching arterioles of the pre-diabetic mouse GM muscle were attenuated by 50 to 80%, respectively, compared to that of control (Novielli & Jackson, 2014).

The use of fluorescently-labeled red blood cells in these experiments provides noteworthy advantages over the traditional method of solely collecting diameter data, followed by inferences made on changes in blood flow. Previously, the assumption was that the velocity profile shape (and therefore the velocity ratio) is not only diameter independent for baseline values, but is also independent of diameter changes that accompany vasodilation responses to muscle contraction. As previously stated, we found a strong linear relationship between arteriolar diameter and velocity ratio (a surrogate for velocity profile shape), therefore assuming a fixed velocity ratio of 1.6 would result in over- and/or under-estimation of hemodynamic responses to contraction both within and

between control and pre-diabetic groups; and 2) use of the “streak length” velocity measurement technique provided instantaneous hemodynamic data collection alongside the collection of geometrical data both during and after muscle contraction. This novel advancement in data collection provides insight on the time-course associated with blood flow responses to contraction. With our intravital video microscopy setup, we are able to acquire high frame rates, which allowed for minimal time spent on acquiring fluorescent red blood cell data, in between tracking arteriolar diameter changes throughout both contraction paradigms.

5.5 Use of “streak length” method for the validation of an in-house computational flow model

Finally, *in vivo* blood flow calculations determined by using the “streak length” technique have been used to validate our in-house computational flow model blood flow calculations. The planar geometry of the rat GM allowed for direct mapping and reconstruction of network geometry, which was used for network flow analysis by incorporating our computational flow model. The computational flow model assumed a fixed pressure drop across the reconstructed arteriolar network, and calculated blood flow based on resistance values calculated with input of arteriolar diameter measurements. When compared as functions of diameter, the slope and y-intercept values for the computational versus experimental blood flow calculations were similar, thereby validating the calculated outputs of our computational model. As this validation using data collected under baseline conditions, we were able to estimate hemodynamic changes that accompany changes in arteriolar diameters under the activation of sympathetic

nervous system receptors by incorporating the calculated levels of resistance from vasoconstrictor experimental data (Chapter 4).

Moreover, the benefit of validating our computational flow model is that we can now compute hemodynamic parameters that are otherwise difficult to acquire experimentally. For instance, while mapping the network geometry under bright-field microscopy is straight-forward (under stable hemodynamic conditions), acquiring “streak” velocity data for the entire network may prove to be challenging as there is a finite amount of fluorescent exposure the muscle can endure prior to being subject to fluorescent leakage from the labeled red blood cells. Fluorescent leakage is problematic as it results in a drastic decrease in contrast between the labeled red blood cells and the background. As we have collected experimental blood flow values for a large range of arteriolar diameters, the validation of the computational model implies that the model can interpolate blood flow values, for a greater number of vessel segments than what would be experimentally feasible.

The computational flow model can also be used to estimate flow changes during application of superfused agonists. The model relies on the input of diameter values at each node (i.e., one end of a finite vessel segment) of the reconstructed network, inlet hematocrit, and both inlet and outlet pressure values. Arteriolar diameters are acquired from *in vivo* data collection, inlet hematocrit is approximated to be near systemic values, with an assumed fixed pressure drop across the network. From these hemodynamic parameters, resistance is measured for each vascular segment, followed by calculation of theoretical blood flow values. In the thesis herein, we evaluated vasoconstrictor responses to several sympathetic nervous system receptor agonists across multiple consecutively

branching arteriolar orders. Our computational flow model was able to estimate changes in total resistance and blood flow throughout the entire reconstructed network, as well as red blood cell flow heterogeneity at each order in response to each receptor agonist.

5.6 Use of the rat GM for investigating SNS receptor functionality in branching arteriolar trees

The findings from this thesis include topologically-dependent responses to the activation of 4 SNS receptors in 5 consecutively branching arteriolar orders of the rat GM muscle. The collected data highlighted in this thesis represent the most comprehensive evaluation of SNS receptor activation in skeletal muscle arteriolar networks to date. Indeed, our work builds upon and is in agreement with other studies (Faber, 1988; Joshua, 1991; Ohyanagi *et al.*, 1991; Ekelund & Erlinge, 1997; Gitterman & Evans, 2000; Moore *et al.*, 2010) whose findings are summarized by Fig. 1.1 (Chapter 1); however, the work herein is the first of its kind to assess the topological dependence of adrenergic, purinergic, and peptidergic receptor activation in branching arteriolar segments of skeletal muscle microvasculature. Moreover, we are the first to estimate the ensuing changes in hemodynamic parameters as a result of topologically-dependent responses to SNS receptor activation.

Classically, the role of the SNS on skeletal muscle microvascular regulation has been understood to be primarily carried out through adrenergic control. This view has evolved from several experimental designs; namely: 1) upon either sympathetic neuronal stimulation (Marshall, 1982), or activation of adrenergic receptors via sympathetic agonist delivery (Faber, 1988; Ohyanagi *et al.*, 1991; Moore *et al.*, 2010), the sites of observation used in other studies for assessing vasoconstrictor responses were acquired

from proximal arterioles (1A to 3A) and did not include data from distal (4A to terminal) arterioles, and 2) while activation of purinergic P2X1 receptor (Buckwalter *et al.*, 2003) or NPY Y1R (Jackson *et al.*, 2004), via infusion of specific SNS receptor agonists, resulted in substantial increases in downstream resistance, activation of both Y1R and P2X1R have not been investigated using IVVM experiments; thus, it was unclear whether increases in resistance were due to vasoconstrictor responses at the feed artery, or downstream within the distal microcirculation.

The first experimental limitation was due to either a deliberate design in experimental protocol such that data were collected up until 3A vessels, or a significant increase in difficulty acquiring data beyond 3A vessels. In the case that the experimental protocol had been designed to limit data collection to 3A vessels, then importance was not placed on data collection beyond 3A. However, if data collection did not go beyond 3A vessels due to a lack of adequate visibility, then it is necessary to develop a preparation which allows for appropriate visibility of all vessels.

The second experimental limitation is also due to the lack of an appropriate skeletal muscle model for investigating the purinergic and peptidergic responses. However, similar to previous adrenergic data, the observation of purinergic and peptidergic vasoconstrictor responses were nevertheless possible at 1A-3A vessels. To our knowledge, there is a finite number of studies evaluating purinergic and peptidergic (Joshua, 1991) vasoconstrictor responses in skeletal muscle microvasculature; thus, limited purinergic and peptidergic responses may have been limited due to a lack of investigation.

5.7 Topologically-dependent SNS receptor activation and ligand contribution

We showed that proximal (1A to 3A) arterioles are more responsive to α 1R and α 2R activation than distal arterioles. Interestingly, the LogEC50 among the 5 arteriolar orders was different during α 1R activation (with phenylephrine, specific α 1R agonist, being least potent in 5A arterioles). There was no difference in LogEC50 among the 5 arteriolar orders during UK 14,304 delivery (specific α 2R agonist). The maximal efficacy to each of phenylephrine and UK 14,304 was significantly greater for proximal versus distal arterioles.

We showed that for a wide range of concentrations, ATP elicited a dichotomous response in arterioles: constriction at low concentrations (10^{-9} to 10^{-8} M), and dilation at higher concentrations ($>10^{-6}$ M) of ATP. Finally, we showed that distal arterioles are more responsive to Y1R activation than proximal arterioles. The LogEC50 among the 5 arteriolar orders was not different during Y1R activation; however, the maximal efficacy to NPY was significantly greater for distal versus proximal arterioles.

By strict comparison of agonist concentration, NPY is approximately 1000x more potent than the other SNS receptor agonists. Certainly, norepinephrine would cause a maximal efficacy much greater than that of phenylephrine and UK 14,304 (Moore *et al.*, 2010); however, despite the lack of norepinephrine data, we predict NPY would remain more potent even if these key data had been collected. The potency of NPY is evident even at physiological resting concentrations, where it is available at a 1000 \times lower concentration than that of norepinephrine (Abd-Allah *et al.*, 2004; Hirsch & Zukowska, 2012). In terms of equivalent concentrations, the baseline levels of norepinephrine (10^{-9} to 10^{-8} M) would

correspond to the concentration of NPY during high stress conditions such as during hemorrhaging shock in the rat (Hirsch & Zukowska, 2012). While the current dogma upholds adrenergic control as the primary determinant of microvascular regulation, our data strongly support considering a shift in this paradigm. Explicitly, although the absolute baseline concentration of norepinephrine is higher than that of NPY, the *potential* contribution of NPY is greater than that of norepinephrine; thus, it is necessary to revisit the classic “adreno-centric” model of SNS-mediated regulation of skeletal muscle microvasculature.

5.8 Importance of collecting data from microvascular networks

Using the rat gluteus maximus muscle, we were successful in evaluating adrenergic, purinergic, and peptidergic receptor activation for arteriolar orders beyond 3A. This is due to the aforementioned clear visibility provided by the preparation itself, coupled with intravital video microscopy and adequate care of the muscle during experimentation (e.g., constant superfusion of physiological salt solution with maintained temperature) in order to uphold tissue integrity. Vasoconstrictor responses due to adrenergic receptor activation have been evaluated in the mouse GM preparation (Moore *et al.*, 2010), although this study did not consider responses beyond 3A arterioles.

Our laboratory has recently investigated the effects of pre-diabetes in response to muscle contraction on branching arterioles in the mouse GM muscle. Data from this study were from branching arteriolar tree segments that included 4A arterioles, where the 4A arterioles were represented as terminal or pre-capillary arterioles which immediately preceded capillary networks (Novielli & Jackson, 2014). In fact, one of the key findings

of this study was that reactivity of these 4A vessels was most affected in pre-diabetic conditions, thereby having the greatest impact on red blood cell distribution to capillaries (Pries *et al.*, 1989). Similarly, in the thesis herein, the vasoconstrictor responses to SNS receptor activation is an integrated response to change in resistance throughout the network. These findings underscore the importance of evaluating complete arteriolar trees, as fundamental data predicting red blood cell distribution can be understood from analyzing hemodynamic data at arteriolar orders beyond 3A.

5.9 Future Studies

5.9.1 Experimental values of hematocrit

By fluorescently labeling red blood cells, we are able to single out a red blood cell as it travels through the vessel segment of interest. Theoretically, use of flow cytometry should allow us to calculate how many red blood cells are represented by a single fluorescently-labeled red blood cell (i.e., what fraction of total red blood cells does a single fluorescent cell represent?). Thereafter, quantifying the number of fluorescent cells across a vessel segment is straightforward, as the fraction of labeled cells is low, allowing for high contrast between labeled and unlabeled portions. Once a finite number of labeled cells are quantified, the data from flow cytometry can be used to determine the total number of red blood cells present in the vessel segment of interest.

While this approach is simple to follow in theory, it is difficult to put into practice. A vessel segment is assumed to be modeled by a cylindrical geometry, where the wall buckling phenomenon (Davis, 2005) is considered negligible in classical blood flow calculations. Using intravital video microscopy, we observe a single plane through a

blood vessel, where the longitudinal height of that plane is limited to the focal depth. While it may seem simple to count the number of fluorescent red cells in a given plane, the fundamental limitation with calculating experimental hematocrit using the described method would be the potential leakage of fluorescent signal from red blood cells outside of the plane of interest. The issue of fluorescent signal leakage would raise concern because it would result in inaccuracies (i.e., an over-estimation) in hematocrit calculations.

Future *in vivo* studies involving use of the “streak length” method should include data that scans through the entire depth of the vessel segment, in addition to focusing on the center plane where the most accurate measure of diameter can be made. By scanning through the depth of the entire vessel lumen, one can approach hematocrit counts by two proposed methods: 1) Acquire finite number of video segments at each incremental step through each of the planes of the vessel segment (plane width can be user-defined), followed by off-line analysis of fluorescent red blood cell incidence in each of the frames for each plane. The total number of labeled cells can be used to determine total number of red blood cells via use of flow cytometry. 2) Acquire a single video spanning the entire depth of the vessel segment, and recreate this video using z-stacking software. Thereafter, the labeled red cells would be quantified and through use of flow cytometry the total red cell fraction through that segment can be calculated.

From these two proposed approaches to calculating experimental hematocrit, the first approach, although more methodical, is predicted to be more experimentally feasible to carry through compared to the second approach. The second approach assumes that the final z-stacked vessel segment would be temporally equivalent throughout the segment;

however, each frame throughout the volume reconstruction of the segment would in fact be temporally out of sync with the subsequent collected frame. This assumption is not necessary nor is it implied in the first approach, whereas the individual video segments from the first approach would resolve any temporal issues as data are averaged throughout the video segment, and does not rely on a single frame to be representative of the flow behavior throughout the segment.

With hematocrit values, it would then be possible to calculate viscosity and develop an experimentally-derived tube hematocrit to discharge hematocrit relationship (originally theoretically derived by Pries *et al.*) that would be specific to skeletal muscle arterioles. As well, the Fahraeus effect, describing how hematocrit changes with diameter, can be derived experimentally and be purposeful for validation of computational flow analysis. As well, with the collection of experimental hematocrit values, it would be beneficial to assess the plasma skimming effect across the vascular network, primarily focusing on blood flow from pre-terminal arterioles to capillaries. *In vivo* hematocrit data would introduce the opportunity to assess numerous other hemodynamic questions, such as (but not limited to): What is the effect of arteriolar diameter on shear rate variability? How does the activation of SNS receptors affect RBC distribution?

5.9.2 Sympathetic nervous system co-transmission of neurotransmitters

Our analysis evaluated vasoconstrictor responses due to activation of one SNS receptor at a time. While these findings highlight essential information regarding the topologically-dependent nature of SNS receptor functionality, the experimental design does not model the physiological case of co-transmitter release. To build upon our findings, future

experiments should entail the evaluation of vasoconstrictor responses to co-delivery of norepinephrine and/or ATP, and/or neuropeptide Y, as well as the combined delivery of all three agonists.

5.9.3 Other topics of interest

Future studies should aim to answer the following: 1) characterizing homology in vascular topology and geometry in rat GM preparations [as previously shown in the mouse GM (Bearden *et al.*, 2004)], 2) acquisition of outlet data at numerous terminal arteriolar segments for input in the computational flow model, 3) the shear rate values in arteriolar diameters under SNS-mediated vasoconstriction and the resolution between shear-mediated dilation and imposing SNS constriction, 4) characterizing purinergic mediation of vasoregulation (constriction and dilation) by delivering combinations of adenosine, ATP, ADP, as well as the appropriate blockade experiments, and 5) conducting SNS neuronal stimulation studies, in the face of antagonist delivery, alongside conducting *in situ* molecular characterization of receptor density at each level of the tree (i.e., immunohistochemistry and/or Western blotting on vessel sections from varying branch orders). Finally, it would be of great interest to estimate the effect(s) of the glycocalyx (a glycoprotein-polysaccharide that is tethered to the luminal surface of the endothelium and extends into the vessel lumen) on the velocity profile shape within the red blood cell free layer, and how the presence of the glycocalyx adjusts wall shear rate calculations. With the resolution used in the thesis herein, the dimensions of the glycocalyx are not resolvable; however, its dimensions can be approximated from literature and incorporated into wall shear rate calculations.

5.10 References

- Abd-Allah NM, Hassan FH, Esmat AY & Hammad SA. (2004). Age dependence of the levels of plasma norepinephrine, aldosterone, renin activity and urinary vanillylmandelic acid in normal and essential hypertensives. *Biol Res* **37**, 95-106.
- Al-Khazraji BK, Novielli NM, Goldman D, Medeiros PJ & Jackson DN. (2012). A simple "streak length method" for quantifying and characterizing red blood cell velocity profiles and blood flow in rat skeletal muscle arterioles. *Microcirculation* **19**, 327-335.
- Baker M & Wayland H. (1974). On-line volume flow rate and velocity profile measurement for blood in microvessels. *Microvasc Res* **7**, 131-143.
- Bearden SE, Payne GW, Chisty A & Segal SS. (2004). Arteriolar network architecture and vasomotor function with ageing in mouse gluteus maximus muscle. *J Physiol* **561**, 535-545.
- Buckwalter JB, Hamann JJ & Clifford PS. (2003). Vasoconstriction in active skeletal muscles: a potential role for P2X purinergic receptors? *J Appl Physiol* (1985) **95**, 953-959.
- Chien S, Usami S, Dellenback RJ, Gregersen MI, Nanninga LB & Guest MM. (1967). Blood viscosity: influence of erythrocyte aggregation. *Science* **157**, 829-831.
- Davis MJ. (2005). An improved, computer-based method to automatically track internal and external diameter of isolated microvessels. *Microcirculation* **12**, 361-372.
- Duling BR, Sarelius IH & Jackson WF. (1982). A comparison of microvascular estimates of capillary blood flow with direct measurements of total striated muscle flow. *Int J Microcirc Clin Exp* **1**, 409-424.
- Ekelund U & Erlinge D. (1997). In vivo receptor characterization of neuropeptide Y-induced effects in consecutive vascular sections of cat skeletal muscle. *Br J Pharmacol* **120**, 387-392.
- Faber JE. (1988). In situ analysis of alpha-adrenoceptors on arteriolar and venular smooth muscle in rat skeletal muscle microcirculation. *Circ Res* **62**, 37-50.
- Gitterman DP & Evans RJ. (2000). Properties of P2X and P2Y receptors are dependent on artery diameter in the rat mesenteric bed. *Br J Pharmacol* **131**, 1561-1568.
- Hester RL & Duling BR. (1988). Red cell velocity during functional hyperemia: implications for rheology and oxygen transport. *Am J Physiol* **255**, H236-244.
- Hirsch D & Zukowska Z. (2012). NPY and stress 30 years later: the peripheral view. *Cell Mol Neurobiol* **32**, 645-659.

- House SD & Lipowsky HH. (1987). Microvascular hematocrit and red cell flux in rat cremaster muscle. *Am J Physiol* **252**, H211-222.
- Jackson DN, Moore AW & Segal SS. (2010). Blunting of rapid onset vasodilatation and blood flow restriction in arterioles of exercising skeletal muscle with ageing in male mice. *J Physiol* **588**, 2269-2282.
- Jackson DN, Noble EG & Shoemaker JK. (2004). Y1- and alpha1-receptor control of basal hindlimb vascular tone. *Am J Physiol Regul Integr Comp Physiol* **287**, R228-233.
- Joshua IG. (1991). Neuropeptide Y-induced constriction in small resistance vessels of skeletal muscle. *Peptides* **12**, 37-41.
- Katritsis D, Kaiktsis L, Chaniotis A, Pantos J, Efstathopoulos EP & Marmarelis V. (2007). Wall shear stress: theoretical considerations and methods of measurement. *Prog Cardiovasc Dis* **49**, 307-329.
- Kesmarky G, Kenyeres P, Rabai M & Toth K. (2008). Plasma viscosity: a forgotten variable. *Clin Hemorheol Microcirc* **39**, 243-246.
- Marshall JM. (1982). The influence of the sympathetic nervous system on individual vessels of the microcirculation of skeletal muscle of the rat. *J Physiol* **332**, 169-186.
- Mayrovitz HN & Roy J. (1983). Microvascular blood flow: evidence indicating a cubic dependence on arteriolar diameter. *Am J Physiol* **245**, H1031-1038.
- Moore AW, Jackson WF & Segal SS. (2010). Regional heterogeneity of alpha-adrenoreceptor subtypes in arteriolar networks of mouse skeletal muscle. *J Physiol* **588**, 4261-4274.
- Murrant CL, Dodd JD, Foster AJ, Inch KA, Muckle FR, Ruiz DA, Simpson JA & Scholl JH. (2014). Prostaglandins induce vasodilatation of the microvasculature during muscle contraction and induce vasodilatation independent of adenosine. *J Physiol* **592**, 1267-1281.
- Murray CD. (1926). The Physiological Principle of Minimum Work: I. The Vascular System and the Cost of Blood Volume. *Proc Natl Acad Sci U S A* **12**, 207-214.
- Namgung B, Ong PK, Johnson PC & Kim S. (2011). Effect of cell-free layer variation on arteriolar wall shear stress. *Ann Biomed Eng* **39**, 359-366.

- Novielli NM & Jackson DN. (2014). Contraction-evoked vasodilation and functional hyperaemia are compromised in branching skeletal muscle arterioles of young pre-diabetic mice. *Acta Physiol (Oxf)* **211**, 371-384.
- Nyberg M, Al-Khazraji BK, Mortensen SP, Jackson DN, Ellis CG & Hellsten Y. (2013). Effect of extraluminal ATP application on vascular tone and blood flow in skeletal muscle: implications for exercise hyperemia. *Am J Physiol Regul Integr Comp Physiol* **305**, R281-290.
- Ohyanagi M, Faber JE & Nishigaki K. (1991). Differential activation of alpha 1- and alpha 2-adrenoceptors on microvascular smooth muscle during sympathetic nerve stimulation. *Circ Res* **68**, 232-244.
- Pittman RN & Ellsworth ML. (1986). Estimation of red cell flow microvessels: consequences of the Baker-Wayland spatial averaging model. *Microvasc Res* **32**, 371-388.
- Pries AR, Ley K, Claassen M & Gaetgens P. (1989). Red cell distribution at microvascular bifurcations. *Microvasc Res* **38**, 81-101.
- Reneman RS, Arts T & Hoeks AP. (2006). Wall shear stress--an important determinant of endothelial cell function and structure--in the arterial system in vivo. Discrepancies with theory. *J Vasc Res* **43**, 251-269.
- Reneman RS & Hoeks AP. (2008). Wall shear stress as measured in vivo: consequences for the design of the arterial system. *Med Biol Eng Comput* **46**, 499-507.
- Segal SS & Duling BR. (1987). Propagation of vasodilation in resistance vessels of the hamster: development and review of a working hypothesis. *Circ Res* **61**, II20-25.
- Sriram K, Intaglietta M & Tartakovsky DM. (2014). Non-Newtonian flow of blood in arterioles: consequences for wall shear stress measurements. *Microcirculation* **21**, 628-639.
- Tangelder GJ, Slaaf DW, Muijtjens AM, Arts T, oude Egbrink MG & Reneman RS. (1986). Velocity profiles of blood platelets and red blood cells flowing in arterioles of the rabbit mesentery. *Circ Res* **59**, 505-514.
- VanTeeffelen JW & Segal SS. (2006). Rapid dilation of arterioles with single contraction of hamster skeletal muscle. *Am J Physiol Heart Circ Physiol* **290**, H119-127.

Appendices

Appendix A: Copyright license agreement for Chapter 2

**JOHN WILEY AND SONS LICENSE
TERMS AND CONDITIONS**

Jan 24, 2015

This Agreement between Baraa K Al-Khazraji ("You") and John Wiley and Sons ("John Wiley and Sons") consists of your license details and the terms and conditions provided by John Wiley and Sons and Copyright Clearance Center.

License Number	3555630062308
License date	Jan 24, 2015
Licensed Content Publisher	John Wiley and Sons
Licensed Content Publication	Microcirculation
Licensed Content Title	A Simple "Streak Length Method" for Quantifying and Characterizing Red Blood Cell Velocity Profiles and Blood Flow in Rat Skeletal Muscle Arterioles
Licensed Content Author	BARAA K. AL-KHAZRAJI, NICOLE M. NOVIELLI, DANIEL GOLDMAN, PHILIP J. MEDEIROS, DWAYNE N. JACKSON
Licensed Content Date	Apr 24, 2012
Pages	9
Type of use	Dissertation/Thesis
Requestor type	Author of this Wiley article
Format	Electronic
Portion	Full article
Will you be translating?	No
Title of your thesis / dissertation	A novel microvascular blood flow technique for characterizing sympathetic nervous system control in skeletal muscle microcirculation
Expected completion date	Apr 2015

Appendix B: Animal use protocol approval

eSirius Notification - Annual Protocol Renewal APPROVED by the AUS 2012-018::1



2012-018::1:

AUP Number: 2012-018

AUP Title: Microvascular function in skeletal muscle

Yearly Renewal Date: 09/01/2013

The YEARLY RENEWAL to Animal Use Protocol (AUP) 2012-018 has been approved, and will be approved for one year following the above review date.

1. This AUP number must be indicated when ordering animals for this project.
2. Animals for other projects may not be ordered under this AUP number.
3. Purchases of animals other than through this system must be cleared through the ACVS office.
Health certificates will be required.

REQUIREMENTS/COMMENTS

Please ensure that individual(s) performing procedures on live animals, as described in this protocol, are familiar with the contents of this document.

The holder of this Animal Use Protocol is responsible to ensure that all associated safety components (biosafety, radiation safety, general laboratory safety) comply with institutional safety standards and have received all necessary approvals. Please consult directly with your institutional safety officers.

Submitted by: Kinchlea, Will D
on behalf of the Animal Use Subcommittee

Appendix C: An automated cell-counting algorithm for fluorescently-stained cells in migration assays

A form of this manuscript has been published:

Al-Khazraji BK, Medeiros PJ, Novielli NM & Jackson DN. (2011). An automated cell-counting algorithm for fluorescently-stained cells in migration assays. *Biol Proced Online* **13**, 9.

Background

Traditionally, *in vitro* cell-counting methodologies consist of manual counts through use of a hemacytometer (Kukulski *et al.*, 2007; Ricardo & Phelan, 2008). Generally, cell migration experiments are conducted using modified Boyden chambers, whereby the cells of interest migrate through a porous membrane and are stained for counting. Such migratory cells are commonly labelled on the membrane with a crystal violet stain (Chien *et al.*, 2011; Jones *et al.*, 2012), Trypan Blue dye (Kuo *et al.*, 2010), or hematoxylin (Jee *et al.*, 2007; Zhu *et al.*, 2007; Wedel *et al.*, 2011), and quantified manually. Although it remains the gold standard, manual cell counting is very time-consuming and may introduce experimenter bias, thus increasing the potential for measurement errors (Piuri & Scotti, 2004).

In an effort to increase efficiency and mitigate potential sources of bias/error associated with manual cell counting, a number of commercially available software suites provide automated cell counting from microscopic images. These software packages enable users to collect cell counts from random fields of view within specimens of interest.

Unfortunately, these software suites contain proprietary algorithms (making them inadaptable), are generally expensive, and often require powerful computers, making them an unfeasible option for many research laboratories.

Whole membrane quantification has been accomplished through spectrophotometric methods using absorbance microplate readers (Denholm & Stankus, 1995; Mu *et al.*, 2006; He *et al.*, 2010). These microplate readers are able to detect total stained (if using dyes/stains) or fluorescence signal, where output values are a direct indication of total

migrated cells. Although absorbance microplate readers allow for an expeditious analysis of migration assays, they are costly and do not provide a record of membrane images should manual confirmation or further analysis be required.

In the current study, we sought to develop a feasible, valid, and reliable algorithm designed to automate cell counting using stored images from cell migration experiments. In an effort to validate our algorithm we: 1) compared automated cell counts with manual counts from a blinded experimenter; and 2) determined the effect of objective power (2.5×, 5×, and 10×) and increasing the number of cells in images on our algorithm's ability to accurately resolve and quantify cells.

Results

Cell-Counting Algorithm

Matlab® software was used to create an algorithm (Appendix A) for counting 4',6-diamidino-2-phenylindole (DAPI)-stained 4T1 (murine breast cancer) cells from cell migration assays. DAPI nucleic stain provided images with high contrast between nuclei and background (Figure 1, Panel A). Our algorithm consisted of three main components (in order) for automated counting:

- 1) Image thresholding: Original images (Figure 1A) were read into the algorithm, and through use of the Matlab® command *graythresh*, Otsu's method for global thresholding (Otsu, 1979) was applied for selection of a threshold level used to convert the original image into a binary image. Briefly, Otsu's method segments an image by maximizing the separability of the two populations in a histogram. Three

- conditions must be met in order to maximize use of Otsu's method: a) minimum variability in grey levels of foreground objects, b) minimum variability in background grey levels, c) maximum variability between background and foreground objects grey levels. These conditions are met by the DAPI-nucleic stained images used in this study.
- 2) Pixel intensity values greater than threshold level were assigned a value of 1 (white; Figure 1, Panel B), and values lower than threshold level were assigned a value of 0 (black).
 - 3) Calculating average cell nucleus area: The command *regionprops* (measures properties for image regions) was then used to sequentially (from left to right of image) label each object at its centroid (Figure 1, Panel C), and to measure area (pixel²) of each object in the binary image. The trimmed mean (command *trimmean*) of the constructed area array was calculated with a chosen percent value of 10%. As such, for a given image, 5% of the highest and lowest values from the area cell array were not included in calculation of the mean cell nucleus area. Average cell area (mean \pm S.E.M.) at 2.5 \times , 5 \times , and 10 \times power was 20.9 ± 0.6 pixels², 62.4 ± 1.1 pixels², and 256.1 ± 18.9 pixels², respectively, and was independent of total number of seeded cells.
 - 4) Determining final cell count: Each value in the area cell array was divided by the average cell nucleus area and rounded to the nearest integer (using command *round*). The sum of the integers then provided the total number of cells for a given image. Final counts were saved as a text file and exported into Microsoft® Excel® software (Version 12.2.8) for column statistics and data organization.

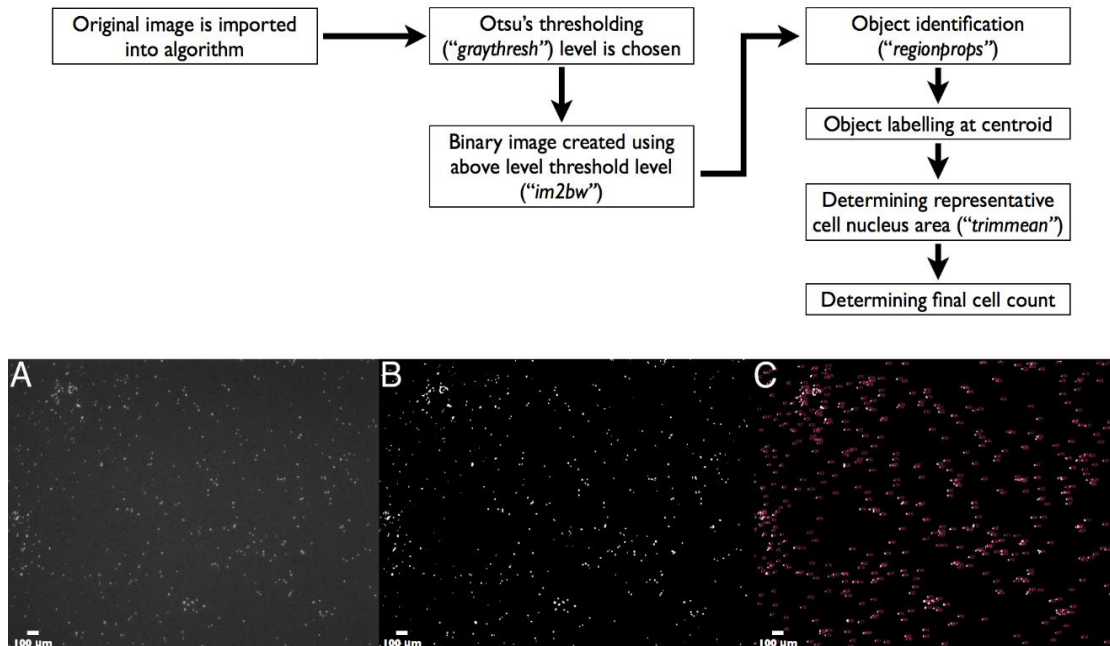


Figure 1: Flow Chart of Algorithm Processes.

Panel A: original image (2.5×) read by algorithm; B: post-thresholding using Otsu's method for selection of threshold level. C: thresholded image with each object numerically labeled.

Algorithm Outputs Compared to Manual Counts

A blinded experimenter conducted manual cell counts using ImageJ software (ImageJ 1.43u, National Institute of Health, Bethesda, Maryland, USA), which required them to manually place a marker on each cell. A total of 47 images from varying fields of view within each membrane (for 10,000 and 100,000 total seeded cells) were read in as a series of images (.tif series) based on sequential file name order. Using our algorithm, total computing time for 47 images was 14.5 seconds, which was 596 times faster than manual counting [total manual counting time for 47 images = 8640 seconds (2.4 hours)]. Linear correlation between manual and automated cell counts from 47 images images taken using 2.5×, 5×, and 10× objectives illustrated near perfect correlation and congruency ($r^2 = 0.99$, $P < 0.0001$, Slope = 1.02, Y intercept = 2.2; Figure 2).

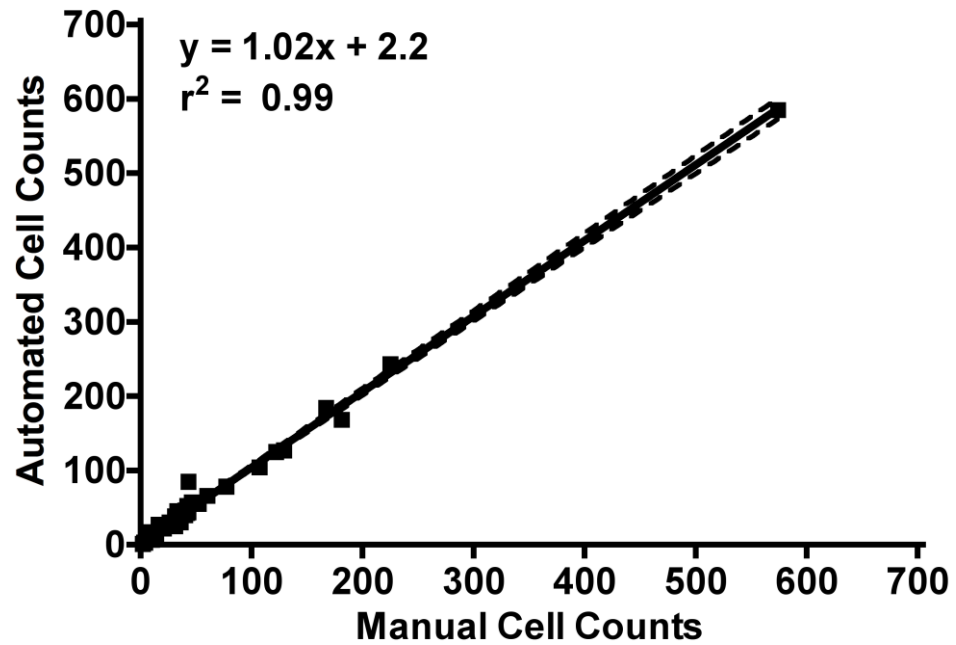


Figure 2: Manual versus Automated Cell Counts. Linear regression of manual versus automated cell counts for 47 images, with a correlation of $r^2 = 0.99$, $P < 0.0001$. Dotted lines represent 95% confidence interval for slope and y-intercept.

Algorithm Outputs Compared to Manual Cell Counts Based on Objective Power and Total Seeded Cells

To determine the effect of objective power on the software's ability to resolve migrated cells, a single 2.5× image (centered on the membrane) was captured for experiments that used 10,000 and 100,000 seeded cells, followed by images of the same membrane area at 5×, and then 10×. Multiple 5× and 10× images were assembled into a photomontage (all image resolutions were collected and maintained at 150 dpi) to reconstruct exact membrane area covered by the single 2.5× image. At each number of total seeded cells (10,000 and 100,000 cells), manual counts (in triplicate) were performed on the single 2.5× image, 5× photomontage, and the 10× photomontage (Figure 3). It is important to note that during cell migration experiments not all seeded cells migrate through the membrane, thus cell counts are lower than the total number of seeded cells.

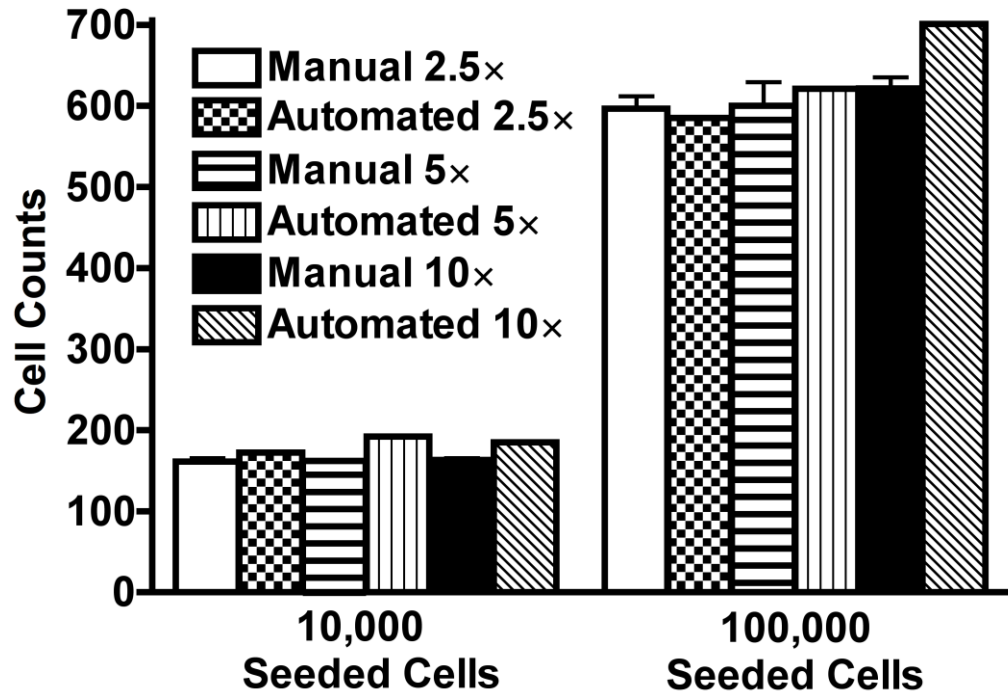


Figure 3: Manual versus Automated Cell Counts Based on Objective Power.

Comparison of manual versus automated cell counts for varying objective power (2.5 ×, 5 × montages, and 10 × montages) and total seeded cells (10,000 and 100,000 cells).

Within each group of total seeded cells, RM ANOVA confirmed no significant difference between manual and automated counts at all objective powers.

Discussion

In the current study, an automated cell counting algorithm was created to quantify resultant migratory 4T1 breast cancer cells in cell migration assays that used 10,000 and 100,000 total seeded cells. The algorithm was only tested in migration assays conducted in modified Boyden chambers using DAPI-stained 4T1 breast cancer cells. For a total of 47 images, automated cell counts had strong correlation with manual counts ($r^2 = 0.99$, $P < 0.0001$; Figure 2). To highlight the congruency between methods, the y-intercept for the linear regression line (Fig. 2) indicated that our automated method overestimated an average of only 2 cells under all experimental and imaging conditions. Furthermore, there were no differences in cell counts between methods regardless of experimental conditions (number of cells seeded) or objective power (Fig. 3).

Our results support the notion that manual cell counting is time consuming (47 images; manual counting time = 2.4 hours versus automated computing time = 14.5 seconds) and subject to operator bias (hence our experimenter was blinded). Further, it is difficult to reproduce exact measurements using manual methods (hence variability in our manual cell counts, Fig. 3), which is likely due to disparate criteria under which manual cell counting is performed from image to image. Our automated method processes and counts all images using set criteria making it immune to the aforementioned sources of error. Upon multiple independent screening of the same 47 images, zero variability was still obtained.

Quantification of migrated cells from cell migration experiments are generally limited to objective powers ranging from $5\times$ to $200\times$ (Alge-Priglinger *et al.*, 2009) and thus require

3 (Du *et al.*, 2010) to 10 (Kusuma *et al.*, 2012) fields of view in an effort to capture a representative sample of the membrane. The consistency in computed cell counts among different objective magnifications highlights our algorithm's ability to accurately resolve and count cells even under low magnification; thus enabling the user to analyze larger proportions of total membrane surface area in one field of view. This is due to the thresholding portion of our algorithm, which optimizes contrast between cell nuclei and the image background (Fig. 1).

Conclusions

We have successfully developed a feasible algorithm for automated cell counting within cell migration assays. Automated cell counts agreed favorably with manual counts for all objective powers and for different levels of total seeded cells. As well, in contrast to manual counting, our automated algorithm counted cells quickly and independent of bias, and presented zero variability for counting cells multiple times within single images.

Materials and methods

Cell Culture

4T1 cells, a gift from Dr. Fred Miller (Wayne State University, Michigan USA), were cultivated in high glucose Dulbecco's Minimal Essential Medium (DMEM) supplemented with 10% sterile FBS. Cells were incubated at 37°C and 5% carbon dioxide. At approximately 80% confluency, cells were washed with HBSS and passaged using 0.25% trypsin-EDTA treatment for dissociation.

Migration Assays

Migration assays were conducted using a modified Boyden chamber apparatus with a 12-well plate and cell culture inserts with polyethylene terephthalate membranes (8 μm pores, BD Biosciences). 4T1 cells were plated in the upper chamber in serum-free media (10,000 and 100,000 cells). Serum-containing media (10% fetal bovine serum) was added to the bottom chamber as a chemoattractant. After 24 hours of incubation, non-migrated cells were scraped from the top of the membrane with a cotton swab; migrated cells (on the bottom of the membrane) were then fixed in methanol and stained with DAPI. The mounted on slides, and imaged using fluorescence microscopy at 2.5 \times , 5 \times and 10 \times magnification (Zeiss Axiovert 200, Zeiss AxioCam HRc camera). Image exposure time was consistent at each magnification (2.5 \times : 581 ms; 5 \times : 206 ms, 10 \times : 49 ms).

Image Assembly

To reproduce single 2.5 \times fields of view at higher objective powers, photomontages (.tif) of overlapping fields of view taken at the 5 \times and 10 \times power objectives were assembled in Adobe® Photoshop® CS3 [(version 10.0.1), no changes were made to the original image files].

Statistical Analysis and Data Presentation

All data are presented as mean \pm S.D., unless stated otherwise. Statistical analysis was performed using Prism Software (version 4, GraphPad Software Inc, La Jolla, CA, USA) and differences were accepted as statistically significant when $P < 0.05$. Manual versus automated cell counts for all 47 images (Fig. 2) were plotted using linear regression

analysis. To analyze the effects of objective power and manual versus automated counts within a given level of seeded cells, a repeated measures analysis of variance (RM ANOVA) was conducted (Fig. 3).

References

- Alge-Priglinger CS, Andre S, Kreutzer TC, Deeg CA, Kampik A, Kernt M, Schoffl H, Priglinger SG & Gabius HJ. (2009). Inhibition of human retinal pigment epithelial cell attachment, spreading, and migration by the human lectin galectin-1. *Mol Vis* **15**, 2162-2173.
- Chien W, O'Kelly J, Lu D, Leiter A, Sohn J, Yin D, Karlan B, Vadgama J, Lyons KM & Koeffler HP. (2011). Expression of connective tissue growth factor (CTGF/CCN2) in breast cancer cells is associated with increased migration and angiogenesis. *Int J Oncol* **38**, 1741-1747.
- Denholm EM & Stankus GP. (1995). Differential effects of two fluorescent probes on macrophage migration as assessed by manual and automated methods. *Cytometry* **19**, 366-369.
- Du WW, Yang BB, Shatseva TA, Yang BL, Deng Z, Shan SW, Lee DY, Seth A & Yee AJ. (2010). Versican G3 promotes mouse mammary tumor cell growth, migration, and metastasis by influencing EGF receptor signaling. *PLoS One* **5**, e13828.
- He S, Kumar SR, Zhou P, Krasnoperov V, Ryan SJ, Gill PS & Hinton DR. (2010). Soluble EphB4 inhibition of PDGF-induced RPE migration in vitro. *Invest Ophthalmol Vis Sci* **51**, 543-552.
- Jee BK, Lee JY, Lim Y, Lee KH & Jo YH. (2007). Effect of KAI1/CD82 on the beta1 integrin maturation in highly migratory carcinoma cells. *Biochem Biophys Res Commun* **359**, 703-708.
- Jones ML, Ewing CM, Isaacs WB & Getzenberg RH. (2012). Prostate cancer-derived angiogenin stimulates the invasion of prostate fibroblasts. *J Cell Mol Med* **16**, 193-201.
- Kukulski F, Ben Yebdri F, Lefebvre J, Warny M, Tessier PA & Sevigny J. (2007). Extracellular nucleotides mediate LPS-induced neutrophil migration in vitro and in vivo. *J Leukoc Biol* **81**, 1269-1275.
- Kuo WW, Weng JR, Huang CY, Tsai CH, Liu WH, Wen CH, Tsai SC & Wu CH. (2010). Exploring the molecular mechanisms of OSU-03012 on vascular smooth muscle cell proliferation. *Mol Cell Biochem* **344**, 81-89.

- Kusuma N, Denoyer D, Eble JA, Redvers RP, Parker BS, Pelzer R, Anderson RL & Pouliot N. (2012). Integrin-dependent response to laminin-511 regulates breast tumor cell invasion and metastasis. *Int J Cancer* **130**, 555-566.
- Mu H, Ohashi R, Yan S, Chai H, Yang H, Lin P, Yao Q & Chen C. (2006). Adipokine resistin promotes in vitro angiogenesis of human endothelial cells. *Cardiovasc Res* **70**, 146-157.
- Otsu N. (1979). A threshold selection method from gray-level histograms. *IEEE Transactions on Systems, Man and Cybernetics* **9**, 62-66.
- Piuri V & Scotti F. (2004). Morphological classification of blood leucocytes by microscope images. *CIMSA 2004 - IEEE International Conference on Computational Intelligence for Memremment Systems and Application*.
- Ricardo R & Phelan K. (2008). Counting and determining the viability of cultured cells. *J Vis Exp*.
- Wedel S, Hudak L, Seibel JM, Makarevic J, Juengel E, Tsaour I, Wiesner C, Haferkamp A & Blaheta RA. (2011). Impact of combined HDAC and mTOR inhibition on adhesion, migration and invasion of prostate cancer cells. *Clin Exp Metastasis* **28**, 479-491.
- Zhu BH, Zhan WH, Li ZR, Wang Z, He YL, Peng JS, Cai SR, Ma JP & Zhang CH. (2007). (-)-Epigallocatechin-3-gallate inhibits growth of gastric cancer by reducing VEGF production and angiogenesis. *World J Gastroenterol* **13**, 1162-1169.

Appendix D: Cell counting algorithm

```

%%Automated Cell Counting Algorithm.
    %%Created by Baraa Al-Khazraji,
    %%The Jackson Laboratory, Department of Medical Biophysics,
    Schulich School of Medicine & Dentistry, The University of Western
    Ontario. PROPERTY OF Dr. DWAYNE N. JACKSON, FREE FOR ACADEMIC USE ONLY

close all
clear all
clc
% p = ('/Users/dwaynejackson/Jackson Lab Exp Files renamed for
matlab/SNAP-0001.tif');
% filelist = dir([fileparts(p) filesep 'SNAP-00*.tif']);
% fileNames = {filelist.name}';
%
% % file = '/Users/dwaynejackson/Desktop/Jackson Lab Exp Files renamed
for
% % matlab/SNAP-00*.tif';
% I = imread(fileNames{1});
% [mrows,ncols] = size(I);
% totalimages = length(fileNames);
FoldertoRead = '/Users/dwaynejackson/Desktop/now reading';
Pattern_of_files = fullfile(FoldertoRead, '*.tif');
tif_Files = dir(Pattern_of_files);

for i = 1:length(tif_Files)
    baseFileName = tif_Files(i).name;
    fullFileName = fullfile(FoldertoRead, baseFileName);
    fprintf(1, 'Now Reading %s\n', fullFileName);

    %%Open individual .tif file for analysis
    I = imread(fullFileName);

    %%Show current .tif file that is being analyzed
    figure
    imshow(I)
    %%Turn image into a binary image, with a variable threshold value
    B = im2bw(I,0.32);
    figure
    imshow(B)
    %%Label each object in the binary image
    bw = bwlabel(B);
    %%Quantify each labeled object; choosing 'all' means that all
parameters
    %% (majoraxislength, perimeter, centroid, etc.) are analyzed
    measures = regionprops(B, 'all');
    numberOfitems = size(measures, 1);
    %%Label each object in the binary image at its centroid, in the order
that it is analyzed, and make the font pink, and size 12
    for k = 1 : numberOfitems % Loop through all items.
        itemCentroid = measures(k).Centroid; % Get centroid.
        % Write item number over item at its centroid.
        text(itemCentroid(1), itemCentroid(2), num2str(k), 'Color',
[1 0.3 0.5], 'fontsize',12);
    end
end

```

```

%%Convert each measurement from regionprops output into cells
convertstruct2cell = struct2cell(measures);

%%Take fluorescent area of each object and convert it to a matrix,
then
%%take the sum of total fluorescent area for each image
Area = convertstruct2cell(1,:);
Area_array = cell2mat(Area);
TotalArea = sum(Area_array(1,:));

%%Take the mean of fluorescent area in each image
normalmean = mean(Area_array);

%%Take the mean of fluorescent area in each image, then cleave off
outliers within 10% of the mean
trimmedmean = trimmean(Area_array,10);

%%Take the Area matrix and divide each value by by the mean
fluorescent
%%area, then round to the nearest integer. Done using normal mean,
and
%%the "trimmedmean" (outliers removed)
WholeCells = round(Area_array/normalmean);
WholeCellstrimmed = round(Area_array/trimmedmean);

%%Add up all the integers to calculate total cells in each image
TotalWholeCells(i) = sum(WholeCells);
TotalWholecellstrimmed(i) = sum(WholeCellstrimmed);

% NumberofCells_highrange = TotalArea/17;
% NumberofCells_lowrange = TotalArea/20;
% Averagenumber_fromhighandlowrange(i) = (NumberofCells_highrange +
NumberofCells_lowrange)/2;

%%Convert the row to a column (transpose it)
Totalwholecells_usingtrimmedmean = TotalWholecellstrimmed';
Totalwholecells_usingnormalmean = TotalWholeCells';

% ConvertFileName = char(baseFileName);
% FileName = ConvertFileName';
trimmean_mean = trimmedmean';
normal_mean = normalmean';
% Averagenumber_from_highandlowrange =
Averagenumber_fromhighandlowrange';

%%Create a dataset of results
T1_25000cells_5x = dataset(Totalwholecells_usingtrimmedmean,
Totalwholecells_usingnormalmean,normal_mean,trimmean_mean);

%%Export dataset to a text file, and name the text file
export(T1_25000cells_5x)
end

```

Curriculum Vitae

BARAA K. AL-KHAZRAJI

EDUCATION

Direct-Entry Ph.D. (Discipline: Medical Biophysics) – Under supervision of Dr. Dwayne N. Jackson; The University of Western Ontario. London, Ontario, Canada
September 2009 – April 2015 (maternity leave June 2014 – January 2015)

B.Sc. Honors Specialization in Medical Biophysics (Phys. Sci. Concentration) Minor in Philosophy – The University of Western Ontario. London, Ontario, Canada
September 2005 – April 2009

AWARDS

- Alan C. Groom Award - awarded annually for the most effective graduate student seminar, UWO, September 2014
- Alfred Jay Award for Cellular Cardiovascular Research - annually awarded for best paper in basic biophysical research, UWO, April 2014
- 1st Place Award Winner for London Health Research Day Platform Competition, March 2013
- Nominated for Graduate Student Teaching Award, 2013
- Silver Award Winner at the Canadian Institute of Health Research (CIHR) Doctoral Student Poster Presentations within the Canadian Student Research Health Forum, Winnipeg, MB, Canada, June 2011
- Nominated for the Drs. Madge and Charles Macklin Teaching & Research Fellowship award, 2011
- Microcirculatory Society's Zweifach Graduate Research Student Award Winner, 2011
- UWO Graduate Thesis Awards Fund Winner, 2010-2011
- UWO University Student Council Teaching Honor Roll, 2009-2010
- UWO Western Mustang Band Most Dedicated Band Member Award Winner, 2007-2008

SCHOLARSHIPS

- Western University Faculty of Health Sciences Postdoctoral Fellowship (2015-2016)
- CIHR Banting Postdoctoral Fellowship Nominee, September 2014
- Alexander Graham Bell Canada Graduate Scholarship (NSERC CGS D; September 2012 – August 2014)
- Nominated by UWO for Vanier Canada Graduate Scholarship (September 2011), rank: top 35% in Canada
- Ontario Graduate Scholarship (September 2012 – August 2013) - **Declined**

- Ontario Graduate Scholarship (September 2011 – August 2012)
- Alexander Graham Bell Canada Graduate Scholarship (NSERC CGS M; September 2010 – August 2011)
- CIHR Strategic Training Program in Vascular Research (September 2009 – August 2011)
- Ontario Graduate Scholarship (September 2009 – August 2010)
- SSMD Graduate Tuition Scholarship (full tuition scholarship; September 2009 – August 2014)
- Western Entrance Scholarship (September 2005 – April 2009)

RELEVANT WORK EXPERIENCE

Teaching

- Guest Lecturer for 3rd year Medical Biophysics course (MBP 3501F) 2011-2014
- Guest Lecturer for 4th year Medical Biophysics course (MBP 4535) 2012-2014
- Teaching Assistant/ Lab Instructor, Assisted in course development (General Biophysics Laboratory (course code 3970Z)). UWO USC Teaching Honor Roll (2009 – 2010) 2009 -2011
- Teaching Assistant for 3rd year Medical Biophysics course (MBP 3501F) 2012-2013

Mentoring

- Research Mentor for Mohammad Al-Tarhuni (1st year MSc student, May 2014 – current)
- Research Mentor for Partners in Education High School Student: Nicole Omoruwa (February 2010 – Current)
- Research Mentor for Elton Law (4th year Physiology student, Thesis project, September 2013-April 2014)
- Research Mentor for David Yeung (3rd year MBP student, 6 week project, September 2013-April 2014)
- Research Mentor for Jenna Kara (3rd year MBP student, 6 week project, September 2013-April 2014)
- Assistant Research Mentor for UWO Scholar's Elective Student: Ryann Kwan (May – June 2012)
- Research Mentor for 4th year Medical Biophysics Thesis student: Samantha Coleman (September 2011 – April 2012)
- Research Mentor (3rd Year General Biophysics Laboratory (course code 3970Z) Research Project): Joanne Wong, Department of Medical Biophysics (January – April 2011)
- Research Mentor (undergraduate summer student researcher): Kelley Bronson, Department of Medical Biophysics (May – August 2009)

PUBLICATIONS

Published Peer Reviewed Articles

Shoemaker J.K., Badrov M., **Al-Khazraji B.K.**, Jackson D.N. *Neural control of vascular function* (invited review). *Comprehensive Physiology*. 2015. (in 2nd review; submission #: CPHY-15-0004; May 2015)

Al-Khazraji B.K., Saleem A., Goldman D., Jackson D.N. *From one generation to the next: A comprehensive account of sympathetic receptor control in branching arteriolar trees*. *Journal of Physiology*. 2015 (in press; April 2015).

Yeung T.P., Kurdi M., Wang Y., **Al-Khazraji B.**, Morrison L., Hoffman L., Jackson D., Crukley C., Lee T.Y., Bauman G, Yartsev S. *CT perfusion imaging as an early biomarker of differential response to stereotactic radiosurgery in C6 rat gliomas*. *PLoS One*. 2014.

Nyberg M., **Al-Khazraji B.K.**, Mortensen S.P., Jackson D.N., Ellis C.G., Hellsten Y. *Effect of extraluminal ATP application on vascular tone and blood flow in skeletal muscle: implications for exercise hyperemia*. *The American Journal of Physiology - Regulatory, Integrative and Comparative Physiology*. 2013.

Novielli N.M., **Al-Khazraji B.K.**, Medeiros P.J., Jackson D.N. *Pre-diabetes augments neuropeptide Y1- and $\alpha 1$ -receptor control of basal hindlimb vascular tone in young ZDF rats*. *PLoS ONE*. 2012.

Al-Khazraji B.K., Novielli N.M., Goldman D., Medeiros P.J., Jackson D.N. *A simple "streak method" for quantifying and characterizing red blood cell velocity profiles and blood flow in rat skeletal muscle arteriolar networks*. *Microcirculation*. 2011.

Al-Khazraji B.K., Medeiros P.J., Novielli N.M., Jackson D.N. *Method: An automated cell-counting algorithm for fluorescent-stained cells in migration assays*. *Biological Procedures Online*. 2011.

Medeiros P.J., **Al-Khazraji B.K.**, Novielli N.M., Postovit L.M., Chambers A.F., Jackson D.N. *Neuropeptide Y stimulates proliferation and migration in the 4T1 breast cancer cell line*. *International Journal of Cancer*. 2011.

Peer Reviewed Abstracts

Al Tarhuni M., **Al-Khazraji B.K.**, Omoruwa N, Jackson D.N. *Level of Sympathetically Mediated Arteriolar Control is Inversely Dependent on Arteriolar Segment Length in Rat Gluteus Maximus Microvascular Networks*. *Experimental Biology*. The FASEB Journal March 2015

Al-Khazraji B.K., Saleem A., Goldman D., Jackson D.N. *Hemodynamic consequences of spatially-dependent sympathetic regulation in skeletal muscle arteriolar trees*. (678.14) *The FASEB Journal* April 2014 28:678.14

Yeung T.P.C., **Al-Khazraji B.**, Morrison L., Hoffman L., Jackson D., Lee T.Y., Bauman G., and Yartsev S.. Monitoring vascular response to stereotactic radiosurgery in a brain tumor model using CT perfusion. *Radiotherapy and Oncology*. 2013;108(supplement 1):S25.

Yeung T.P.C., **Al-Khazraji B.**, Morrison L., Hoffman L., Jackson D., Lee T.Y., Yartsev S., and Bauman G. Assessing the acute anti-angiogenic effect of Bevacizumab on glioma with CT perfusion. The 11th Imaging Network Ontario Symposium. (04/02/13 – 05/02/13).Book of abstract: page 55

Yeung T.P.C., **Al-Khazraji B.**, Morrison L., Hoffman L., Jackson D., Lee T.Y., Bauman G., Yartsev S. Monitoring the vascular response of brain tumor to stereotactic radiosurgery with CT perfusion. The 11th Imaging Network Ontario Symposium. (04/02/13 – 05/02/13). Book of abstract: page 56.

Al-Khazraji B.K., and Jackson D.N. (2012) *Heterogeneous Arteriolar Constriction And Blood Flow Responses To Sympathetic Co-Transmitters In Skeletal Muscle Microvascular Networks*. Presented at the Joint Meeting of the British and American Microcirculation Societies. Oxford University, Oxford, United Kingdom.

Novielli, N.M., **Al-Khazraji B.K.**, Jackson D.N. (2012). *Pre-diabetes and microvascular dysfunction in contracting skeletal muscle*. The Canadian Student Health Research Forum 2012 Book. Winnipeg, Manitoba, Canada.

Al-Khazraji B.K., Novielli, N.M., Goldman D., Ellis C.G., Jackson D.N. (2011). *Novel Video Method for Acquiring and Modeling In Vivo Hemodynamic Data From Arteriolar Networks of Rat Gluteus Maximus Skeletal Muscle*. 2011 CIHR National Student Research Poster Competition (National). Abstract #255. The Canadian Student Health Research Forum 2011 Book. Winnipeg, Manitoba, Canada. (Recipient of Silver Award)

Al-Khazraji B.K., Novielli N.M., Goldman D., Ellis C.G., Jackson D.N. (2011). *Novel Video Method for Acquiring and Modeling In Vivo Hemodynamic Data From Arteriolar Networks of Rat Gluteus Maximus Skeletal Muscle*. *Experimental Biology 2011 (International)*; Abstract # 7005 (Poster). The FASEB Journal April 2011. Washington, District of Columbia, United States

Novielli, N.M., **Al-Khazraji B.K.**, Jackson D.N. (2011). *Impaired microvascular control in contracting skeletal muscle in a murine model of prediabetes*. *Experimental Biology 2011 (International)*. The FASEB Journal April 2011. Washington, District of Columbia, United States

Novielli, N.M., **Al-Khazraji B.K.**, Ellis C.G., Jackson D.N. (2010). *Sympathetic modulation of baseline hindlimb blood flow and vascular conductance in a model of prediabetes using young Zucker Diabetic Fatty rats*. *Experimental Biology 2010*. The FASEB Journal April 2010.

Lizardo M.M., **Al-Khazraji B.**, Percy D.B., Wirtzfeld L.A., MacDonald I., Fenster A., Lacefield J.C., and Chambers A.F. (2008) *Optical Fluorescence and High Frequency (40mHz) Ultrasound Imaging of Spontaneous Lymph Node Metastases in a Xenograft Model of Breast Cancer*. (Poster) Canadian Breast Cancer Research Alliance (CBCRA) Reasons for Hope Conference.

Lizardo M.M., Strike D.R.G., **Al-Khazraji B.**, Wirtzfeld L.A., MacDonald I., Fenster A., Lacefield J., and Chambers A.F. (2007) *Development of a High Frequency Ultrasound (40mHz) Imaging Technique to Study the Progression of Lymph Node Metastasis in a Mouse Model of Breast Cancer*. (Poster) National Cancer Institute of Canada (NCIC) 60th Anniversary Canadian Cancer Research Conference.

INVITED PRESENTATIONS

Annual Alan C. Burton Day, Graduate Student speaker, Department of Medical Biophysics, April 2015

Canadian Student Research Health Forum (held by CIHR) Doctoral Student National Poster Competition Winnipeg, MB, Canada. June 2011 (**2nd place winner**)

London Health Research Day Platform Competition. London Convention Centre, March 2012 and 2013 (**2013 1st Place Award Winner**), London, Ontario, Canada.